

IMAGE PROCESSING CONSIDERATIONS FOR HIGH RESOLUTION
DIFFUSION TENSOR IMAGING OF THE HUMAN BRAINSTEM

APPROVED BY SUPERVISORY COMMITTEE

Richard Briggs, Ph.D.

Roderick McColl, Ph.D.

Vikram Kodibagkar, Ph.D.

Matthew Lewis, Ph.D.

Wendy Ringe, Ph.D.

DEDICATION

To Nancy, in whom I find great delight.

I would like to thank my supervising professor, Dr. Roderick McColl, for giving me the opportunity to pursue this research. He gave me the latitude I needed to explore DTI and to come to the realization that there was room to improve the data quality with post-processing. I would also like to thank Dr. Richard Briggs who served as the chairman of my graduate committee. His encouragement to me and his input to my manuscript were invaluable. I am indebted to Dr. Wendy Ringe for her help with the organization of my manuscript and for her probing questions which challenged me to excel as a researcher. I thank Dr. Matthew Lewis for his model of insatiable curiosity as a scientist and Dr. Vikram Kodibagkar for pressing me to provide clearer substantiation for fundamental conclusions that I drew. Dr. Kaundinya Gopinath contributed greatly to my studies with his continual encouragement and participation in guiding me toward a research topic. Dr. Jeffrey Spence helped me to evaluate and select statistical methods, Dr. Xiufeng Li provided me with the pulse sequence diagrams from the Siemens scanner, Aman Goyal worked out the procedure for recording real and imaginary data for the DTI

scans and helped me with the volunteer scan, and Larry Steier generously agreed to be the subject for the volunteer DTI scan with intentional motion. I want to thank Dr. Robert Haley and Dr. Ron Peshock for their roles of encouragement and support in my studies. This study was supported by IDIQ contract VA549-P-0027, awarded and administered by the Department of Veterans Affairs Medical Center, Dallas, TX.

Graduate studies do not take place in a vacuum but in the context of life. The opportunity to devote myself to the pursuit of a Ph.D. has been a great privilege and a great help to me. It has been a privilege to be counted among the scholars of this institution and to have the attention of men and women of such excellence. I am humbled by the thought of what I have gained from so many. The pursuit of my Ph.D. has been a help to me in that it has given me the opportunity to contribute to the scientific community in a way that has increased my confidence and restored a sense of the significance of my contribution. In the course of this pursuit I have, of course, been helped by many outside the academic community as well. First among these is my wife Nancy who brings so much joy to my life and who has constantly supported me in my studies. My counselor, Ken, has spent many hours with me and helped bring perspective and hope in the darker days, as did my good friend, Eric Barnes. Above all, I have been sustained by the hope given to me by Jesus Christ. As my confidence of His attention and care has increased, so has my joy. Thanks be to God for His indescribable gift.

IMAGE PROCESSING CONSIDERATIONS FOR HIGH RESOLUTION
DIFFUSION TENSOR IMAGING OF THE HUMAN BRAINSTEM

By

KEITH MCLEOD HULSEY

DISSERTATION

Presented to the Faculty of the Graduate School of Biomedical Sciences

The University of Texas Southwestern Medical Center

In Partial Fulfillment of the Requirements

For the Degree of

DOCTOR OF PHILOSOPHY

The University of Texas Southwestern Medical Center

Dallas, Texas

May, 2012

IMAGE PROCESSING CONSIDERATIONS FOR HIGH RESOLUTION
DIFFUSION TENSOR IMAGING OF THE HUMAN BRAINSTEM

KEITH MCLEOD HULSEY, Ph.D.

The University of Texas Southwestern Medical Center, 2012

RODERICK W. MCCOLL, Ph.D.

Diffusion weighted MRI is used to measure the diffusivity of water in the human brain noninvasively. Diffusion tensor imaging (DTI) fits the diffusivity measurements from many directions to a tensor model of the diffusivity of water in brain tissue. DTI is particularly useful for interrogating the health and organization of white matter in the brain. The human brainstem has many white matter tracts that connect small nuclei in the brainstem to other regions of the brain. High resolution DTI of the brainstem may be helpful in understanding diseases that implicate brainstem nuclei. There are technical challenges for DTI which must be addressed to provide the most sensitive and meaningful measurements. Some of these challenges are: accurate registration between

diffusion weighted images, accurate fitting of the data to the tensor model, measuring significance of group differences using DTI results, and increasing image resolution. This study has focused on finding solutions for accurate fitting of data to the tensor model in the presence of signal void artifacts and on increasing image resolution beyond the point at which signal aliasing occurs. To meet the aims of this study I have; 1) developed an innovative approach to detect and remove signal void artifacts caused by subject motion, brain motion induced by cardiac pulsation and scanner vibration, 2) developed an innovative approach to mask aliased signal in DTI scans which have a field of view smaller than the subject's head, and 3) shown that removing signal void artifacts from the DTI scans acquired for the Gulf War Illness study produces significant changes in FA for most subjects in the study. Removing signal void artifacts from the Gulf War Illness study data did not, however, alter the conclusions of group comparisons for the samples of Gulf War veterans studied. Two conclusions of this study are that signal void artifacts should be removed from DTI data before conducting analysis and that an image with a field of view larger than the subject's head can be used to estimate the location of aliased signal in DTI scans acquired with fields of view smaller than the subject's head.

TABLE OF CONTENTS

LIST OF FIGURES	X
LIST OF TABLES	XIII
LIST OF APPENDICES	XV
LIST OF ABBREVIATIONS.....	XVI
1 INTRODUCTION	1
1.1 MEASUREMENT OF DIFFUSIVITY WITH MAGNETIC RESONANCE	1
1.2 DIFFUSION TENSOR IMAGING	6
1.3 SINGLE-SHOT ECHO PLANAR IMAGING.....	10
1.4 CHALLENGES THAT NEED ADDITIONAL WORK.....	12
1.4.1 ACCURATE REGISTRATION BETWEEN DIFFUSION WEIGHTED IMAGES	12
1.4.2 ACCURATE FITTING OF THE DATA TO THE TENSOR MODEL	17
1.4.3 MEASURING SIGNIFICANCE OF GROUP DIFFERENCES USING DTI RESULTS	41
1.4.4 INCREASING IMAGE RESOLUTION	43
2 AIMS	53
2.1 SPECIFIC AIMS FOR THIS STUDY	53

2.2 GENERAL APPROACH TO ACCOMPLISH AIMS	54
3 METHODS	57
3.1 SIMULATION OF DIFFUSION WEIGHTED IMAGES WITH SIGNAL VOID ARTIFACTS	57
3.2 DATA COLLECTION	61
3.3 DETECTION OF SIGNAL VOID ARTIFACTS	64
3.3.1 SIMULATION OF DIFFUSION-WEIGHTED SIGNAL USING RESTORE	65
3.3.2 DETECTION OF ARTIFACTS DUE TO VIBRATIONS	67
3.3.3 DETECTION OF ARTIFACTS OTHER THAN THOSE DUE TO VIBRATIONS.....	70
3.4 REDUCTION OF SIGNAL VOID ARTIFACTS.....	72
3.5 EFFECT OF ARTIFACT EXCLUSION ON FA.....	73
3.6 MITIGATING THE IMPACT OF ALIASED SIGNAL.....	76
3.7 TBSS ANALYSIS OF GWIS DATA.....	80
4 RESULTS	83
4.1 SIMULATION OF DTI SCANS WITH SIGNAL VOID ARTIFACTS.....	83
4.2 DETECTION OF SIGNAL VOID ARTIFACTS	89
4.2.1 DETECTION OF VIBRATION ARTIFACTS.....	89
4.2.2 DETECTION OF ARTIFACTS OTHER THAN VIBRATION ARTIFACTS	

FOR SIMULATED DATA.....	95
4.2.3 DETECTION OF ARTIFACTS OTHER THAN VIBRATION ARTIFACTS FOR WHOLE HEAD FOV DATA.....	97
4.2.4 DETECTION OF ARTIFACTS OTHER THAN VIBRATION ARTIFACTS FOR SMALL-FOV DATA.....	100
4.2.5 ADDITIONAL ARTIFACTS DETECTED WHILE SEARCHING FOR SIGNAL VOID ARTIFACTS	103
4.3 REMOVAL OF SIGNAL VOID ARTIFACTS.....	105
4.3.1 SIMULATION DATA	105
4.3.2 GWIS WHOLE HEAD FOV DTI DATA	107
4.3.3 GWIS SMALL-FOV DTI DATA.....	109
4.4 ALIASED SIGNAL MASKS FOR MEAN FA MAPS	110
4.5 REGISTRATION OF FA MAPS FOR SMALL-FOV DTI SCANS	111
4.6 RESULTS FOR GULF WAR ILLNESS STUDY DTI GROUP ANALYSIS	113
5 DISCUSSION AND CONCLUSIONS	125
5.1 DISCUSSION.....	125
5.2 CONCLUSIONS	136
5.3 FUTURE WORK	137

LIST OF FIGURES

FIGURE 1. STEJSKAL-TANNER SEQUENCE:	6
FIGURE 2. K-SPACE SHIFT OF ROTATING DISC:	19
FIGURE 3. DIFFUSION WEIGHTED VOLUME WITH SIGNAL VOID ARTIFACTS:	22
FIGURE 4. K-SPACE SHIFT OF SIGNAL VOID ARTIFACTS:	25
FIGURE 5. CARDIAC PULSATION-INDUCED SIGNAL VOID:.....	30
FIGURE 6. VIBRATION-INDUCED SIGNAL VOID:	33
FIGURE 7. LOCATION OF VIBRATION ARTIFACTS:.....	34
FIGURE 8. FLOW DIAGRAM OF RESTORE ALGORITHM:	38
FIGURE 9. THE LOCUS CERULEUS (LC) IN THE BRAINSTEM:	44
FIGURE 10. SIMULATED ALIASING OF A SMALL-FOV IMAGE:	51
FIGURE 11. ALIASING OF A SMALL-FOV IMAGE:	52
FIGURE 12. BRAIN MASK FOR IMAGE WITH ALIASED SIGNAL:	79
FIGURE 13. ROTATIONAL VELOCITY OF SIMULATED HEAD MOTION:.....	84
FIGURE 14. MASKS FOR CARDIAC PULSATION AND VIBRATION ARTIFACTS:	85
FIGURE 15. VIBRATION EFFECT USED FOR SIMULATING THE VIBRATION ARTIFACT:	85
FIGURE 16. SIMULATED NOISE:.....	87
FIGURE 17. SIMULATED MOTION-INDUCED SIGNAL VOID ARTIFACT:	88
FIGURE 18. FA MAP FROM SIMULATED DTI SCAN AND ORIGINAL FA:	89
FIGURE 19. VIBRATION EFFECT CALCULATED FROM THE SIMULATED DTI	

SCAN:.....	90
FIGURE 20. VIBRATION ARTIFACT DETECTION FOR SIMULATED IMAGE:	91
FIGURE 21. VIBRATION EFFECT CALCULATED FROM THE GWIS DTI SCAN FOR SEABEE GWS0018:.....	93
FIGURE 22. VIBRATION ARTIFACT DETECTION FOR GWIS SEABEE GWS0018:	94
FIGURE 23. LOCATION OF VIBRATION ARTIFACTS ON STANDARD BRAIN: ...	95
FIGURE 24. TWO ARTIFACTS OBSERVED IN GWIS DTI DATA:	104
FIGURE 25. IMPACT OF ARTIFACT REMOVAL ON SIMULATION FA:.....	105
FIGURE 26. IMPACT OF ARTIFACT REMOVAL ON FA FROM THE GWIS WHOLE HEAD FOV DTI SCAN FROM SUBJECT GWN0045:	108
FIGURE 27. REGION OF SMALL-FOV MEAN FA MAPS UNAFFECTED BY ALIASED SIGNAL:.....	111
FIGURE 28. REGISTRATION ERRORS IN NON-LINEAR REGISTRATION OF FA MAPS FROM SMALL-FOV DTI DATA:	112
FIGURE 29. REGISTRATION ERROR IN LINEAR REGISTRATION OF THE FA MAP FROM SMALL-FOV DTI DATA OF SUBJECT GWS0007:	113
FIGURE 30. SKELETONISED MASKS OF WHITE MATTER TRACTS:.....	114
FIGURE 31. WHITE MATTER TRACTS FOR WHICH THE CONTROL GROUP HAD GREATER FA THAN THE SYNDROME 2 GROUP:	116
FIGURE 32. COMPARISON OF FA FROM WHOLE HEAD FOV SCANS TO FA FROM SMALL-FOV SCANS:	118
FIGURE 33. WHITE MATTER TRACTS FOR WHICH THE NATIONAL SAMPLE	

HAD GREATER FA THAN THE SEABEES FOR THE SYNDROME 2

GROUPS:..... 120

FIGURE 34. VOXELS FOR WHICH THE SIGNIFICANCE OF FA DIFFERENCES

CHANGED WHEN ARTIFACTS WERE REMOVED: 124

LIST OF TABLES

TABLE 1. ROTATION ANGLES AND TRANSLATION DISTANCES FOR VOLUMES NEAR ARTIFACTS.....	26
TABLE 2. ROTATION ANGLES OF TEMPORALLY SEQUENTIAL SLICES FOR VOLUME 43	28
TABLE 3. REGRESSION METHODS USED IN DIFFUSION TENSOR ESTIMATION	36
TABLE 4. NUMBER OF SUBJECTS IN EACH GROUP IN GWIS	62
TABLE 5. AVERAGE AGE OF GWIS SEABEES PARTICIPANTS	82
TABLE 6. AVERAGE AGE OF GWIS NATIONAL SAMPLE PARTICIPANTS	82
TABLE 7. VISUALLY DETECTED ARTIFACTS IN SIMULATED DTI SCAN.....	88
TABLE 8. COEFFICIENTS FOR VIBRATION ARTIFACT CO-REGRESSOR IN GWIS.	92
TABLE 9. VISUAL EVALUATION OF FLAGGED SLICES FOR SIMULATED DTI SCAN.....	97
TABLE 10. VISUAL EVALUATION OF FLAGGED SLICES FOR WHOLE HEAD FOV GWIS DTI SCANS.....	99
TABLE 11. VISUAL EVALUATION OF FLAGGED SLICES FOR SMALL-FOV GWIS DTI SCANS.....	101
TABLE 12: MAXIMUM FA DIFFERENCES BETWEEN SIMULATIONS AND ORIGINAL TENSORS.....	106
TABLE 13: COMPARISONS OF FA DEVIATION FROM ORIGINAL BETWEEN SIMULATIONS	106

TABLE 14. ROTATION ANGLES AND TRANSLATION DISTANCES FOR VOLUMES IN NATIONAL SAMPLE SUBJECT GWN0045.....	108
TABLE 15. MINIMUM P VALUES FOR SIGNIFICANCE OF FA DIFFERENCES BETWEEN SUB-GROUPS.....	115
TABLE 16. MINIMUM P VALUES FOR SIGNIFICANCE OF FA DIFFERENCES BETWEEN THE CONTROLS AND SYNDROME GROUPS.	117
TABLE 17. MINIMUM P VALUES FOR SIGNIFICANCE OF FA DIFFERENCES BETWEEN THE WHOLE HEAD FOV SCANS AND THE SMALL-FOV SCANS.....	119
TABLE 18. MINIMUM P VALUES FOR SIGNIFICANCE OF FA DIFFERENCES BETWEEN THE NATIONAL SAMPLE AND THE SEABEES.....	121
TABLE 19. MINIMUM P VALUES FOR SIGNIFICANCE OF FA DIFFERENCES BETWEEN THE CONTROLS AND SYNDROME GROUPS WHEN SIGNAL VOID WAS NOT REMOVED.	123
TABLE 20. COMPARISON OF NUMBER OF VOXELS SHOWING SIGNIFICANT DIFFERENCES BETWEEN CONTROLS AND SYNDROME 2 FOR THE SEABEES.	124

LIST OF APPENDICES

APPENDIX A: DIFFUSION WEIGHTING VECTORS	139
APPENDIX B: SCRIPTS FOR SIMULATION OF MOTION-INDUCED SIGNAL VOID ARTIFACTS	142
APPENDIX C: SCRIPT FOR ESTIMATING EXPECTED SIGNAL IN A DIFFUSION WEIGHTED IMAGE	171
APPENDIX D: SCRIPTS FOR DETECTING VIBRATION-INDUCED SIGNAL VOID ARTIFACTS	175
APPENDIX E: SCRIPTS FOR DETECTING OTHER SIGNAL VOID ARTIFACTS ..	183
APPENDIX F: SCRIPTS FOR REMOVING SIGNAL VOID ARTIFACTS	200
APPENDIX G: SCRIPTS FOR QUANTIFYING FA CHANGES OF SIMULATED DTI SCAN.....	206
APPENDIX H: SCRIPTS FOR QUANTIFYING FA CHANGES OF GWIS DTI SCANS	215
APPENDIX I: SCRIPTS FOR GENERATING SMALL-FOV MASKS	223
APPENDIX J: MAXIMUM FA CHANGES FOR WHOLE HEAD GWIS DTI SCANS	232
APPENDIX K: MAXIMUM FA CHANGES FOR SMALL-FOV GWIS DTI SCANS	242

LIST OF DEFINITIONS

ADC - Apparent Diffusion Coefficient

BET - Brain Extraction Tool

DTI - Diffusion Tensor Imaging

DWI – Diffusion Weighted Image

EPI - Echo Planar Imaging

FA - Fractional Anisotropy

FACT - Fiber Assignment by Continuous Tracking

FSL - FMRI Brain Software Library

GWIS - Gulf War Illness Study

LC - Locus Ceruleus

MD - Mean Diffusivity

MR - Magnetic Resonance

MRI - Magnetic Resonance Imaging

PFG - Pulsed Field Gradient

rf - Radio Frequency

ROI - Region Of Interest

SNR - Signal to Noise Ratio

TBSS – Tract-Based Spatial Statistics

TE - Echo Time

TRSE – Twice-Refocused Spin Echo

CHAPTER ONE

INTRODUCTION

Diffusion tensor imaging (DTI) is a fast, high resolution, non-invasive technique which is useful for characterizing the degree and directional dependence of water diffusivity in the human brain. The research presented in this thesis addresses considerations of image artifacts due to brain motion during diffusion sensitization and image artifacts due to acquiring images with an in-plane field of view smaller than the subject head.

1.1 Measurement of Diffusivity with Magnetic Resonance

Diffusion is a key mechanism for the transport of biologically important molecules and ions within cell environments, across cell membranes and within cells. The proper function of cells depends upon the cell's ability to selectively control the concentrations of these molecules and ions by restricting passive diffusion across membranes and by actively transporting selected molecules and ions across those same membranes in accordance with the cell's needs. Diffusion of any given substance in a biological tissue is highly dependent on barriers to random motion, such as impermeable or semi-permeable membranes, on the concentration gradients of that substance, on attraction to or repulsion from other molecules, and on chemical reactions with other molecules. Since diffusion within a tissue is strongly influenced by the function and health of the cells in that tissue, it is useful to characterize diffusion when studying the

health of certain tissues.

An understanding of diffusion in biological tissues can be developed from the physics of diffusion and from a characterization of the constraints on that diffusion. In 1828, Robert Brown observed the random motion of pollen grains under a microscope (Brown 1828). Einstein later attributed that motion to random interactions that the pollen had with the water molecules in which the pollen was suspended. He characterized the motion of single molecules using the random walk model in 1905 and related that motion to diffusion (Einstein 1956). He provided calculations to show that the displacements of diffusing particles in a given period of time form a Gaussian distribution. He calculated the average displacement to be

$$\lambda_x = \sqrt{\langle x^2 \rangle} = \sqrt{2D\Delta} \quad (1)$$

where: $\langle x^2 \rangle$ is the average squared particle displacement,

D is the diffusion coefficient and

Δ is the diffusion time.

Equation 1 characterizes diffusion for molecules which are unobstructed by barriers. When the random walk behavior is complicated by barriers, the model must be adjusted. Diffusion can be characterized as following one of three models; free, hindered (Beaulieu 2002), or restricted (LeBihan and Bassier 1995; Assaf, Freidlin et al. 2004). Free diffusion refers to motion that is unobstructed by barriers. Hindered diffusion occurs when obstacles are present which interact with the diffusing molecules by blocking them or attracting them. Restricted diffusion occurs when boundaries are present which the diffusing molecules cannot penetrate in the time scale of the observation. As a result, it is

clear that the diffusion of molecules in a tissue cannot simply be characterized by the bulk diffusivity, but it must rather be characterized by an apparent diffusion coefficient (ADC) which is dependent on the microenvironment, on the direction considered, and on the time frame over which the diffusion is being described. Direct observation of diffusion in a tissue would provide a measure of the influence these cell structures have on molecular diffusion and may provide clues to tissue health.

Non-invasive measurements of diffusion in biological tissues can be obtained using magnetic resonance (MR). Due to the abundance of water in tissue and the relative ease of probing hydrogen nuclei with MR, the most common measurement of diffusion in tissue using MR is of water. Without causing damage to the tissue, an ADC for water in the tissue can be calculated. An MR signal from biological tissues can be obtained by manipulating the magnetic spins of hydrogen nuclei and detecting the oscillating net magnetization of the nuclei as it precesses about the applied static magnetic field. The precession frequency for an individual hydrogen nucleus, also called the Larmor frequency ω_0 , is determined by the gyromagnetic ratio γ of the nucleus and the strength of the external magnetic field B_0 (Liang and Lauterbur 2000): $\omega_0 = \gamma B_0$.

An externally applied oscillating magnetic field, referred to as a radio frequency (rf) pulse, is used to reorient the net magnetization of the sample from being aligned with the external magnetic field to a vector that precesses about the external magnetic field at an angle determined by the amplitude and duration of the rf pulse. The degree of rotation of the net magnetization is used to characterize the rf pulse such that a 90 degree pulse rotates the magnetization by 90 degrees and a 180 degree pulse inverts the direction of the magnetization. The effect of a 90 degree pulse on magnetization

aligned with the external field is to rotate that magnetization into the plane perpendicular to the external field, at which point the direction of the magnetization precesses about the external magnetic field. The oscillating magnetization can then be detected with coils tuned to the Larmor frequency. The coherence of the precession is disturbed by any differences in the magnetic field which the individual hydrogen nuclei experience. As the signal from the nuclei becomes less coherent, the detectable signal attenuates as some nuclei precess faster than others. The incoherence caused by variation in precessional frequencies can be reversed if the field differences are static. This is accomplished by applying a 180 degree rf pulse which inverts the direction of the net magnetization. The time between the 90 degree pulse and the 180 degree refocusing pulse is $TE/2$. After an additional delay of $TE/2$, the variation in the precessional frequencies restores the coherence of the magnetization of the individual nuclei. The reappearance of the coherent signal is referred to as a spin echo which occurs at the echo time (TE).

By applying a spatially varying magnetic field, the Larmor frequency of the nuclei becomes spatially varying. This allows for spatially encoding the signal with a gradient of the static field. If the strength B_0 of the static magnetic field is modulated with a linear gradient G_x , then the spatially dependent Larmor frequency has the following relationship (Liang and Lauterbur 2000): $\omega(x) = \omega_0 + \gamma G_x x$.

A method for directly measuring the diffusion coefficient of molecules in a sample using MR was proposed by Carr and Purcell in 1954 (Carr and Purcell 1954). It was demonstrated that the MR signal was attenuated due to the random displacement of diffusing molecules in a static magnetic field gradient. This signal attenuation results from the phase dispersion that occurs among excited nuclei as they independently

accumulate phase at slightly different frequencies depending upon their position within a spatially varying magnetic field. For stationary nuclei, this spatial encoding can be reversed by applying a 180 degree rf pulse to reverse the accumulated phase. For non-stationary nuclei, the spatial encoding cannot be completely reversed because the nuclei have randomly moved to new locations with different static fields and frequencies. By comparing the signal when the diffusion sensitizing gradients are applied with the signal when the gradients are not applied, the mean displacement of molecules during the period of diffusion sensitization can be calculated.

In 1965, Stejskal and Tanner introduced the pulsed field gradient (PFG) sequence for measuring diffusion (Stejskal and Tanner 1965). This sequence added the advantage of precisely controlling the interval over which diffusion is measured. They provided the mathematical analysis and experimental evidence that the attenuation of the MR signal due to diffusion follows the relationship

$$\ln[S(TE)/S(0)] = -\gamma^2 D \delta^2 (\Delta - \delta/3) G_d^2 \quad (2)$$

where: $S(TE)$ is the signal amplitude at the spin echo,

$S(0)$ is the signal amplitude at time 0,

γ is the gyromagnetic ratio,

D is the diffusion coefficient,

δ is the duration of the pulsed field gradients,

Δ is the separation of the pulsed field gradients,

$$G_d = \sqrt{G_x^2 + G_y^2 + G_z^2}, \text{ and}$$

G_x is the magnitude of the pulsed field gradient in the x direction.

A diagram of the Stejskal Tanner sequence is presented in Figure 1.

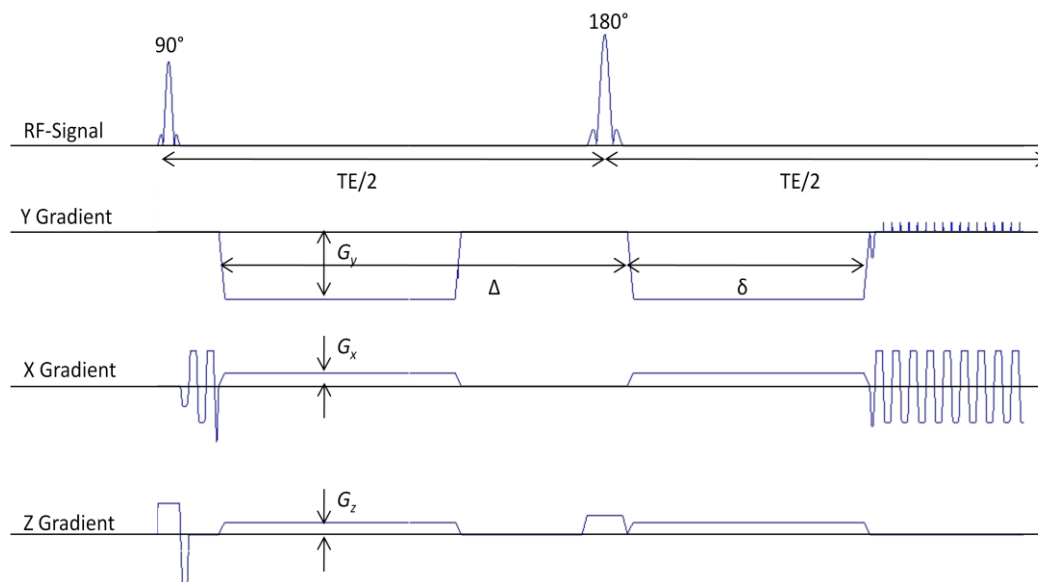


Figure 1. Stejskal-Tanner Sequence: A sequence diagram of a Stejskal-Tanner PFG diffusion weighted experiment with EPI readout as output from the software used with a Siemens Magnetom Trio TIM 3T scanner. (The readout is truncated in this diagram).

1.2 Diffusion Tensor Imaging

Diffusion which is independent of direction is referred to as isotropic. Diffusion in tissue often has directional dependence and is referred to as anisotropic. The ADC calculated using diffusion sensitized MR is direction dependent whenever the diffusivity being measured is anisotropic due to the microstructure of the tissue. This directional dependence can be exploited to gain additional information about diffusivity in a sample. One biological tissue which is known to have dramatic directional dependence for the ADC measurements is white matter brain tissue. White matter tissue is composed of long narrow neuronal axons and of other supporting tissues. Oligodendrocytes are cells in the supporting tissue which form a myelin sheath around

axons. The impact that the long cylindrical axon membranes and the myelin sheaths have on diffusivity is that they allow water to diffuse easily along the direction of the axons but hinder it from diffusing in other directions. The orientation of axons in a local region of white matter tends to be homogeneous as axons are often bundled to form white matter tracts (Beaulieu 2002). Careful interrogation of the diffusivity within a white matter tract will provide information about its orientation. Increasing the number of directions sampled allows for finer directional information to be gained and the noise characteristics of diffusion measurements are improved (Zhan, Leow et al. 2010). However, increasing the number of direction dependent ADC measurements makes the task of interpreting the results more complex.

Interpretation of a multi-directional collection of ADC is facilitated by reducing the degrees of freedom in the data by using a conceptually manageable model. The model most frequently used in diffusion weighted MR is the tensor. A tensor models the diffusion as having independent diffusivity in three orthogonal directions (Basser, Mattiello et al. 1994). The tensor describes the magnitude of diffusion in each of these directions and is written as a 3x3 symmetric matrix (Jones 2009). By grouping the sequence dependent variables of Equation 2 into a factor “ b ” and designating the signal at the echo as S_b , Equation 2 can be rewritten as

$$\ln S_{(b)} = \ln S_{(0)} - \mathbf{bD} \quad (3)$$

where: $S_{(b)}$ is the diffusion weighted signal for vector \mathbf{b} ,
 $S_{(0)}$ is the non-diffusion weighted signal,
 \mathbf{D} is a tensor modeling the diffusion, and

\mathbf{b} is a vector describing the diffusion weighting.

Estimates of the ADC from six non-collinear directions are required to solve the tensor equation, although often many more than six directions are used. The tensor model has been developed to provide several rotationally independent quantities that are useful for quantifying and comparing characteristics of diffusion. Mean diffusivity (MD) is useful as a quantitative measure of the average diffusivity. Fractional anisotropy (FA) is a useful indicator of how directionally dependent the diffusion is (Jones 2009). In addition to the rotationally independent quantities, the eigenvectors of the tensor provide directional information about the diffusivity. General equations for MD and FA are:

$$MD = \frac{D_{xx} + D_{yy} + D_{zz}}{3}$$

$$FA = \sqrt{\frac{3}{2}} * \frac{\sqrt{(\lambda_1 - \langle \lambda \rangle)^2 + (\lambda_2 - \langle \lambda \rangle)^2 + (\lambda_3 - \langle \lambda \rangle)^2}}{\sqrt{\lambda_1^2 + \lambda_2^2 + \lambda_3^2}}$$

Reducing the multi-directional data to a single model facilitates interpretation, but there are some disadvantages to forcing the data to fit a simplifying model.

The tensor model is able to represent a single pool of diffusing molecules within the sampled tissue. Restricting the characterization of diffusion to a single tensor excludes the possibility of modeling complex tissue structure such as crossing axon fibers. Other models are available such as q-ball and tensor distributions (Tournier, Mori et al. 2011). These models can provide a more complete accounting of tissue microstructure than the tensor model does. However, analysis tools that utilize the single tensor model, such as tract-based spatial statistics (TBSS) (Behrens, Woolrich et al. 2003) and fiber assignment by continuous tracking (FACT) (Mori, Crain et al. 1999), are well established. Therefore, with these well defined analysis tools, the tensor model has

continued to play a large role in diffusion weighted studies. A tensor model of the diffusivity of water in tissue facilitates analysis, but spatial localization of the tensor estimate is required to model tissue diffusivity as it changes rapidly over distances of millimeters.

Two dimensional (2D) MR imaging (MRI) can be used to localize the measurements of diffusivity. 2D MRI utilizes the technique of exciting only nuclei in a slice of defined thickness along an imaging plane and then spatially encoding the signal in that volume by applying magnetic field gradients in the remaining two orthogonal directions. Measurements of the magnitude and phase of the signal from the slice are made while varying the spatial encoding. These measurements are combined mathematically to reconstruct a map of the signal from each volume element (voxel). The spatially encoded measurements are represented in a complex Cartesian space referred to as the frequency domain or as k-space. K-space is related to physical space through the two dimensional Fourier Transform.

$$S(k_x, k_y) = \int_{-\infty}^{+\infty} \int_{-\infty}^{+\infty} \rho(x, y) e^{-i2\pi(k_x x + k_y y)} dx dy \quad (4)$$

where: k_x and k_y are the k-space coordinates of the spatial encoding,
 $S(k_x, k_y)$ is the complex signal at position k_x, k_y in k-space, and
 $\rho(x, y)$ is the signal from the slice at position x, y when no spatial encoding has been applied.

If the signal is sampled on a rectangular grid in k-space, then an image can be reconstructed from the sampled data using the Discrete Fourier Transform.

$$I(j, k) = \sum_{m=-\frac{M}{2}}^{\frac{M}{2}-1} \sum_{n=-\frac{N}{2}}^{\frac{N}{2}-1} S(m, n) e^{i2\pi(\frac{kn}{N} + \frac{jm}{M})} \quad (5)$$

where: M and N are the numbers of samples in the k_x and k_y dimensions of k-space

$j, k, m,$ and n are integers with $-M/2 \leq j < M/2$, $-N/2 \leq k < N/2$

$I(j, k)$ is the reconstructed signal for position $x=j/(M*\Delta k_x), y=k/(N*\Delta k_y)$

$S(m, n)$ is the signal at k-space coordinates $k_x=m*\Delta k_x, k_y=n*\Delta k_y$

Adjacent 2D images are stacked to form three dimensional (3D) volumes. Diffusion tensor imaging (DTI) uses diffusion weighted volumes to calculate a 3D map of the diffusion tensors representing tissue diffusivity at each location in the brain. The process of sampling the signal $S(k_x, k_y)$ and converting these samples into an image does not require that the samples all be acquired after a single excitation, but it does require that all the samples have a consistent phase relationship. Subject motion during diffusion encoding will introduce phase components which will undermine this consistency.

1.3 Single-Shot Echo Planar Imaging

The object signal before spatial encoding $\rho(x, y)$ used in Equation 4 has both a magnitude and a phase component. For proper reconstruction of image $I(j, k)$, all the samples of the spatially encoded signal $S(k_x, k_y)$ must come from a consistent $\rho(x, y)$. However, motion during diffusion weighting adds an additional phase component to $\rho(x, y)$ which can change each time the diffusion weighting gradients are applied. If the sample moves during diffusion sensitization with a constant linear velocity, the signal will pick up a phase of (Wedeen, Weisskoff et al. 1994):

$$\varphi = \mathbf{K}_v \cdot \mathbf{V} \quad (6)$$

where: \mathbf{V} is the constant velocity and

\mathbf{K}_v is the velocity sensitivity of the MR sequence.

If several excitations are required to fill k-space, then the signal $S(k_x, k_y)$ will have inconsistent phase information and the reconstructed image will exhibit artifacts (Pipe 2009). Several approaches are available to correct for the phase differences produced by differences of bulk motion between excitations. Many include making estimates of the phase addition for each excitation and correcting for it. The most widely used approach to limit the dispersion of phase in k-space is to collect all of k-space after a single excitation pulse (Pipe 2009). The single shot echo planar imaging (EPI) readout collects all signal for a 2D image after a single excitation.

In order to image the human brain, several parallel 2D slices are imaged consecutively to cover the whole brain and the images are stacked to form a 3D volume. The signal from a slice must be sampled before it decays to the noise level which occurs on the order of 100 msec. For the example of slices 2 mm thick, 64 slices cover a field of view of 128 mm which is sufficient to cover the brain. Therefore it would take about 6.4 seconds to acquire a single 3D volume of the whole brain. To fit a tensor for each voxel, a minimum of six 3D volumes with different diffusion directions must be acquired as well as a reference volume that has no diffusion weighting. This allows a complete DTI scan to be completed in less than a minute. In practice, for signal to noise and for modeling considerations, many more than six directions are sampled and more than one reference volume is acquired. Imaging times of 5 to 10 minutes are common for DTI scans. (A 3D-image will be referred to here as a volume, and all the volumes collected for a diffusion

tensor experiment will be referred to as a DTI scan.)

1.4 Challenges That Need Additional Work

Diffusion weighted MRI provides us with the ability to measure the local diffusivity of water in the human brain noninvasively in a matter of minutes. This information is very useful for clinical work, as in assessing stroke (van Gelderen, de Vleeschouwer et al. 1994), and in research, as in characterizing white matter changes between groups (Smith, Jenkinson et al. 2006) and in tracing paths for white matter tracts (Mori, Crain et al. 1999; Behrens, Berg et al. 2007). However, there have been significant technical challenges which had to be faced in order to get meaningful results. Some of these challenges which are still in need of additional work include: accurate registration between diffusion weighted images (DWI), accurate fitting of the data to the tensor model, measuring significance of group differences using DTI results, and increasing image resolution. These will be addressed in the following sections.

1.4.1 Accurate registration between diffusion weighted images

Diffusion tensor modeling algorithms combine data from at least six directionally independent measurements of the diffusion weighted signal with data from one or more non-diffusion weighted measurements. A diffusion tensor is calculated for each image voxel. To provide a meaningful model of diffusion, the measurements provided to the algorithm for a given voxel must be measurements from the same anatomical location. Subject motion and geometric distortions cause the anatomical placement of voxels to be slightly different for each diffusion weighted volume. Proper image registration is required to insure that corresponding voxels contain signal from the

same anatomical location. Accurate registration between diffusion weighted images requires correcting for subject motion and correcting for changes in geometric distortion between images.

The first component of accurate image registration is correcting for subject motion between volumes. A diffusion weighted volume typically requires several seconds to be acquired. Subject motion on the order of the voxel size, typically 2 mm, is often observed. Subject motion changes the orientation of the head but not the size or shape. Such motion can be characterized using the six degrees of freedom associated with rotation and translation. A linear transformation is sufficient to co-register volumes with inter-image motion. Calculation of the linear transform required to co-register images can be accomplished by minimizing a cost function that compares the images (Jenkinson and Smith 2001). If motion occurs during the time a single volume is being acquired, the inter slice motion cannot be corrected with a single linear transform of the whole volume. To correct for that motion, slice to slice registration must be performed to generate a consistent orientation for the slices within the volume.

The second component of accurate image registration is correcting for geometric distortions between images. The acquisition of diffusion weighted images requires the rapid application of strong field gradients. Changing magnetic fields induce eddy currents in conductors. The strength and duration of the induced currents depend on how quickly the magnetic field is changing and on the characteristics of the conductors. The eddy currents that result from application of diffusion weighting gradients are strong enough and last long enough to produce image distortion (Ahn and Cho 1991; Haselgrove and Moore 1996).

Eddy current induced image distortion arises from the additional field gradient emanating from the eddy current persisting during signal readout. These gradients have the effect of distorting the sampling of k-space. Because the diffusion weighting gradients are applied in different directions for each volume, the eddy currents will be different and the distortion of k-space sampling will depend on the applied field gradient. Haselgrove explains that residual gradient fields from eddy currents impact the position of the reconstructed image in the phase encoding direction (Haselgrove and Moore 1996). He breaks down the effects into three categories; 1) residual gradient along the slice direction which induces a shift of the image in the phase encoding direction, 2) residual gradient along the frequency encoding direction which induces a shift in the phase encoding direction that varies with position in the frequency encoding direction, resulting in image shear., and 3) residual gradient in the phase encoding direction which produces a scaling of the image in that direction. Haselgrove proposed a correction for images distorted by eddy currents. The process compared a diffusion weighted image with the reference image which has no diffusion weighting. By correcting for magnification, shear distortion and translation, he was able to reduce the eddy current distortion. This solution does not account for the eddy current decay characteristics. A better approach would be to reduce the distortion during data collection.

Careful design of the diffusion weighting gradient waveform can be incorporated into the DTI sequence to reduce the effects of eddy currents. Alexander introduced a bipolar gradient waveform and demonstrated a reduction in image distortion (Alexander, Tsuruda et al. 1997). This approach uses the fact that changes in the gradient of opposite sign counteract each other and effectively eliminate the eddy currents and

their effects. The correction is not complete, however, because the bipolar gradients are necessarily applied at different times, and the eddy currents from the first pulse decay some amount before the counteracting eddy currents come into play. Reese introduced a twice-refocused spin echo (TRSE) sequence which uses two refocusing rf pulses to provide more control over the magnitudes of the counteracting eddy currents (Reese, Heid et al. 2003). Reese models the effects of eddy currents as exponentially decaying gradients. Tuning his sequence for the apparent decay constant of the eddy currents, he was able to reduce the effects of eddy currents without a large impact on image noise characteristics or contrast. However, the model of mono exponential decay is incomplete for characterizing eddy currents and therefore, when using this correction method, residual distortion remains.

After sequence adjustments are in place, additional improvement is still available through post processing of the images. At this point an algorithm such as the one described by Haselgrove may provide the needed improvement. However, Haselgrove's approach does not account for the effects of decay of the eddy currents. Truong proposed mapping the eddy current phase distortion of a phantom as a function of time to characterize the eddy currents of a scanner (Truong, Chen et al. 2011). A phase correction could then be applied to the Fourier Transform of the diffusion weighted image. The correction would be calculated based on the amount of distortion that occurred at the time a particular sample in k-space was collected. Truong reported good distortion correction and noted that the scanner characterization was stable over many months. Although careful modeling of the eddy current effects can help remove them when subject motion is carefully controlled, when subject motion occurs, the geometric

effects produced by the motion must also be corrected. A common approach to correct for eddy current distortion and subject motion is to use a single affine transform to correct for both. This is a combination of the linear transform approach for motion using six degrees of freedom and the Haselgrove approach for eddy current correction using a linear transform with three degrees of freedom.

The FMRI Brain Software Library (FSL) (Smith, Jenkinson et al. 2004) has a tool which corrects for eddy current distortion and the image misregistration due to subject motion. The EDDY_CORRECT algorithm of FSL calculates and applies the affine transforms which register each volume in a DTI scan to a common template, typically the first non-diffusion weighted volume of the scan. Jones has pointed out that a single transform for correction of eddy current and motion effects between the volumes of a DTI scan is not sufficient (Jones and Cercignani 2010). However, registering single slices to a reference volume is difficult because of uncertainties introduced by noise. Because of the difficulty of registering single slices to a whole volume, the availability of software such as the EDDY_CORRECT algorithm, and the conceptual simplicity of applying a single affine transform, the single affine transform is widely used for subject motion and eddy current correction of DTI scans. Residual errors remain due to non-linear effects of eddy current decay, intra-volume motion, and contrast mismatch between the volume being corrected and the template volume. In addition, Nam addressed the issue of the difficulty of registering a diffusion weighted image to a non-diffusion weighted template (Nam and Park 2011). He devised an approach to register the measured diffusion weighted volumes to simulated volumes that were derived from an estimate of the tensors. An iterative process was used to improve the correction. Although

Nam addressed the problem of registering images with different contrasts, the issue of eddy current decay is still not addressed. A definitive resolution to the challenge of accurate image registration is still being pursued in the image processing community. Good anatomical registration of images is required to ensure that the proper data are used, but it is also important to provide a robust way of fitting the tensor model with data that may contain noise and artifacts.

1.4.2 Accurate fitting of the data to the tensor model

When more than six diffusion weighted images are collected, solving the tensor equation becomes an over-constrained problem. Fitting data to a model, such as a tensor, is generally accomplished by minimizing an error function. In the case of fitting diffusion data to a tensor, the linear least squared errors approach fits the equation $\ln S_{(\mathbf{b})} = \ln S_{(0)} - \mathbf{bD}$ by minimizing the term (Basser, Mattiello et al. 1994; Chang, Jones et al. 2005)

$$\chi^2 = \sum_i \omega_i \times (y_i - y(x_i))^2$$

$$\text{where: } \omega_i = \frac{(S_{(\mathbf{b})})^2}{\sigma^2},$$

$S_{(\mathbf{b})}$ is the measured signal,

y_i is the log of the measured signal,

$y(x_i)$ is the log of the modeled signal and

σ is the standard deviation of the signal.

As long as the noise in the system is well behaved, the solution is robust. However, a single error in the data can skew the result if that error is large. Artifacts in DTI data can have a profound impact on the tensor model with a single artifact

introducing significant bias. Artifacts attributable to subject motion, physiologically induced motion and vibration frequently appear in DTI scans.

1.4.2.1 Errors from subject motion artifacts

Diffusion weighted imaging is particularly susceptible to rotational subject motion. Wedeen showed that subject motion can produce signal void in MRI (Wedeen, Weisskoff et al. 1994). As indicated in Equation 6, motion introduces a velocity dependent phase component to diffusion weighted images. Therefore, if there is a dispersion of velocities within a voxel, this will cause a dispersion of the phase from individual contributions to the signal from that voxel. As the phase dispersion approaches and exceeds π radian/voxel, the signal drops off very rapidly due to incoherence of the signal within the voxel. Wedeen noted an all-or-none effect at that point. His simulation of this artifact for a rotating disc is displayed in Figure 2. This figure also presents a magnitude image of k-space which shows the shift of power away from the center of k-space as the rotational velocity increases.

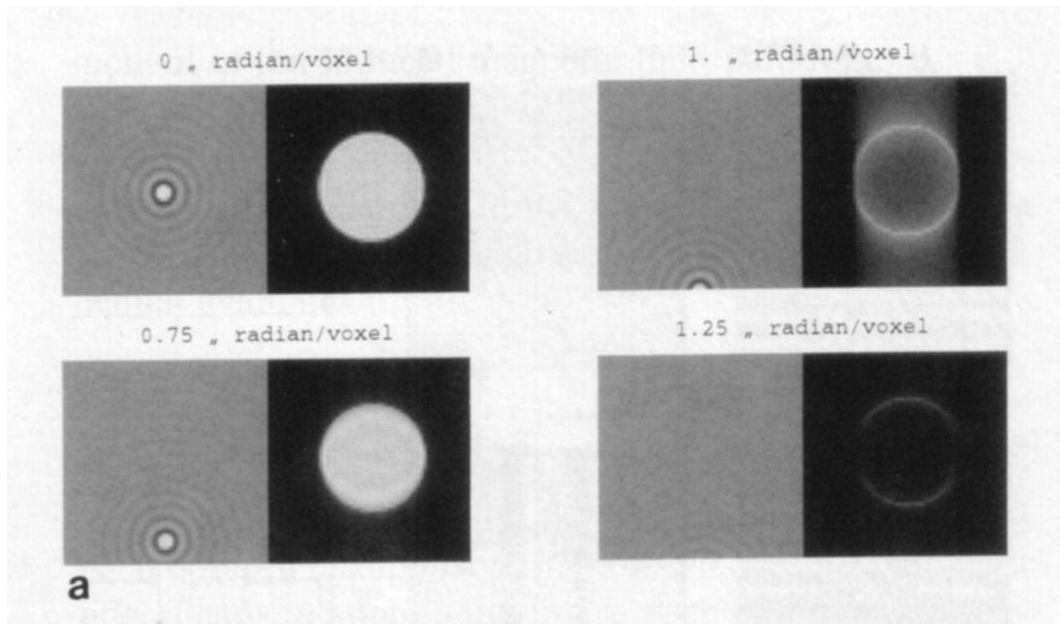


Figure 2. K-space shift of rotating disc: Simulations conducted by Wedeen demonstrating the k-space shift for a disc rotating at four different speeds and the resulting signal void artifact of the reconstructed image. Used, with permission, from: Wedeen, V. J., R. M. Weisskoff, et al. (1994). "MRI signal void due to in-plane motion is all-or-none." Magn Reson Med 32(1): 116-120.

Storey further investigated the affect of rotational velocities on diffusion weighted single-shot EPI reconstructed from partial k-space. He found that rotational velocities of $\sim 4^\circ/\text{sec}$ were sufficient to cause signal void artifacts for typical scanning parameters (Storey, Frigo et al. 2007). The effect of a spatially linear phase accumulation, such as is caused by rotational velocities, is to shift the location of the echo in k-space. When the center of the echo falls outside of the region of k-space being acquired, the intensity drops off dramatically. When the diffusion sensitization is in the frequency encoding direction, in-plane rotational motion causes the k-space to shift in the phase encoding direction. Partial-Fourier acquisition does not sample the extreme part of k-

space in the negative phase encode direction. Less of a shift in that direction of k-space is required for the echo to fall outside the sampled region than is required in other directions. The equation Storey presented for phase accumulation φ of a moving object during a once refocused Stejskal Tanner sequence is (Storey, Frigo et al. 2007):

$$\varphi = \gamma \mathbf{v} \cdot \mathbf{G} \delta_{dur} \Delta_{sep}$$

where: γ is the gyromagnetic ratio,

\mathbf{v} is the velocity of the object,

\mathbf{G} is the diffusion sensitizing gradient pulse,

δ_{dur} is the duration of the gradient pulse, and

Δ_{sep} is the separation between the diffusion sensitizing gradient pulses.

The gradient of the phase accumulation $\nabla \varphi$ due to rotational motion and the shift in k-space Δk_y due to rotational motion in the axial direction during diffusion sensitization in the x direction are (Storey, Frigo et al. 2007):

$$\nabla \varphi = \gamma \mathbf{G} \times \boldsymbol{\Omega}_{rot} \delta_{dur} \Delta_{sep} \quad (7)$$

$$\Delta k_y = -\gamma G_x \Omega_z \delta_{dur} \Delta_{sep} \quad (8)$$

where: $\boldsymbol{\Omega}_{rot}$ is the angular velocity of rotation,

Ω_z is the axial component of the angular velocity, and

G_x is the x component of the gradient.

The occurrence of artifacts caused by head rotation was demonstrated at UT Southwestern Medical Center when a healthy volunteer was scanned on a Siemens

Magnetom Trio Total Imaging Matrix (TIM) 3T scanner. The DTI sequence parameters were: FA=90 deg, TR/TE=8300/82, 2mm x 2mm x 2mm resolution, a 2D EPI readout with pixel bandwidth=1395 Hz, acquisition matrix of 80 x 128 reconstructed to 128 x 128 samples, GRAPPA acceleration factor=2, number of reference lines for parallel imaging=38, partial k-space reconstruction=6/8, and 64 2mm thick slices. The DTI scan consisted of 6 reference images with $b=0$ and 50 diffusion weighted images with non-collinear diffusion directions and $b=1000 \text{ s/mm}^2$. Vectors for the 50 directions are given in Appendix A. The volunteer intentionally moved his head when instructed to do so. Image slices from volume 43 of that demonstration, during which the subject shook his head, are presented here in Figure 3. The slices of the whole volume are presented as a mosaic where anatomically sequential slices are ordered left to right then top to bottom. Since the volume was collected in an interleaved order, temporally sequential slices are separated from each other horizontally by one slice of the alternate interleave. The motion artifact appears as large dark areas of an image slice. Within the dark regions, the normal brain structure appears to be missing, or to be obscured by image noise. In several slices of this example, the whole slice is affected, obscuring nearly all information in the slice. The artifacts in this example are spread over several temporally adjacent slices.

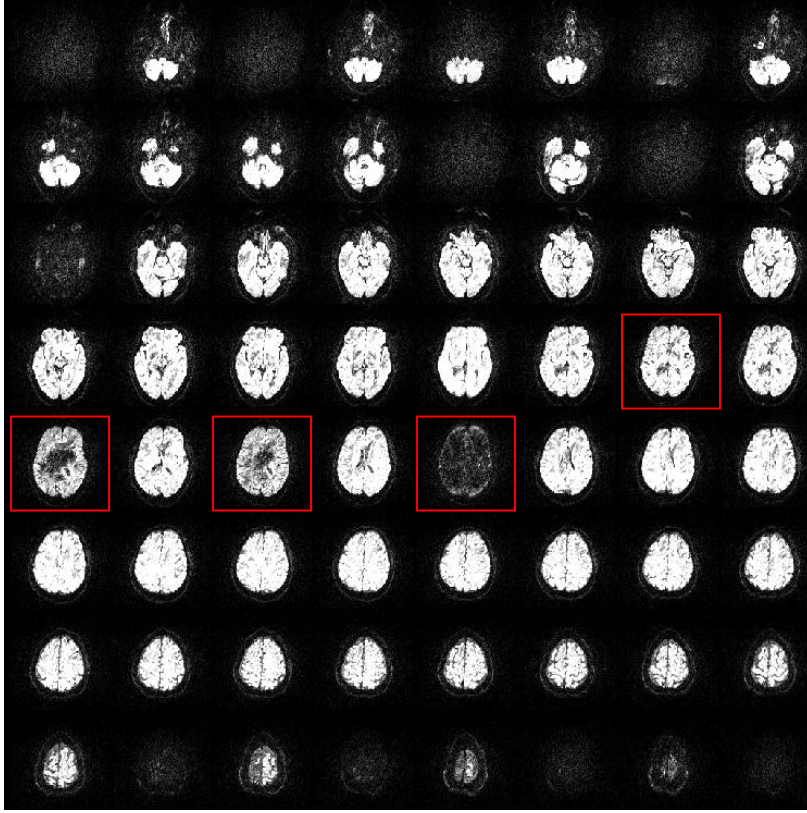


Figure 3. Diffusion weighted volume with signal void artifacts: A diffusion weighted volume with signal void artifacts evident in several slices. The red boxes indicate slices 30, 32, 34, and 36 which were used for further analysis. (Slice numbering starts with 0.)

The diffusion gradient parameters of a sequence similar to that used to collect the images of Figure 3, but with a diffusion weighting in the frequency encoding direction, are:

$$\Delta y = 2mm$$

$$N=128$$

$$\Delta k_y = 1/(N * \Delta y) \approx 3.9m^{-1}$$

$$\max(k_y) = (1/2)N\Delta k_y = 250m^{-1}$$

$$\min(k_y) = -(1/4)N\Delta k_y = -125m^{-1} \text{ (only 1/2 of k-space collected in } -k_y \text{ direction)}$$

$$\gamma = 42.58MHz/T$$

$$G_x = 30.23mT/m$$

$$\delta_{dur} = 22.21ms$$

$$\Delta_{sep} = 38.42ms$$

Substituting these parameters into Equation 8, a negative rotation of $-13.0^\circ/s$ would shift the center of the echo to the most positive position of k-space that is acquired, leaving half of the signal unsampled. A positive rotation as slow as $6.5^\circ/s$ would cause the echo to shift to the most negative position acquired. These rates of rotations are easily achievable with intentional motion. (It should be noted that motion-induced signal void artifacts are not expected in the non-diffusion weighted images. For these $b=0$ images, spoiler gradients with $G_x = 22mT/m$, $\delta_{dur} = 2ms$, and $\Delta_{sep} = 6.2ms$ replace the diffusion sensitizing gradients. A rotational motion approximately 100 times faster would be required for the spoilers to cause signal void artifacts.) Examination of the k-space data for the diffusion weighted images should reflect the shift of the signal from the center if there were head rotation.

K-space data for images acquired during head rotation are presented in Figure 4. Images of axial slices 34, 35, and 36 from the volume shown in Figure 3 are presented to the left of a magnitude image of k-space. The k-space images show that the echo of the signal in slices 34 and 36 is translated away from the center of k-space whereas the center of the echo for slice 35 is properly centered in k-space. The magnitude images of k-space in Figure 4 also indicate that the MR signal was only acquired for part

of k-space. The data for the lowest quarter of k-space in the phase encoded direction (vertical in this presentation) are essentially zero because data were not collected in that region of k-space. When the center of k-space is shifted into a region of k-space not collected (as in Frame f of Figure 4), the reconstructed image intensity drops dramatically. The direction and distance of the signal from the center of k-space can be used to estimate the rate of rotation at the time of image acquisition.

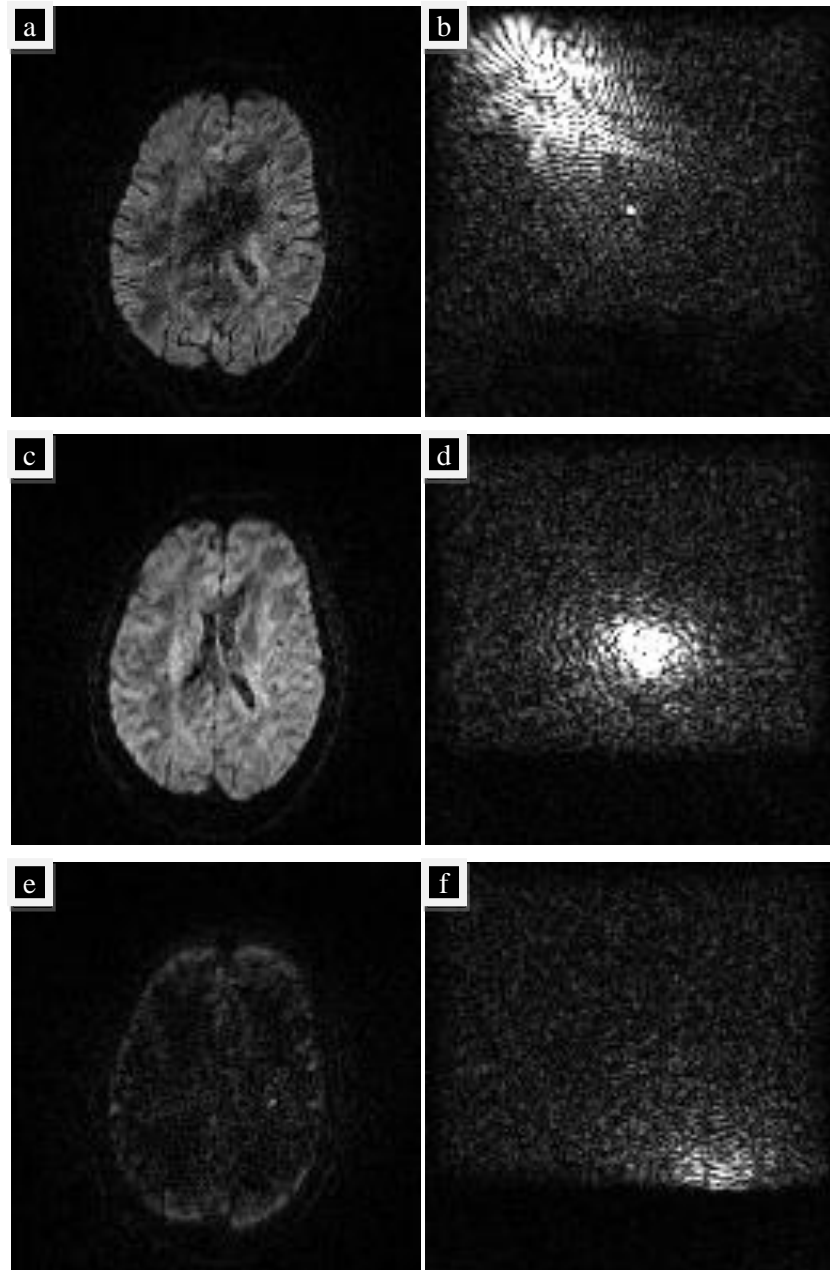


Figure 4. K-space shift of signal void artifacts: On the left are slices 34, 35, and 36 from Figure 3. On the right is the k-space data for each slice. The subject's head was still during slice 35, rotating to the left during slice 34 and rotating right during slice 36.

Although subject motion was not directly measured, subject motion can be inferred from co-registration of image data acquired at different times. Motion that occurred on the timescale of the volume acquisition can be estimated by analyzing the affine matrices used when registering the individual volumes to the first volume in the DTI scan. Evidence of motion between diffusion weighted volumes can be used as evidence that the subject was likely to have been moving while the slices within the volume were being acquired. Rotation and translation parameters of the affine matrices used to register volumes 42, 43, and 44 to the first volume of the DTI scan are presented in Table 1. In volume 43 the subject's head was rotationally repositioned about 1 degree about the y axis and translated about 1.4 mm in the posterior direction relative to the previously acquired volume. Subject motion during this time can be determined with more temporal precision by considering inter-slice motion as estimated by inter-slice co-registration.

Table 1. Rotation angles and translation distances for volumes near artifacts.

Volume	Ω_z (°)	Ω_x (°)	Ω_y (°)	I-S (mm)	R-L (mm)	A-P (mm)
Vol42	-0.42	-0.64	1.05	-0.22	-0.29	0.02
Vol43	-0.52	-0.21	0.12	0.16	-0.29	1.40
Vol44	-0.64	-0.39	0.87	-0.33	-0.11	0.10

The rotation angles about the z axis of the temporally sequential slices 32, 34, and 36 relative to slice 30 are presented in Table 2. The amount of axial rotation was determined by using the FLIRT algorithm of FSL to perform a 2D co-registration of the

slices. At the time volume 43 was acquired, the subject was directed to shake his head left and right. The direction of the diffusion weighting for this volume was $[x,y,z]=[0.78,0.53,0.33]$. This caused the center of k-space to move in the direction of -55° which is roughly the direction observed in Figure 4. Although the k-space image has experienced more distortion than simple translation, the center has moved about half of the distance to the corner which would be a k-space shift of about $0.5 \cdot \sqrt{2} \cdot 250 \text{ m}^{-1}$ or $\sim 177 \text{ m}^{-1}$. That amount of translation in k-space would occur with $\sim 7^\circ/\text{s}$ of axial rotation. The 64 slices of a volume were collected over 8.3 seconds. That means the sequential slices are acquired about one eighth of a second apart. The rotation between slice 30 and 32 would be roughly $15^\circ/\text{s}$ and between 32 and 34 would be roughly $4^\circ/\text{s}$. Since the instantaneous velocity at the time of diffusion weighting was not directly measured, this is the best estimate available to compare with the rotational velocity calculated from the shift in k-space. The comparison shows rough agreement between the estimate derived from registration and the estimate obtained using the shift in k-space. The rotation between slices 34 and 36 is in the opposite direction at about $19^\circ/\text{s}$. The signal for slice 36 was mostly rotated out of the region sampled which would be expected for that velocity of rotation. Subject rotation is a reasonable explanation for the changes observed in k-space.

Table 2. Rotation angles of temporally sequential slices for volume 43

Slice	Ω_z (°)
30	0.00
32	-1.89
34	-2.35
36	-0.02

The characteristics of the image artifact are also reasonably similar to the artifacts produced in simulation. The appearance of the artifact is similar in nature to the effect described by Wedeen for rotational bulk motion during MR imaging. Although there are similarities in appearance between Wedeen's simulation and the data from the volunteer, there are also distinct differences. The k-space data in Wedeen's simulation do not change shape, but are only translated. Also, the effect on the magnitude image was uniform except for the edge. Some slices from the volunteer had these characteristics but others deviated from these. In particular, Frame *b* of Figure 4 shows that the k-space data are more spread out than those of Frame *d*. Also, Frame *a* has a central portion of the image which is dark while much of it looks normal. The distortion of the signal profile in k-space is likely due to spatial variations in the degree of shift in k-space. That is, the k-space shift of signal from one voxel is different from that of another voxel. This could result from a change of the rotational head velocity during diffusion sensitization, though because that change would have to occur over the course of about 50 ms, it is more likely that the dispersion in k-space is due to non-rigid-body motion of the brain. As the head is rapidly accelerated, shear forces may cause additional velocity gradients in the brain. This would cause the k-space shift of signal from different parts of the brain to be

different. This explanation could also account for the observation that certain regions of a slice have signal void while other regions in the same slice look somewhat normal. Whereas the characteristics of the subject motion artifacts are modified by non-rigid body motion, non-rigid motion characteristics are more central to the formation of artifacts occurring with physiological noise and scanner vibrations.

1.4.2.2 Errors from physiologically induced artifacts

Non-rigid brain motion caused by cardiac pulsation and susceptibility changes caused by respiration are two sources of physiological noise in brain MRI. Feinberg characterized brain motion that is synchronous with cardiac systole (Feinberg and Mark 1987). Poncelet later used echo-planar MR velocity measurements to quantify the motion. He observed “a rapid displacement in systole with a slow diastolic recovery.” The brainstem moved at up to 2 mm/s caudally and the thalami moved medially at up to 1.5 mm/s. The maximum displacement was 0.5 mm (Poncelet, Wedeen et al. 1992). The impact of brain motion induced by cardiac pulsation on DTI was quantified by Habib (Habib, Auer et al. 2010). He described the large differences in diffusion weighted images acquired at different points in the cardiac cycle when the diffusion weighting was in the slice-select direction. Figure 5 presents axial slices acquired at various intervals after the R-wave in the subject’s cardiac cycle. Regions of artifact are noted by the arrows. Habib found that images acquired in about 6% of the whole cardiac cycle were subject to this artifact. Greitz found that brain motion induced by cardiac pulsation occurred during systole below the corpus callosum in the central and caudal parts of the brain (Greitz, Wirestam et al. 1992). However, Nunes, in studying the effects of cardiac gating on

diffusion weighted images, detected voxels superior to the corpus callosum which had signal variation that was greater when the images were not cardiac gated than when they were (Nunes, Jezard et al. 2005). The effects and efficiency of cardiac gating for DTI acquisition have been discussed by several investigators (Skare and Andersson 2001; Jiang, Golay et al. 2002; Nunes, Jezard et al. 2005; Habib, Auer et al. 2010).

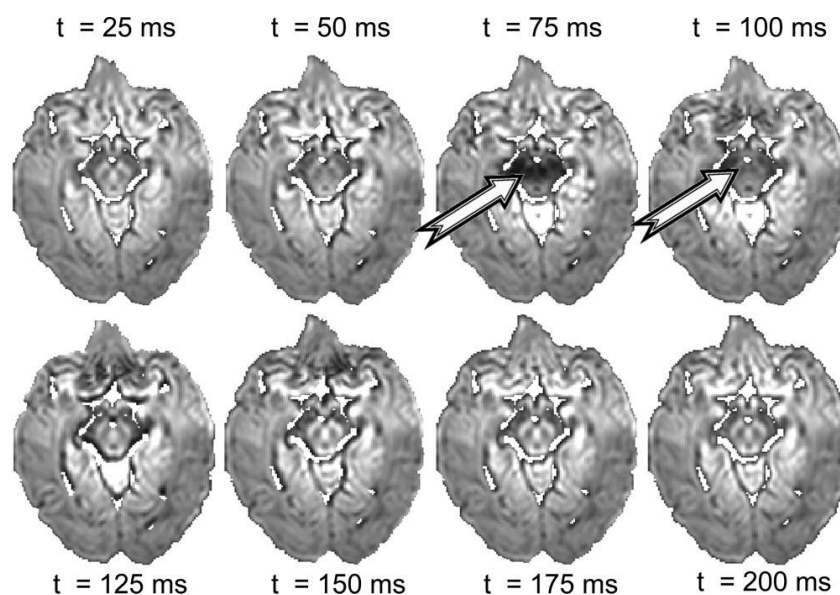


*Figure 5. Cardiac pulsation-induced signal void: Diffusion weighted images from a subject at specific interval t after the R-wave. Diffusion weighting was applied in slice-select direction. Arrows indicate signal void due to cardiac pulsation. Used, with permission, from: Habib, J., D. P. Auer, et al. (2010). "A quantitative analysis of the benefits of cardiac gating in practical diffusion tensor imaging of the brain." Magn Reson Med **63**(4): 1098-1103.*

The effect of respiration on diffusion weighted imaging has received less attention than cardiac pulsation has (Pierpaoli 2011). Noise introduced by respiration is commonly addressed in functional MRI studies. The respiratory effects are due partly to changes in the magnetic susceptibility of the chest cavity (Kruger and Glover 2001; Raj,

Anderson et al. 2001; Van de Moortele, Pfeuffer et al. 2002; Birn, Smith et al. 2008). Changes in the susceptibility of the lungs during respiration affect the magnetic field in the brain. The caudal parts of the brain, which are closer to the lungs, experience greater field change than the more rostral parts. Changes in the magnetic field cause an image shift in the phase encoding direction, an intensity shading in that direction, and diminished signal due to intra-voxel dephasing. Raj conducted an investigation of this effect at a field strength of 1.5 T. He found the image shift to be on the order of a pixel or less which was 3.12 mm in his investigation, while the intensity variation was on the order of 1% (Raj, Anderson et al. 2001). The model which Raj had developed earlier predicts that these effects scale with field strength (Raj, Paley et al. 2000), so at 3 T the image shift should approach 6 mm and the intensity variation should be about 2%. Birn derived a respiration response function from the effects of a single breath hold and showed an effect with a latency of 16 seconds (Birn, Smith et al. 2008). This demonstrates an effect which is distinct from the effect caused by changes in the magnetic susceptibility of the lungs. It is hypothesized that changes in breathing affects the blood gases which in turn affects the oxygenation and flow of blood in the brain. These changes influence the magnetic susceptibility of the tissue on a microscopic level which in turn can cause local dephasing and signal loss. The degree of importance of respiratory artifacts has not been investigated for DTI. However, the intra-voxel dephasing could interact with the dephasing caused by bulk rotational motion or cardiac motion to cause enough intra-voxel phase variation to result in signal void.

1.4.2.3 Errors from vibration artifacts

Dr. Kaundinya Gopinath and Dr. Sergey Cheshkov conducted tests for a DTI study at UT Southwestern Medical Center which revealed a vibration artifact in the medial parietal lobes caused by a mechanical coupling of scanner vibration to the brain. The artifact consisted of regions of signal void when the diffusion encoding gradient direction was primarily in the left-right direction, which for their tests was the x direction. The signal void was interpreted in the tensor calculation as increased diffusivity in the x direction. The tests were conducted using the TRSE sequence on a Siemens 3T TIM Trio scanner. The artifact was shown to be due to vibration by demonstrating that mechanical damping reduced the effect significantly. Gallichan characterized this signal void artifact and proposed a post-processing correction for it (Gallichan, Scholz et al. 2010). He noted that the artifact occurred with partial-Fourier acquisition but not when the whole k-space was acquired. Figure 6 illustrates the vibration-induced signal void. Gallichan concluded that mechanical shear-waves propagating through the brain produced velocity gradients within the brain.

Mechanical shear-waves produce signal void in diffusion weighting images by creating velocity gradients in the imaged object. Motion in the direction of the diffusion sensitization produces an additional phase component to the signal as indicated by Equation 6. An in-plane gradient of the velocity will produce a phase ramp which shifts the signal in k-space. When the phase ramp shifts the signal out of the region of k-space being acquired, the signal for the affected voxel is lost. For partial k-space reconstruction, the shortest distance from the center of k-space to a region of k-space not collected is in the negative phase encoding direction. This makes the system most sensitive to velocity

gradients in that direction. Because water is nearly incompressible, a velocity gradient in the direction of a vibration would be nearly zero. On the other hand, laminar flow would allow a velocity gradient perpendicular to the direction of the vibration. Therefore, velocity gradients in the phase encoded direction occur only when the direction of vibration lies in the x - z plane. This helps to account for why diffusion weighting in the x direction is more prone to vibration artifacts than weighting in the y direction. The propensity for the x direction being more sensitive than the z direction is apparently due to scanner vibration considerations. Gallichan noted that the physical sensation of vibration was mildly stronger when the diffusion gradients were applied along the x direction as compared to the y or z direction. Another factor which affects the amplitude of the vibration is the choice of diffusion weighting sequences.

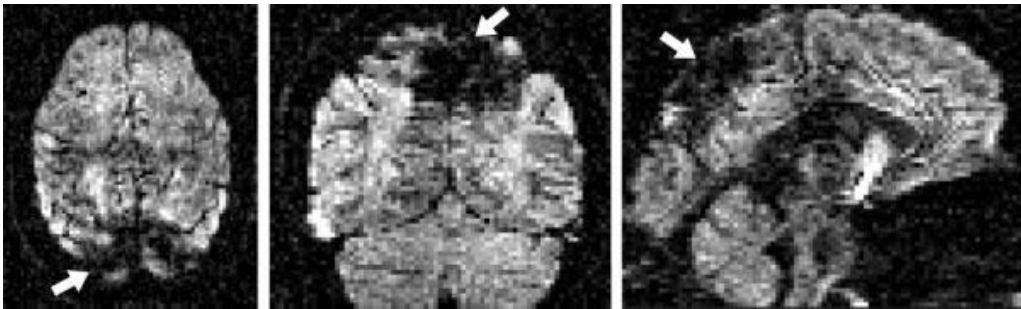


*Figure 6. Vibration-induced signal void: Axial, coronal, and sagittal cross-sections of a diffusion-weighted volume demonstrating a severe example of the vibration-induced artifact located mainly in the medial parietal lobe. Diffusion-gradient direction was $[x, y, z] = [0.98, 0.02, -0.20]$. Used, with permission, from: Gallichan, D., J. Scholz, et al. (2010). "Addressing a systematic vibration artifact in diffusion-weighted MRI." Hum Brain Mapp **31**(2): 193-202.*

The TRSE sequence was designed to reduce eddy current distortion in diffusion weighted images (Reese, Heid et al. 2003). The sequence uses a second

refocusing rf pulse to provide more flexibility in diffusion gradient design. With this sequence, the diffusion gradients are rapidly turned on and off four times rather than twice. The additional switching, however, results in greater scanner vibration. Hiltunen compared the scanner vibration during DTI using the TRSE sequence to the vibration when using the Stejskal Tanner sequence. He found that the TRSE sequence increased the amplitude of scanner vibrations by a factor ≥ 1.5 over vibration with the Stejskal Tanner sequence (Hiltunen, Hari et al. 2006). When the TRSE sequence was replaced with the Stejskal Tanner sequence on the Siemens scanner used by Gopinath and Cheshkov, the vibration artifacts were largely, though not completely, mitigated. The artifact remained a concern, because when it did occur, just as with the motion-induced signal void, the impact on the tensor calculation was dramatic.

The localization of the artifact using this method in a set of 22 images is visually presented in Figure 7.

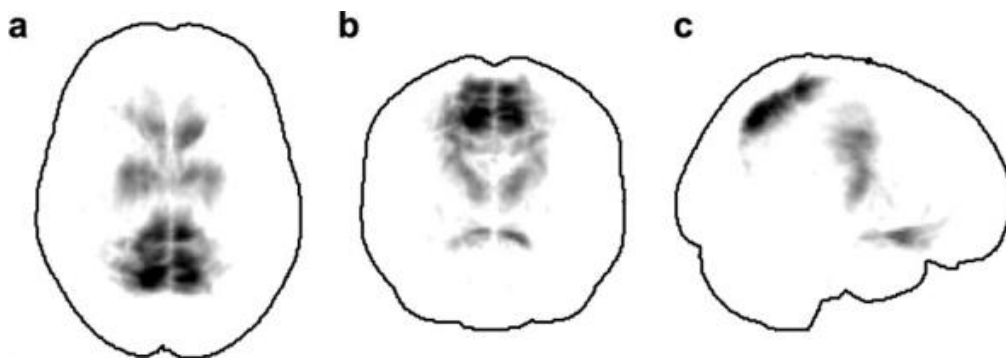


Figure 7. Location of vibration artifacts: Maximum-intensity projections of the mean distribution of the artifact co-regressor across 22 subjects which Gallichan used to mitigate the effect of the vibration-induced signal void artifact. (a) axial, (b) coronal, and (c) sagittal views. Used, with permission, from: Gallichan, D., J. Scholz, et al. (2010). "Addressing a systematic vibration artifact in diffusion-weighted MRI." Hum Brain Mapp 31(2): 193-202.

1.4.2.4 Impact of signal void artifacts on FA

Sharman investigated the impact of data corruption for DTI and concluded that even minor corruption has the potential to affect the tensor direction. He also noted that the impact on FA increased as the severity of the corruption increased. In several cases he observed an FA change of about 35% of the original FA (Sharman, Cohen-Adad et al. 2011). Use of a more robust data fitting algorithm may provide a valid tensor fit in spite of the presence of artifacts.

1.4.2.5 Robust algorithms for fitting the data to the tensor model

Fitting diffusion weighted data to the tensor model requires that the error between the model and the data be quantified and minimized. Three sources of error that impact the tensor calculation are noise, artifacts, and tissue diffusivity that is not correctly modeled by a tensor. When the primary source of error is scanner noise, the linear least-squares method described above provides a robust estimate of the best tensor fit to the data. If any particular data point were excluded from the tensor calculation, the result would not be greatly affected. However, since artifacts do affect the tensor calculations, and they are a source of known error, it is desirable to remove their influence from the tensor fitting process.

Chang discusses the need for limiting the effect of data outliers, such as artifacts, on the calculation of DTI tensors. He points out that the linear least-squares method is not robust in the presence of “physiological noise” and that it is sensitive to the presence of outliers. He outlines three common tensor fitting methods which are presented in Table 3 (Chang, Jones et al. 2005). In the table, $S_{(0)}$ is the signal intensity

when no diffusion sensitizing gradients are applied. $S_{(\mathbf{b})}$ is the signal intensity when the diffusion sensitizing matrix \mathbf{b} is applied. \mathbf{D} is the diffusion tensor, σ is the standard deviation of the signal, r_i is the residual from a prior estimation and C is a scale factor. The methods summarized in Table 3 minimize the value of χ^2 as calculated by the equation $\chi^2 = \sum_i \omega_i \times (y_i - y(x_i))^2$, where $y(x_i)$ is the modeled signal for the i^{th} \mathbf{b} vector and y_i is the measured signal. The natural logarithm of the signal intensity is used for the linear method and the raw signal intensity is used for the other two methods. The nonlinear least-squares method as implemented by Markwardt (Markwardt) and the Geman-McClure M-estimator method as implemented by Mangin (Mangin, Poupon et al. 2002) provide more robust tensor calculations than the linear least-squares method, but each is still influenced to some degree by outlier data points. These outliers must be removed from the calculation if their influence on the tensor is to be completely eliminated.

Table 3. Regression Methods Used in Diffusion Tensor Estimation

Method	Equation	Weighting function
Linear least-squares	$\ln S_{(\mathbf{b})} = \ln S_{(0)} - \mathbf{bD}$	$\omega_i = \frac{(S_{(\mathbf{b})})^2}{\sigma^2}$
Nonlinear least-squares	$S_{(\mathbf{b})} = S_{(0)} * \exp(-\mathbf{bD})$	$\omega_i = \frac{1}{\sigma^2}$
Geman-McClure M-estimator	$S_{(\mathbf{b})} = S_{(0)} * \exp(-\mathbf{bD})$	$\omega_i = \frac{1}{r_i^2 + C^2}$

Used, with permission, from: Chang, L. C., D. K. Jones, et al. (2005). "RESTORE: robust estimation of tensors by outlier rejection." Magn Reson Med 53(5): 1088-1095.

Chang proposed a method for identifying outliers and removing them from the tensor calculation and implemented it in his RESTORE algorithm (Chang, Jones et al. 2005). The RESTORE algorithm begins by estimating a tensor with all the data using the nonlinear least-squares method. If all the residuals are less than three times the standard deviation of the background noise, the tensor solution is accepted. If any residuals fall outside of this criterion, each data point is re-weighted by a formula which depends on the fit to the tensor and a new tensor is calculated. The re-weighting is done iteratively until a convergence criterion is met. Outliers to the tensor model are then identified and removed and a final tensor is calculated. The flow chart in Figure 8 depicts the process graphically. The RESTORE algorithm robustly fits DTI data to a tensor, but the data being evaluated for outlier status may have been smoothed during volume co-registration, leading to errors in identifying outliers.

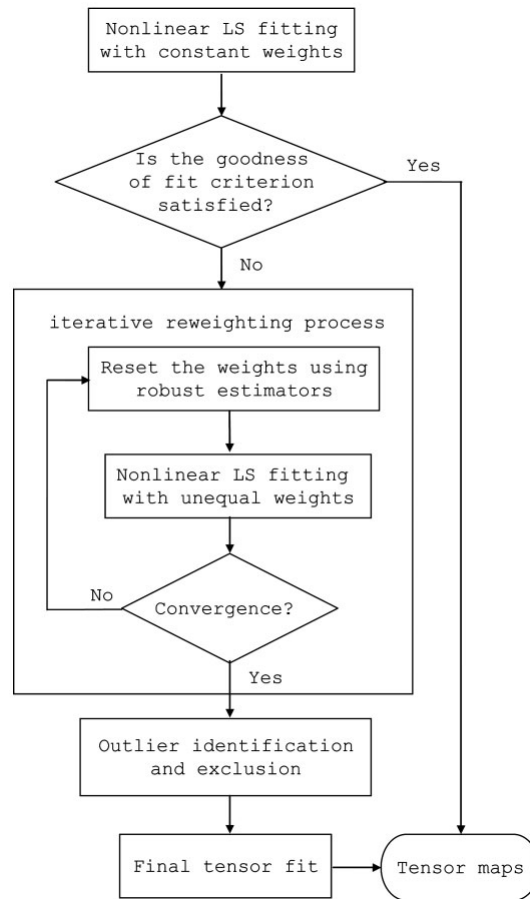


Figure 8. Flow diagram of RESTORE algorithm: Used, with permission, from: Chang, L. C., D. K. Jones, et al. (2005). "RESTORE: robust estimation of tensors by outlier rejection." *Magn Reson Med* 53(5): 1088-1095.

Co-registration of DTI data to a common template before tensor fitting causes the interpolated data points used for tensor fitting to have contributions from both valid data and artifacts. This results in the likelihood that some interpolated data points that are corrupted by artifacts will not be flagged as outliers. Morris proposed an approach that would allow data to be analyzed for outlier exclusion before they were registered to the common template (Morris, Nossin-Manor et al. 2011). His approach is to analyze each

diffusion weighted volume by selecting it as the target template for co-registration and then using the RESTORE algorithm to identify its outliers. As the target template, the volume is not interpolated so there is no mixing of valid data and artifact in that volume. Data identified as outliers are then replaced by estimates generated from tensors calculated by the RESTORE algorithm. Outliers are identified and replaced in each diffusion weighted volume through this process. This process improves the outlier identification, but the solution that Morris proposed has the potential of introducing bias by substituting data simulated from a model and then fitting that same model with a combination of valid data and simulated data.

When data that do not conform to the tensor model fall outside the acceptance criteria, the RESTORE algorithm excludes the data as outliers. In many cases the data are outliers due to artifacts or random noise. In other cases, the data may not fit the model because the tensor is not a good model for the actual diffusivity of the tissue. This is true for inhomogeneous voxels partially filled with fibers of one orientation and partially filled with other tissue or with fibers of a different orientation. In such a case, it would be inappropriate to exclude data as outliers because the RESTORE algorithm would generate a tensor fit which on the one hand is closer to the remaining data, but on the other hand is biased by the fact that valid data, which may significantly influence the tensor fit, are excluded (Zhou, Liu et al. 2011).

The presence of artifacts in DTI data can have a dramatic impact on the tensors that are calculated. Robust algorithms such as non-linear or iterative methods reduce the effect of outliers but they do not completely remove it. The RESTORE algorithm removes artifacts so they do not contribute to the tensor calculation, but by removing all

outliers, the RESTORE algorithm potentially biases the results by removing valid data, especially for voxels with volume averaging or fiber crossings. Rather than relying on the robustness of the tensor solving algorithm to reduce sensitivity to error, removal of known error before solving the tensor is more appropriate. As DTI experiments typically acquire more than the minimum number of six diffusion directions needed to calculate the tensors, this redundancy in the data can be exploited by simply eliminating the corrupted data from the calculation of the tensors. An approach of visually inspecting and removing volumes with signal void artifacts is commonly used. However, by removing the whole volume, valid data from the unaffected slices is unnecessarily lost (Sharman, Cohen-Adad et al. 2011; Zhou, Liu et al. 2011). In addition, visual inspection is prone to overlook some slices with corrupted data (Zhou, Liu et al. 2011). Furthermore, for subjects with excessive motion, slices from a large number of volumes may be affected. If all slices from all affected volumes are excluded, there may not be enough data left to make a valid tensor fit, thus excluding the subject from a study (Morris, Nossin-Manor et al. 2011). Zhou approached these problems by automatically detecting artifacts and then only removing the affected slices rather than the whole volume (Zhou, Liu et al. 2011). Sharman addressed the problem of potentially removing too many volumes by interpolating from uncorrupted data if fewer than 16 volumes remained (Sharman, Cohen-Adad et al. 2011). As discussed above, Morris identified outliers using the RESTORE algorithm and then replaced the corrupted data with an estimate calculated from the tensors fit with data that the RESTORE algorithm accepted as valid. Properly handling artifacts in DTI data requires more innovation to provide a robust solution that does not bias the results. Robust and unbiased results are needed to minimize variation so

that valid group comparisons can be made.

1.4.3 Measuring significance of group differences using DTI results

DTI is commonly used to detect subtle differences between groups. Several approaches are available which differ in complexity, interpretability and sensitivity. A common approach used for exploiting the data in DTI scans is to utilize the directional and spatial information available in the data to generate tractograms, which are maps of white matter tracts. Points within a volume of tensors can be connected by following the local tensor direction from one point to the next. Using this approach, putative white matter tracts can be traced from seed regions of interest throughout the brain. Tractography algorithms fall into two main categories, deterministic and probabilistic. Deterministic algorithms start at a seed point and trace a tract until defined end criteria are met. At each point along the tract, only one direction can be followed to the next point (Mori, Crain et al. 1999). Probabilistic algorithms allow for multiple directions to be followed at any given point. Which direction is followed is determined by chance and probability. Many iterations are followed and a record is compiled of the voxels traversed. The probability that a voxel is connected to the seed is assumed to be related to how many sampled tracts pass through it (Behrens, Woolrich et al. 2003). Quantitative group analysis of the resulting tracts, whether computed deterministically or probabilistically is challenging. Careful intersubject registration is required and proper statistical comparisons must be made.

One approach to making group comparisons is to compute rotationally invariant scalar quantities from the diffusion tensors, co-register the images from all

subjects in a study, and then make a statistical comparison of the group averages at each voxel. Voxel Based Morphometry (VBM) has proven very useful in structural analysis. However, precise co-registration between subjects is crucial for making correct inferences. Voxel based comparisons of tensor quantities has not proven useful for analyzing the DTI scans of several subjects. This is due to the difficulty in precisely co-registering FA maps from different subjects (Smith, Jenkinson et al. 2006). The FSL tract-based spatial statistics algorithm (TBSS) is designed to provide sufficient white matter tract registration for group analysis (Smith, Jenkinson et al. 2006). Working under the assumption that the center of white matter tracts will have the greatest anisotropy, the averaged image of the non-linearly registered FA maps in a study is thinned and skeletonised. The skeleton is assumed to lie at the center of white matter tracts. The individual FA maps are further registered to the skeletonised average FA by finding the local maximum on the perpendicular to the skeleton and generating an FA skeleton for each DTI scan. Each point on the skeleton has FA values from every DTI scan in the analysis. Statistical inferences are then made on the samples of the same location. The FSL tool for making statistical inferences on TBSS data is called “RANDOMISE”. It uses a Monte Carlo algorithm to build a distribution of averages by randomly assigning the study subjects to each of the groups being compared. The average calculated from the actual assignments of groups is statistically compared to the distribution of the averages calculated from the random assignments of groups (Nichols and Holmes 2002). Very subtle differences between groups can be detected that cannot be visualized in individual subjects. However, if the differences between groups are localized to structures smaller than the resolution provided by the diffusion weighted images, the differences may not be

detectable.

1.4.4 Increasing image resolution

A challenge for DTI imaging of small structures in the brain is to acquire images with sufficient spatial and angular resolution to answer questions about those structures in a period of time that is short enough to make the scan practical for a human subject. Many structures in the brain, particularly structures in the brainstem, are difficult to image with DTI because of their small size and complexity. An example of this is the locus ceruleus which is a cluster of neurons in the brainstem that play a major role in arousal, attention and stress response (Benarroch 2009). When deficiencies in these areas are part of a particular disorder, it would be helpful for studying that disorder to establish whether there are differences in the locus ceruleus of the patient population compared to a control group.

An example of a disorder with symptoms of deficiencies in arousal, attention and stress response is the Gulf War Illness (Iannacchione, Dever et al. 2011). The Gulf War Illness describes a pattern of symptoms experienced by many veterans of the 1991 Persian Gulf War. Haley characterized three strongly clustered syndromes using factor analysis of symptoms (Haley, Kurt et al. 1997). Syndrome 1 (“impaired-cognition”) was “characterized by problems with attention, memory, and reasoning, as well as insomnia, depression, daytime sleepiness, and headaches.” Syndrome 2 (“confusion-ataxia”) was “characterized by problems with thinking, disorientation, balance disturbances, vertigo, and impotence.” And syndrome 3 (“arthro-myo-neuropathy”) was “characterized by joint and muscle pains, muscle fatigue, difficulty lifting, and extremity paresthesias.” Since

arousal and attention are symptoms which are part of syndrome 1 but not included in syndrome 2 or 3, the locus ceruleus may be involved in the illness. Researchers investigating the Gulf War Illness acquired DTI data at a resolution of $1.25 \times 1.25 \times 3 \text{ mm}^3$ in an effort to image small features of the brainstem such as the locus ceruleus. Figure 9 depicts the size and location in the brain of the locus ceruleus (Benarroch 2009). The mean size of the locus ceruleus in healthy adults is 12.7 mm in length with a volume of 10.5 mm^3 (Hoogendijk, Pool et al. 1995).

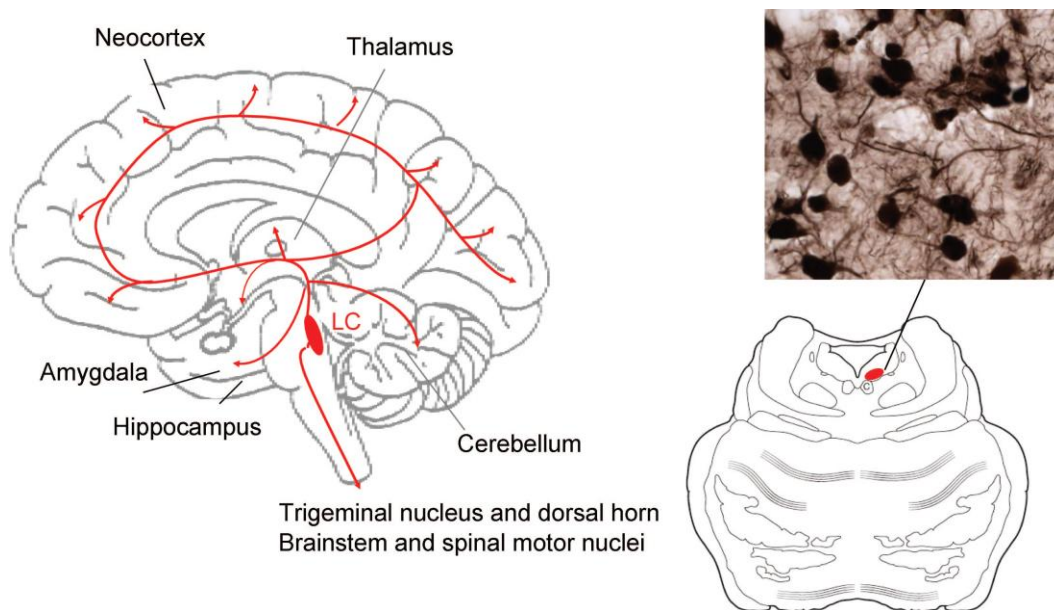


Figure 9. The locus ceruleus (LC) in the brainstem: Used, with permission, from: Benarroch, E. E. (2009). "The locus ceruleus norepinephrine system: functional organization and potential clinical significance." *Neurology* 73(20): 1699-1704. As modified from Benarroch EE. *Basic Neurosciences with Clinical Applications*. Philadelphia: Butterworth Heinemann/Elsevier; 2006 (figure 23-10). Copyright Elsevier 2006.

To reliably distinguish two structures in an image, the resolution of the image

must be smaller than the structures themselves (Liang and Lauterbur 2000). For the locus ceruleus, the cross-sectional resolution would need to be on the order of 1 mm or smaller. Isotropic resolutions of 1.8 mm have been achieved using EPI with partial k-space reconstruction and parallel imaging hardware (Nagae-Poetscher, Jiang et al. 2004). However, this resolution is insufficient to image structures of 1 mm. One approach to increasing resolution is to allow for 3D multi-shot acquisition. Unfortunately, the requirement of cardiac gating substantially increases the scan time and motion sensitivity of the sequence makes this approach impractical for DTI when using many scan directions (Golay, Jiang et al. 2002). Another approach uses additional post-processing to gain local resolution from continuity of fiber tracts throughout the brain (Calamante, Tournier et al. 2011). However, efforts made here were not successful in reproducing similar resolution increases on available data. Other investigators have increased the attainable resolution by decreasing the FOV by either only exciting nuclei within the FOV (Jeong, Kim et al. 2005) or by suppressing the outer volume before exciting the FOV (Karampinos, Van et al. 2008). Each of these techniques attempts to separate image information from noise and artifacts inherent in MRI.

The major limiting factor for MRI spatial resolution is noise. When rf excitation at the Larmor frequency is introduced to a system of nuclei, the nuclei precess synchronously and the coherent magnetic signal can be detected. However, slight variations in magnetic field experienced by the nuclei cause them to resonate at slightly different frequencies. With time, the coherence of the nuclei degenerates and the signal decays with a time constant called T_2^* . Many factors contribute to the initial strength of the signal and many factors contribute to the noise in the detected signal. As long as the

detected signal is above the noise level, information about the system can be detected. For a single-shot acquisition method, the number of samples in k-space available for image reconstruction is limited to the number of signal samples that can be acquired by the scanner before the signal decays to the noise level. Furthermore, the number of samples acquired per second is limited by the scanner hardware bandwidth. The signal and noise collected in k-space will produce a mixture of signal and noise in the reconstructed image that is characterized by the signal to noise ratio (SNR). For a given sequence, SNR is determined by signal strength and noise levels inherent to the scanner and sequence as well as by reconstruction parameters such as voxel volume and number of measurements of the signal. A generalized expression for SNR for MRI is (Elster and Burdette 2001):

$$SNR = K \cdot v \cdot \frac{\sqrt{\# \text{ measurements}}}{\sqrt{\text{bandwidth}}} \quad (9)$$

where: K accounts for system and sequence characteristics, and

v is the voxel volume.

For single-shot EPI, the number of measurements is generally set to the maximum possible. Therefore the SNR cannot be improved by increasing the number of measurements per image, but multiple images can be averaged to increase the SNR. For the case of DTI, when the number of images acquired is increased a choice is available as to whether additional diffusion weighting directions are added or whether current diffusion weighting directions are replicated.

1.4.4.1 Directional resolution

The SNR of a DTI scan can be increased by increasing the number of volumes

acquired during the scan. The SNR in the diffusion tensors is impacted by the number of diffusion weighted directions and the number of b values used in the DTI scan. Jones found that measurements of ADC and trace have the best noise characteristic when two b values are used, the low b value as low as possible and the high b value being greater by 0.85/tissue diffusivity. Jones also calculated that the number of measurements made at the high b value should be 8.7 times the number made at the low b value with only one volume for each direction (Jones, Horsfield et al. 1999). For calculation of mean diffusivity (MD), fractional anisotropy (FA) and tensor orientation, a minimum of 30 independent directions for the high b value are required for a robust determination of these quantities (Jones 2004). Removing volumes from a DTI scan before fitting the tensor reduces the SNR of the anisotropy indices computed from the tensors. Zhan found that for a group of 50 subjects, adding a single diffusion direction to a DTI scan significantly increased the SNR of FA up until 53 independent directions were included in the scan (Zhan, Leow et al. 2010). He concluded that additional increases of SNR were available up to about 60 independent directions. An implication of Zhan's study is that loss of data through occasional signal void artifacts does not have a significant impact on the SNR of the anisotropy indices so long as the erroneous data are not used in computing the tensor and as long as the number of independent diffusion weighted directions does not fall below 53. When the more complex diffusivity model of two superimposed tensors is used to account for crossing fibers, b values two to three times greater give better results (Alexander and Barker 2005). Although SNR can be improved by increasing the number of volumes acquired, poor SNR of the individual volumes cannot be ignored because of biases introduced by the rectified noise floor of low SNR images.

1.4.4.2 Bias errors due to noise

The bias introduced in low SNR MRI is a well established phenomenon (Henkelman 1985; McGibney and Smith 1993; Gudbjartsson and Patz 1995; Dietrich, Heiland et al. 2001; Jones and Basser 2004). Noisy MRI data form a Rician distribution (Gudbjartsson and Patz 1995). For signals well above the noise floor, the noise is essentially Gaussian with no bias. However, for signals near the noise floor, the noise has a skewed distribution with a definite bias. This bias is introduced because Gaussian noise in the real and imaginary images produced by the discrete Fourier transform is rectified when the magnitude of the complex image is computed. Many correction schemes have been proposed to remove the bias, all of which require a good estimate of the background noise (Dietrich, Heiland et al. 2001). Although several techniques are available for measuring the SNR of an MR image, care must be exercised in selecting the proper technique. In particular, results from comparing the average signal from a region of interest with the noise measured in the background has been shown to differ from the real SNR in many cases (Dietrich, Raya et al. 2007). This is particularly true when parallel imaging techniques are used for image reconstruction since the SNR of the reconstructed image is not position independent. When DTI data are collected with low SNR, the bias introduced by noise has a significant impact on the calculation of the ADC and consequently on the calculation of the diffusion tensors. Jones explored this issue and proposed a limit to the b value that could be used without needing to adjust for the bias introduced by the noise floor (Jones and Basser 2004). As the resolution of DTI is increased, the individual volume SNR must be monitored to determine if appropriate bias corrections are required. Another consequence of increasing the resolution DTI scans

collected with single-shot EPI is that decreasing the voxel size while keeping the number of samples constant reduces the FOV which could then introduce aliasing.

1.4.4.3 Cause of aliased signal

When the MR image is reconstructed from k-space using a Discrete Fourier Transform, the FOV is determined by the sample spacing in k-space, and the resolution of the image is determined by the number of samples N in k-space. For a 2D image $FOV_x = 1/\Delta k_x$; $FOV_y = 1/\Delta k_y$; $\Delta x = FOV_x/N_x$; $\Delta y = FOV_y/N_y$. If the k-space samples are acquired on a rectangular grid, and the number of samples across the grid is constant, then increasing the image resolution (decreasing Δx and Δy) will result in decreasing the FOV. If the FOV is decreased too far, then tissue will fall outside the FOV. Signal from the tissue that is outside the FOV will still be collected by the receiver, but its location will be misinterpreted (or aliased) during image reconstruction as having come from inside the FOV. If the aliased signal is superimposed on a region of interest such as a brain structure, the true and corrupting signals cannot be separated which makes it impossible to calculate an accurate diffusion tensor for the structure.

When the Fourier Transform of a continuous one dimensional function $I(x)$ is sampled with a regular sample spacing Δk , the Discrete Fourier series reconstruction $\hat{I}(x)$ follows the relationship (Liang and Lauterbur 2000):

$$\hat{I}(x) = \sum_{n=-\infty}^{\infty} I(x - \frac{n}{\Delta k})$$

$\hat{I}(x)$ is a periodic function with period $1/\Delta k$. For two dimensional images this periodic property holds true for both dimensions. In practice, only a single period of the reconstructed signal is used. However, if the original signal is not contained within a

range of $1/\Delta k$, the signal from outside that range will be wrapped around and superimposed onto the signal within the range. Figure 10 shows an image reconstructed from k-space using a discrete Fourier transform. The original object is replicated with a period determined by the k-space sampling resolution. A single period of the image is depicted by the green box. When all the signal of the original object can be contained in one period of the reconstructed image, the replicated images can be ignored. If the k-space sample spacing were increased, the size of a single period would be reduced as depicted by the red box. Because the original object cannot be contained within one period, the replicated reconstruction will overlap as on the right of Figure 10. The light blue mask indicates the high intensity portions of the replicated images. The signal from the replicated images is “aliased” into the central period, making it impossible to separate the desired signal from the replicated signal.

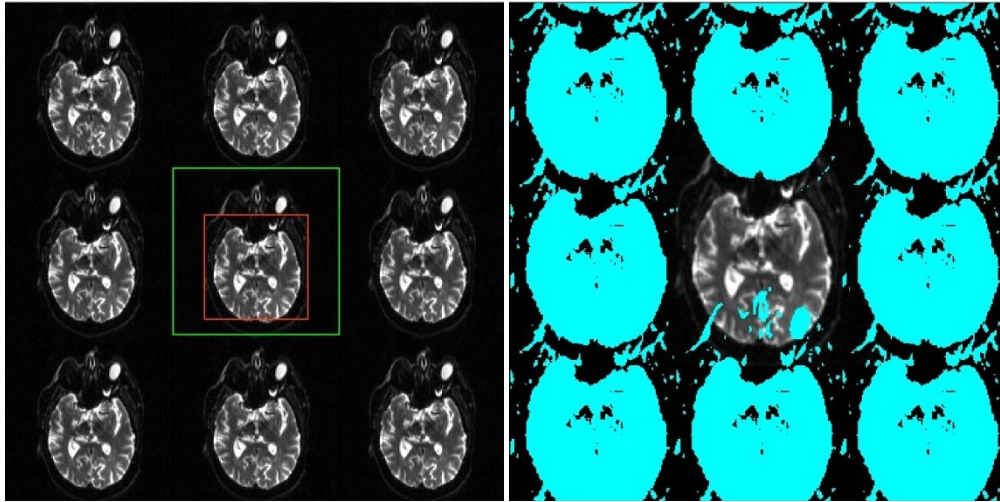


Figure 10. Simulated aliasing of a small-FOV image: The image on the left was acquired with a k -space sampling fine enough to avoid overlap between periods of the DFT reconstruction. The image on the right is a simulation of a course k -space sampling that would cause data aliasing. A threshold was applied to the “aliased” data which are depicted by the blue mask. The green box indicates the FOV of the original acquisition. The red box indicates the FOV simulated on the right.

Once aliased signal is superimposed on the desired signal, the two cannot be separated. However, signal that has not been contaminated is still a proper reconstruction of the original. As long as the dimensions of the original object are not greater than twice the dimensions of the FOV used during image acquisition, there will be some portion of the original signal which is faithfully reconstructed. Figure 11 displays an example of an image which was corrupted by aliased signal during image acquisition. Of particular note is the mislocation of the occipital lobe to the anterior of the image.

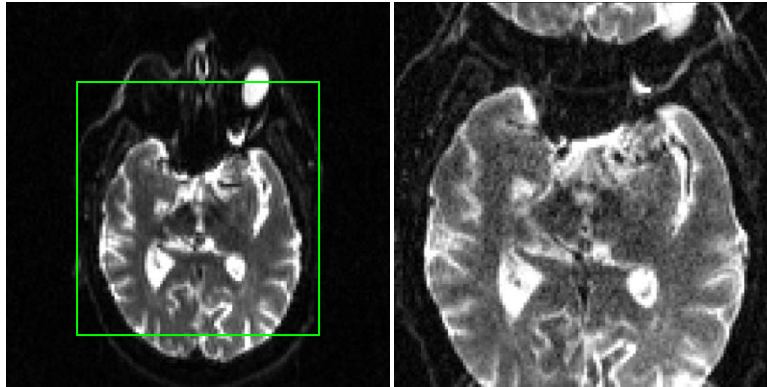


Figure 11. Aliasing of a small-FOV image: The image on the left has an in-plane resolution of $2 \times 2 \text{ mm}^2$ with an FOV of $256 \times 256 \text{ mm}^2$. The green box depicts the smaller field of view used for the image on the right which has an in-plane resolution of $1.25 \times 1.25 \text{ mm}^2$ with an FOV of $160 \times 160 \text{ mm}^2$.

1.4.4.4 Impact of aliased signal on image processing

Aliased signal in a 3D volume can be problematic when it is unclear whether the data being analyzed is corrupted with aliased signal. Although automatic skull stripping tools such as the Brain Extraction Tool (BET) (Smith 2002) in the FSL library do a good job of creating a brain mask for images with reduced FOV, there are no tools for identifying and excluding regions within the brain which have aliased signal superimposed on properly interpreted signal. DTI volumes with significant aliased signal must be handled in a way that keeps the aliased signal from being included in image analysis. Since aliased signal in a digital image cannot be distinguished from correctly interpreted signal, additional innovation is required to properly handle high resolution DTI data which have significant amounts of aliased signal.

CHAPTER TWO

AIMS

High resolution DTI provides image contrast that reflects tissue microstructure and larger scale organization of tissue, particularly of white matter tracts in the brain. DTI has proven to be a useful tool for analyzing the structure and health of white matter brain tissue. Many advances have been made to overcome image distortion issues, poor tensor fitting in the presence of artifacts, difficulty in measuring significance of observed differences and increasing resolution for imaging the brainstem. Each of these areas deserves more effort. The aim of this research is to address two of these: poor tensor fitting in the presence of artifacts and increasing resolution for imaging the brainstem. Properly handling artifacts in DTI data requires more innovation to provide a robust solution that does not bias the results. Since aliased signal in a digital image cannot be distinguished from correctly interpreted signal, additional innovation is required to properly handle high resolution DTI data which have significant amounts of aliased signal.

2.1 Specific Aims for This Study

The aims of this study are;

- 1) to develop an approach for mitigating the influence that signal void artifacts have on DTI analysis,
- 2) to develop an approach for mitigating the impact on data analysis arising from the

presence of aliased signal which occurs in DTI scans which have an axial FOV smaller than the head,

3) to apply tract-based spatial statistics (TBSS) (Smith, Jenkinson et al. 2006) for group analysis on the DTI data collected for the Gulf War Illness study (GWIS) after applying the signal void artifact removal method and the aliased signal impact mitigation method developed here.

2.2 General Approach to Accomplish Aims

To accomplish the first aim, a method was developed for automatically flagging slices within volumes of a DTI scan which have signal void artifacts, and a method was developed for excluding slices flagged as having signal void artifacts from the diffusion tensor calculation. The method for flagging artifacts is generally applicable to DTI data. Excluding the effect of individual slices on the tensor is presented here as a way to exclude known error while including as much uncorrupted data as possible in the tensor fitting process. Simulated DTI data were used to demonstrate the influence of artifacts on FA and to demonstrate the impact on FA of excluding signal void artifacts. DTI scans collected for the Gulf War Illness study conducted at UT Southwestern Medical Center were used as a test bed to demonstrate the application and utility of these methods to real data.

To accomplish the second aim, a method was developed for masking regions of small-FOV DTI scans which are contaminated with aliased signal. The method utilizes information from a structural MRI image acquired with an FOV large enough to cover the whole brain. The structural image used for this method had similar image contrast and

geometric distortions as the DTI non-diffusion weighted images. The method of generating the aliased signal mask only requires use of FSL tools and information in the image header about the scanner position of the image origin. This approach is presented as a way to utilize higher in-plane resolution DTI of the brainstem which contains aliased signal in contrast to the standard approaches that rely upon suppressing signal outside of the FOV during image acquisition (Golay, Jiang et al. 2002; Jeong, Kim et al. 2005; Karampinos, Van et al. 2008).

To accomplish the third aim, the DTI data collected for the Gulf War Illness study at UT Southwestern Medical Center were processed using standard processing augmented by signal void artifact removal and aliased signal masking. Group analysis was performed between syndrome groups present in the subjects of the GWIS and the control group using the TBSS algorithm of FSL. Group analysis was performed using both the whole head field of view DTI data and the small field of view DTI data. This analysis demonstrated that the artifact removal method could be applied to real data and demonstrated whether applying the method produced an impact on the TBSS analysis of the GWIS DTI data. The analysis using the small field of view DTI data further demonstrated whether enough data were left after masking out the aliased signal to allow for analysis of the scans using the TBSS algorithm.

The results of this study are generally applicable to DTI data collected with an axial field of view smaller than the area of signal producing tissue but not so small that aliased signal is superimposed on the region of interest. The handling of signal void artifacts is more broadly applicable to DTI collected with a standard field of view as well. Furthermore, it is expected that the technique of generating a brain mask from an image

with a larger field of view could be extended to other modalities which have restrictions placed on resolution by aliased signal.

CHAPTER THREE

METHODS

3.1 Simulation of Diffusion Weighted Images with Signal Void Artifacts

Diffusion weighted images were simulated using the diffusion tensors calculated for the DTI scan of one subject of the Gulf War Illness study. The imaging parameters used to collect the scan are given in Section 3.2. A tensor map and an averaged $b=0$ image without diffusion weighting were calculated for this subject using the DTIFIT algorithm from the FSL library. Diffusion weighting was then applied to the averaged $b=0$ image by applying Equation 3 to produce a set of volumes with the same diffusion weighting scheme as was used to acquire the original DTI scan. Subject motion and eddy current effects were simulated by applying the inverse affine transforms which had been calculated to correct for these effects in the original DTI scan. The simulated scan could have been generated using any valid set of diffusion weightings or motion parameters, but the parameters generated from an actual scan provided a realistic test set. This process generated a set of diffusion weighted images simulated from a defined tensor map.

The simulated DTI scan was further processed to incorporate simulated data artifacts. Signal void artifacts induced by bulk motion were simulated by superimposing a phase adjustment on simulated images from an artificial motion profile and the relationship of Equation 7. The simulated images were oversampled by a factor of 4 in the x and y directions before the phase adjustment was applied. The Linux scripts used to

implement this simulation are listed in Appendix B. The motion profile was constructed to have the range of velocity and the frequency of occurrence of motion that was observed in Gulf War Illness study subjects. It was constructed by registering sections of the $b=0$ images without diffusion weighting to the whole volume of the averaged $b=0$ image. More specifically, a transform matrix was calculated for each axial slice by registering the image section of five temporally sequential slices to the whole $b=0$ image. The choice of using five slices was made to improve the stability of the registration because using a single slice proved to give erratic results. The x , y , and z rotational angles of the transform matrices were listed and smoothed. The smoothing was accomplished by restricting the rotation angle of a slice to be within the range of the median rotation angle of itself and the four previous angles and the median of the five subsequent angles. The change in angle between sequential slices was then used to calculate the angular velocity between slices. The angular velocities for 14 central slices from $b=0$ images of each subject were concatenated to make a single motion profile that was applied to the simulated image. The maximum rotational velocity of the profile was $6.7^\circ/\text{s}$ and 88 slices had a rotational velocity greater than $4^\circ/\text{sec}$. The oversampled images were transformed to k -space and re-sampled to simulate a partial k -space acquisition at the resolution of the original image.

Signal loss due to cardiac-induced motion was simulated using a mask of a potentially affected region of interest (ROI) and a timing profile of the image slice acquisition time relative to systole. The ROI mask was drawn by hand for a subject that had very evident periodic signal void in the region of the brainstem. The first $b=0$ image of the scan used to draw the ROI was registered to the first $b=0$ image of the scan used

for the simulation. The resulting affine matrix was used to transform the cardiac ROI mask to overlay the simulation image. The timing profile was generated to produce signal void artifact for 6% of the cardiac cycle for a heart rate of 72 beats per minute. The temporal order of the slices was used to determine which slices to simulate as occurring during the 6% of the cardiac cycle that produced artifacts. The signal for the portion of the slice falling within the ROI was reduced by 70%.

Signal loss due to vibration-induced artifacts was simulated using a mask of a potentially affected ROI and a profile of the multiplier for signal strength relative to the x component of the diffusion weighting direction. The ROI mask was drawn by hand for a subject that had very evident vibration-induced signal void artifacts. The first $b=0$ image of the scan used to draw the ROI was registered to the first $b=0$ image of the scan used for the simulation. The resulting affine matrix was used to transform the vibration ROI mask to overlay the simulated image. The profile of the signal strength multiplier was generated from the a and b parameters of Equation 13 that were calculated for a subject with extensive vibration artifact. The signal in the vibration ROI of each volume was multiplied by the signal strength multiplier appropriate for the direction of diffusion weighting.

Noise was added to the simulated images to produce datasets with realistic SNR. The amount of noise added to the images was estimated by measuring the noise in images without diffusion weighting ($b=0$) for a GWIS subject using the multiple scan method outlined by Dietrich (Dietrich, Raya et al. 2007). A region of interest (ROI) was delineated in the central portion of the lateral ventricles to provide a set of measurements with near constant signal. The standard deviation of the measured signals for each voxel

in the ROI was calculated and the average of these was used as an estimate of the signal variance for high signal in the image. The noise in the simulated images was modeled as being Gaussian noise of equal magnitude in the real and imaginary channels after Fourier transform of the signal collected in k-space. The conversion of the real and imaginary channels to a magnitude image then changed the noise distribution to a Rician distribution (Gudbjartsson and Patz 1995) as discussed above. The noise simulation was accomplished using the following relationship:

$$S_{(b,n)} = \sqrt{(S_{(b)} + N(\sigma_r))^2 + N((\sigma_i^2 N(\sigma_i))^2}$$

where: $S_{(b,n)}$ is the simulated noisy signal for diffusion weighting b ,
 $S_{(b)}$ is the simulated signal for diffusion weighting b ,
 $N(\sigma_r)$ is a random sample from a Gaussian distribution with the standard deviation of the noise in the real channel, and
 $N(\sigma_i)$ is a random sample from a Gaussian distribution with the standard deviation of the noise in the imaginary channel.

Finally, correction for eddy current distortion and for subject motion was applied with the EDDY_CORRECT algorithm of FSL and a brain mask was generated using the BET algorithm of FSL.

The presence of simulated artifacts in the data was quantified through visual evaluation. To provide for the most sensitive evaluation of motion-induced artifacts and cardiac-induced artifacts, the data were evaluated before noise addition and vibration artifact simulation. The visual evaluation of all simulated diffusion weighted slices was done using the following categories: “Motion-Induced Signal Void”, “Motion-Induced

Image Blurring”, and “Cardiac-Induced Signal Void”. Slices which appeared to have some regions of signal void were placed in the “Cardiac-Induced Signal Void” category if signal void was limited to the regions where cardiac pulsation was simulated. Other slices with signal void artifacts were placed in the “Motion-Induced Signal Void” category. Slices that had general image blurring caused by the motion-induced artifact simulation were placed in the “Motion-Induced Image Blurring” category.

3.2 Data Collection

UT Southwestern Medical Center conducted a study of veterans of the 1991 Persian Gulf War to investigate complexes of syndromes experienced by those veterans. The goals of this study included following up Haley’s MR spectroscopy results of 2000 (Haley, Marshall et al. 2000), extending earlier findings by including more MR modalities and testing a sample which was more representative of the veterans of the Gulf War. The Gulf War Illness study (GWIS) included 154 veterans of the 1991 Persian Gulf War. The first 57 subjects were members of the Twenty-fourth Reserve Naval Mobile Construction Battalion known as Seabees. These participated in a 2008-2009 follow-up to the 1997-1998 study and also served to pilot the battery of tests, including DTI, used in the subsequent 2009-2010 UT Southwestern study. The remaining 97 subjects were part of the 2009-2010 UT Southwestern study. They had been randomly selected from a sample of 8024 veterans who were given a comprehensive survey questionnaire and were representative of all veterans of the 1991 Persian Gulf War. The cohort of the 2009-2010 study is referred to here as the “national sample”. Each subject gave written consent to

participate in the study under a protocol approved by the Institutional Review Board of the University of Texas Southwestern Medical Center.

The subjects were categorized into 4 groups comprising the three distinct syndromes (1, 2, and 3) (Haley, Kurt et al. 1997) and a control group consisting of both non-deployed veterans and veterans deployed to the Iraq-Kuwait theater of the 1991 Persian Gulf War. The number of subjects in each group is given in Table 4. One subject from the Seabees did not fall into any of the four groups. DTI data are not available for 3 Seabees or for 3 national sample subjects.

Table 4. Number of subjects in each group in GWIS

Group	Seabees	National Sample
Control	16 ^a	31 ^b
Syndrome 1	11	21
Syndrome 2	17	24 ^c
Syndrome 3	12	21
Syndrome 5	1	0
Total	57 ^d	97 ^e

^a composed of 7 non-deployed and 9 deployed well veteran controls

^b composed of 15 non-deployed and 16 deployed well veteran controls

^c includes 5 subjects with both Syndrome 2 and Syndrome 4

^d DTI not available for 2 deployed well veteran controls or 1 Syndrome 3 veteran

^e DTI not available for 2 Syndrome 1 veterans or 1 Syndrome 2 veteran

The subjects were scanned on a Siemens Magnetom Trio Total Imaging Matrix (TIM) 3T scanner. Two sets of DTI sequence parameters were used, one to acquire diffusion weighted images with 2 mm isotropic resolution and the other to acquire images with 3 mm slice thickness and 1.25 mm in-plane resolution. The parameters for the 2 mm

DTI scans were: FA=90 deg, TR/TE=8300/82 ms, voxel size=2 x 2 x 2 mm³, axial FOV=256 x 256 mm², readout mode=2D EPI, pixel bandwidth=1395 Hz, acquisition matrix=80 x 128, reconstruction matrix=128 x 128, GRAPPA acceleration factor=2, number of reference lines for parallel imaging=38, partial k-space reconstruction=6/8, slice thickness=2 mm with no gap, and number of axial slices=64. This DTI scan sequence consisted of 6 reference images with b=0 and 50 diffusion weighted images with non-collinear diffusion directions and b=1000 s/mm². Vectors for the 50 directions are given in Appendix A. Two averages (scans) were acquired to increase image signal-to-noise. The head was completely contained in the FOV so that signal aliasing did not occur. The upper edge of the imaging volume was placed at the top of the brain and the lower edge included the brainstem to below the pons. The parameters for the 1.25 mm in-plane resolution DTI scans were: FA=90 deg, TR/TE=3300/85 ms, voxel size=1.25 x 1.25 x 3 mm³, axial FOV=160 x 160 mm², readout mode=2D EPI, pixel bandwidth=1345 Hz, acquisition matrix=80 x 128, reconstruction matrix=128 x 128, GRAPPA acceleration factor=2, number of reference lines for parallel imaging=38, partial k-space reconstruction=6/8, slice thickness=3 mm with no gap, and number of axial slices=25. The DTI scan sequence consisted of 12 reference images with b=0 and 100 diffusion weighted images with 50 non-collinear diffusion directions and b=1000 s/mm². Vectors for the 50 directions are given in Appendix A. Three averages (scans) were acquired to increase image signal-to-noise.

The 160 x 160 mm² FOV was not large enough to completely contain the head so signal aliasing occurred. The amount of head not contained within the FOV varied depending on the subject's head size. Some cases had very little aliasing with just the

nose wrapping around to superimpose upon the occipital lobe. In other cases, signal from the eyes wrapped around to superimpose upon the occipital lobe and the nose was superimposed on the superior portion of the cerebellum. In the example of aliasing presented in Figure 11, the nose extended 56 mm (35% of the A-P dimension) into the posterior portion of the brain to about the straight sinus. Although in some cases the FOV did not cover the head completely in the left-right direction, the aliased signal from the scalp only extended a few mm into the frame and was not superimposed upon the brain. The imaging volume was placed to cover the brainstem with the superior edge of the volume placed just above the thalamus.

Tensor fitting was performed using the linear least squared errors method implemented in the DTIFIT algorithm of FSL. The tensors were fit after the diffusion weighted images had been co-registered with the EDDY_CORRECT algorithm of FSL to compensate for subject motion and eddy current effects. For those scans containing signal void artifacts, the additional steps described in Section 3.4 were applied. The vectors describing the diffusion weighting directions were rotated to correct for the change in orientation which occurred during motion correction. A brain mask was constructed for the first $b=0$ volume of the whole head FOV scans using the Brain Extraction Tool (BET) in FSL (Smith 2002). This mask was back transformed through the motion correction to generate a brain mask for each volume of the DTI scan. A brain mask was constructed for the small-FOV scans using the method described in Section 3.6.

3.3 Detection of Signal Void Artifacts

In order to reduce signal void artifacts in a DTI scan, the artifacts must first be

detected. Careful visual inspection of all diffusion weighted images of a study the size of the GWIS would be very labor intensive, because the number of diffusion weighted image slices collected for the GWIS exceeds 2 million. Therefore, signal void detection algorithms were developed to automatically detect the artifacts. One algorithm was developed to detect signal void artifacts due to vibrations and a second algorithm was developed to detect other signal void artifacts. Both of these algorithms rely on comparing the measured signal to the signal that would be expected if no artifacts were present.

3.3.1 Simulation of diffusion-weighted signal using RESTORE

The expected signal was simulated by first using the RESTORE algorithm implemented in the Camino diffusion MRI toolkit (Chang, Jones et al. 2005; Cook, Bai et al. 2006) to calculate an initial estimate of the tensors and by then using the estimate of the tensors to calculate the expected diffusion weighted signal from those tensors. The Linux script used to implement this simulation is listed in Appendix C.

The RESTORE algorithm removes most of the signal void artifacts so that the simulated signal will be close to the expected signal even when artifacts are present in the raw data, as described in Section 1.4.2.5. However, as also noted in Section 1.4.2.5, the RESTORE algorithm may introduce bias by excluding data samples identified as outliers to the tensor model even though those samples are accurate measures of diffusivity from tissue which is not well described by a single tensor. This potential bias is not a concern here in the artifact detection method because that degree of error in the estimated tensors will not reduce the estimated signal in any diffusion direction to nearly the degree that the

signal void artifact reduces the signal in affected slices. It is also this consideration which makes the accuracy of a noise estimate for RESTORE less critical for artifact detection. Variation in the noise estimate affects the threshold used by RESTORE to identify outliers, but the resulting changes to the signal estimated using the tensors will be small compared to the signal reduction caused by signal void artifacts. The noise estimate required as input to the RESTORE algorithm was calculated by the difference method as described by Dietrich (Dietrich, Raya et al. 2007). The ROI used for the noise calculation was the brain mask generated using the BET algorithm of FSL. As there were two volumes collected for each of 50 diffusion weighting directions, the difference of these pairs of images were used to calculate the noise at each slice so the number of noise estimates is 50 times the number of slices. These noise calculations assume that corresponding voxel intensities in the image pairs are measures of identical signal intensities. Imaging considerations, such as subject motion and image artifacts, undermine this assumption and inflate the noise calculation. The lowest noise estimate from all the slices is potentially the least affected by motion and artifacts. A brain mask was used when calculating the noise to exclude peripheral voxels where noise characteristics change due to parallel imaging. To avoid slices of the mask containing only a few voxels, only noise estimates from the central slices of the volumes were considered. The minimum noise estimate from the central slices of all diffusion directions was used as the noise estimate for the RESTORE algorithm's tensor fitting routine.

The tensors $D(x,y,z)$ and the non-diffusion weighted image $S_0(x,y,z)$ used for artifact detection were calculated using the RESTORE algorithm on the DTI scan being analyzed after the data was corrected for subject motion and eddy current distortion. The

relationship between the diffusion weighted and the non-diffusion weighted signal given in Equation 3 is rearranged below as Equation 10. The expected diffusion weighted signal was then calculated using Equation 10 with the set of \mathbf{b} vectors from the DTI scan being analyzed. The expected signal for motion corrected images was used for detecting vibration artifacts. For detection of other signal void artifacts, $\mathbf{D}(x,y,z)$ and $S_0(x,y,z)$ were back transformed through the motion and eddy current correction referred to in Section 3.1. For each volume v , of the simulated scan, a tensor map $\mathbf{D}(x,y,z,v)$ and a non-diffusion weighted image $S_0(x,y,z,v)$ were generated. Equation 11 was then applied to the transformed tensors to produce the expected diffusion weighted signal. The resulting images of the expected signal were used in the signal void detection algorithms.

$$S_b(x, y, z, v) = S_0(x, y, z) e^{-\mathbf{b}(v) \mathbf{D}(x,y,z)} \quad (10)$$

$$S_b(x, y, z, v) = S_0(x, y, z, v) e^{-\mathbf{b}(v) \mathbf{D}(x,y,z,v)} \quad (11)$$

3.3.2 Detection of artifacts due to vibrations

The method for detecting artifacts induced by vibration requires knowledge of the expected signal $S_b(x,y,z,v)$ to estimate the signal multiplier $A(x,y,z,v)$ in regions affected by vibration. The dependence of the vibration artifact on the diffusion weighting direction as discussed in Section 1.4.2.3 provides a basis for detecting which voxels contain the artifact. Gallichan presented a method using a co-regressor during tensor calculation to account for the influence of vibration artifacts (Gallichan, Scholz et al. 2010). He designed the co-regressor to be a function of the signal multiplier measured in affected areas with respect to the x component of the diffusion direction. He used least-

squares fitting to determine the parameters for Equation 13 given below. A similar process was used here to develop co-regressors. The Linux scripts used in the process of detecting artifacts due to vibrations are listed in Appendix D. A co-regressor was designed for each DTI scan using Equation 13. An initial estimate of the affected region was used to collect signal multipliers $A(x,y,z,v)$. The signal multiplier for voxel x,y,z in volume v is defined as the ratio of the measured signal $I(x,y,z,v)$ to the expected signal $S_b(x,y,z,v)$ as given in Equation 12. The signal multiplier at index $r_{x,i}$ was then fit to Equation 13.

$$A(x, y, z, v) = \frac{I(x,y,z,v)}{S_b(x,y,z,v)} \quad (12)$$

$$\begin{aligned} A(r_{x,i}) &= 1 & r_{x,i} < a \\ A(r_{x,i}) &= \cos^2\left(\frac{\pi(abs(r_{x,i})-a)}{2b}\right) & a < r_{x,i} < a + b \\ A(r_{x,i}) &= 0 & r_{x,i} > a + b \end{aligned} \quad (13)$$

where $r_{x,i}$ is the x component of the diffusion weighting direction for voxel i in the collection of all voxels in the affected ROI, and the sum of the squared errors was minimized with parameters a and b .

The co-regressor that Gallichan derived for one of his subjects was adopted as the initial co-regressor for use in establishing the initial estimate of the affected area. His co-regressor was defined by Equation 13 with $a=0.61$ and $b=0.54$. The co-regressor was used with the DTIFIT algorithm to determine the strength of the co-regressor effect k for each voxel. All voxels for which k exceeded 0.3 were included in the initial estimate of the area affected by the vibration artifact which was then morphologically filtered. The morphological filtering was a 2D erosion of one voxel followed by a 2D dilation to

restore the original mask without the noise. This approach was chosen based on visual inspection of the unfiltered masks. The parameters of 0.3 for the threshold and one voxel for the erosion and dilation were chosen to make the procedure sensitive to areas with the most visually evident vibration artifacts while excluding isolated voxels at the brain surface which were likely due to slight registration errors. The signal multipliers for voxels in the initial estimate of the affected area were calculated and used to recalculate the parameters a and b of Equation 13. The voxel multipliers were averaged for each diffusion direction and a linear regression against the x component of the direction was performed. Just as the function defined in Equation 13 has a value of 1.0 from 0 to the breakpoint at a , the average signal multipliers for scans with vibration artifacts were clustered around 1.0 until a breakpoint after which the values decrease approximately linearly with the x component of the diffusion direction. The breakpoint was defined as the largest x component for which the averaged signal multiplier was at least 1.0. When at least three averaged signal multipliers lay beyond the breakpoint, a linear regression was used to estimate the portion of the curve above the breakpoint. It was assumed that a vibration artifact was not detected if the estimated slope was not negative as the modeling equation requires. The parameter a was set where the line crossed 1.0 and $a + b$ was set to the point where the line crossed 0. This produced a visually close fit between the plot of the multipliers and the plot of Equation 13. When the value of a was greater than 0.6, the vibration artifact was detected using Equation 13 to design a co-regressor with the new values for a and b . When the values of a was less than 0.6, the vibration artifacts were not evaluated. The value of 0.6 was chosen as the lower limit to prevent calculating tensors for the GWIS data with fewer than 30 diffusion directions.

This new co-regressor was used with the DTIFIT algorithm to determine the strength of the co-regressor effect k . All voxels for which k exceeded 0.5 were included in the refined estimate of the area affected by vibration artifact. The threshold of 0.5 was found to give better results than 0.3 as used above. This is presumably because the regressor used here was tailored to the scan being analyzed. The refined estimate of the vibration ROI was filtered morphologically to remove small areas which were assumed to be noise. The morphological filtering was performed as described above. The resulting vibration artifact mask was used in removing the artifact from the tensor map and was also used in refining the search for other signal void artifacts as described below.

3.3.3 Detection of artifacts other than those due to vibrations

Signal void artifacts other than vibration artifacts were detected by comparing the measured signal $I(x,y,z,v)$ to the expected signal $S_b(x,y,z,v)$ in brain tissue not affected by vibration artifacts. The Linux scripts used in the process of detecting signal void artifacts other than those due to vibrations are listed in Appendix E. The brain mask was modified by the vibration artifact mask and then morphologically filtered in the axial plane with a 2D erosion of two voxels. The erosion of 2 voxels was performed to reduce the impact of large differences at the surface of the brain caused by slight registration errors while not greatly reducing the area of the mask. The measured signal $I(x,y,z,v)$ was subtracted from the expected diffusion weighted signal $S_b(x,y,z,v)$ to give a residual $R(x,y,z,v)$. The distribution of the residuals in each slice was analyzed to determine if there was a signal void artifact in that slice. When a signal void artifact affects a large portion of a slice, the average residual of the slice is greater than zero. However, if a

signal void artifact only affects a small area of a slice, the average residual may actually be negative even though many individual residuals are very positive. Therefore a robust maximum of the residuals was used instead of the average of the residuals. Using a robust maximum rather than an absolute maximum reduces the bias that would be caused by outliers. The 95th percentile of the residuals $R_{p95}(z,v)$ was selected as the robust maximum. $R_{p95}(z,v)$ was compared across diffusion weighted volumes at slice z and a robust z-score was calculated. Using a robust z-score reduces the influence of signal void artifacts during the comparisons. For slice z of volume v the robust z-score $Z(z,v)$ was calculated by subtracting the median $R_{p95}(z,v)$ for all v from $R_{p95}(z,v)$ and dividing by a robust estimate of the standard deviation. The robust estimate of the standard deviation was computed by multiplying the interquartile range (the difference between the 75th percentile of $R_{p95}(z,v)$ for all v and the 25th percentile of $R_{p95}(z,v)$ for all v) by 0.74. The factor 0.74 normalizes the interquartile range to the standard deviation for a normal population. Any slice which had a z score $Z(z,v)$ which exceeded a specified threshold was flagged as having a signal void artifact.

The threshold for $Z(z,v)$ at which a slice was identified as having artifacts was determined through visual evaluation of the dataset. This was accomplished for both the simulated data and the GWIS data by reviewing image slices with z-scores greater than 10 for visual evidence of signal void artifacts. For the simulation data, the quantification of artifacts described in Section 3.1 was reorganized by grouping “Motion-Induced Signal Void” and “Motion-Induced Image Blurring” into the category of “Motion-Induced Artifacts”. Additionally, the flagged slices for the simulation data were reevaluated to check for vibration induced artifacts that may have been missed in the

vibration artifact detection algorithm. To provide for the most sensitive evaluation of the GWIS data, the data were evaluated before eddy current correction to avoid the smoothing that is introduced by image interpolation. The visual evaluation of the GWIS slices was done using the following categories: “Motion-Induced Artifacts”, “Cardiac-Induced Artifacts” and “No Artifacts”. Slices which appeared to have some regions of signal void were placed in the second category if signal void was limited to regions near the brainstem area. Other slices with signal void artifacts were placed in the first category. Slices which had other types of artifacts or which had regions that were slightly darker than expected, but which did not have clear signal void artifacts, were not counted. Slices that appeared normal even though they were flagged for review were placed in the “No Artifacts” category. If motion-induced artifacts were discovered, the threshold was decreased by 1 and the newly flagged slices were reviewed for artifacts. This process was iterated until the newly added slices did not have visually identified motion-induced signal void artifacts. Having identified signal void artifacts, the data affected by artifacts must be excluded from the tensor calculations.

3.4 Reduction of Signal Void Artifacts

Diffusion weighted data flagged in the signal void detection process was excluded from the tensor calculation. This was accomplished differently for the vibration artifacts and the other signal void artifacts. The vibration artifacts were reduced by calculating the tensors for voxels affected by the artifact without using any data from volumes that were affected by vibration. The volumes that were excluded were those with an x component of the diffusion weighting direction greater than the parameter “ a ” used

with Equation 13. The x dependence of the vibration effect as discussed in Section 1.4.2.3 is machine dependent. This orientation for the vibration effect was chosen because it has been observed on the Siemens scanner used for the GWIS. The other signal void artifacts were reduced by calculating the tensors after excluding any slices flagged as having signal void. This was accomplished by determining which diffusion weighted volumes contributed data affected by signal void to each slice of the tensor map and calculating tensors with the unaffected volumes. The Linux scripts used in the process of removing signal void artifacts are listed in Appendix F.

A four dimensional (4D) mask (3 spatial dimensions and one dimension to specify the diffusion weighted volume) of the signal void artifacts was generated for each DTI scan. Any slice flagged as having the artifact received a 1 at every voxel and all other voxels in the volume received a 0. This mask was then transformed through the eddy current and motion correction that had been applied to that DTI scan. This placed the artifact masks in the same orientation as the eddy current corrected data. A list of the volumes containing artifact masks at a given slice level was made for each slice. A separate tensor map was made using the DTIFIT algorithm for each unique combination of volumes that contributed uncorrupted data to the tensor map. The tensor maps were then combined slice by slice to form one artifact free tensor map. The necessity of removing signal void artifacts before calculating a tensor map can be seen in the effects such a correction has on the FA map calculated for a DTI scan.

3.5 Effect of Artifact Exclusion on FA

The impact of signal void artifacts on the FA map of a single DTI scan was

visualized by comparing the FA map when signal void was present in the data to when it had been removed. The effect of excluding signal void artifacts when calculating the tensor map for a DTI scan was demonstrated in a more rigorous way by examining the changes in the FA map when the artifacts were excluded. The effect of signal void artifacts on FA was first quantified with simulated data and then demonstrated with data from the GWIS.

Since the simulated data were generated from a defined set of tensors, the true FA values for the simulation could be directly computed. Three additional FA maps were computed from the three simulated DTI scans. The first FA map was computed for the baseline simulated DTI scan which had no simulated artifacts. The second FA map was computed for the simulated DTI scan corrupted with simulated artifacts. The third FA map was computed for the simulated DTI scan with the simulated artifacts reduced using the methods described above. Since the simulation process includes resampling k-space data and adding noise, the FA map calculated from the baseline simulation DTI scan is not identical to the original FA map used to generate the simulations. Therefore, the maximum differences between the FA generated by the simulation process being tested and the original FA were calculated for each slice of the FA map and these were compared to the maximum differences between the FA for the baseline simulation and the original FA. An additional comparison was made to determine if the FA of the simulation with artifacts removed was significantly closer to the FA of the baseline simulation than was the FA of the simulation which included signal void artifacts. Finally, the maximum differences between the FA of the simulation with signal void artifact and the FA of the baseline simulation were calculated for each slice of the FA map and these were

compared to the maximum differences between the FA of the simulation with signal void artifacts removed and the FA for the baseline simulation. The maximum of the FA differences was calculated for each slice using the “-r” option in the FSLSTATS algorithm of FSL to obtain a more robust solution than would have obtained using the simple maximum. To exclude voxels from the periphery and from grey matter areas, a mask was applied which excluded voxels with FA less than 0.2 or with mean diffusivity (MD) less than one half of the average mean diffusivity.

A paired t test was performed to determine if the FA differences between the simulation being tested and the original FA were greater than the FA differences of the baseline simulation and the original FA. Pairs of FA differences were collected from each slice for which signal void artifacts had been flagged. The two simulation processes tested were the simulation process which included simulated signal void artifacts and the simulation process which removed flagged signal void artifacts. A final paired t test was performed to determine if the FA differences between the simulation with signal void artifacts and the baseline simulation were greater than the FA differences between the simulation with signal void artifacts removed and the baseline simulation. The Linux scripts used to collect these comparison data are listed in Appendix G. These tests of the FA differences on simulated data were used to quantify the effect which the signal void artifacts included in the simulation have on FA. The actual occurrence of such differences in real DTI data was investigated using GWIS DTI data.

Three FA maps were generated for each DTI scan of the GWIS. The first FA map was computed from tensors fit from all the data. The second FA map was computed from tensors fit after signal void artifacts were reduced. The third FA map was computed

as a control from tensors fit with an alternate volume removed in place of removing a volume flagged for signal void artifacts. The alternate volume removed was that volume which had the same diffusion weighting as the flagged volume. If the volume having the same diffusion weighting direction was also flagged for removal, then two alternate volumes with similar diffusion weighting as the flagged volumes were removed. The maximum changes in FA caused by removing data flagged for artifacts were calculated for each slice of the FA map. These were compared to the maximum changes in FA caused by removing data from alternate volumes to the ones flagged for artifacts. The Linux scripts used to collect these comparison data are listed in Appendix H. A paired t test was performed to determine if the FA changes caused by removing signal void artifacts were greater than the FA changes caused by removing alternate volumes. A t test was performed for each subject that had signal void artifacts removed. A comparison was also made using data from all the slices in the GWIS that had signal void removed.

The test using a simulated DTI scan quantified the effect of signal void artifacts on FA and the test using GWIS DTI scans demonstrated whether removing signal void artifacts from real DTI scans had a measurable effect on FA. These tests address the first goal of this research. The second goal of this research is to address the impact of aliased signal on small-FOV DTI.

3.6 Mitigating the Impact of Aliased Signal

For DTI scans acquired with an FOV smaller than the head, *a priori* knowledge of the geometry of the imaged object was used to identify which voxels were significantly influenced by aliased signal. A lower resolution image acquired with an

FOV sufficiently large to cover the whole head, but having similar contrast and geometric distortion as the images without diffusion weighting, was rescaled, translated and replicated with a period equal to the dimensions of the smaller FOV. This was done to simulate the aliased signal that was present in the small-FOV image. The proper scaling and translation for the whole head image was determined from the position and voxel dimension data contained in the image headers. Replication of the data simulated the effect of the discrete Fourier transform of k-space which is the cause of aliasing as discussed in Section 1.4.4.3. A binary mask of the replicated signal that fell within the simulated FOV was generated. A threshold of 50 was used for making the binary mask. This level was set to be greater than the background noise of the lower resolution image.

The whole head image was then registered to the small-FOV image using the FLIRT algorithm of FSL. The aliased signal mask was used as a binary weighting file for the reference volume during image registration. The effect of the weighting file was to exclude aliased signal from being used in calculating the cost functions during registration. An initial estimate of the transform, generated using the position and voxel dimension data contained in the image headers, was provided as input to the FLIRT algorithm. The resulting affine transform corrected for any net movement of the subject between the acquisitions for the two images. The new registration was used to transform and replicate the whole head image again to refine the mask of aliased signal. The brain mask computed for the whole head image was also transformed to the small-FOV image. The standard brain mask available with the FSL software was used for the extreme inferior portion of the brain when the FOV of the whole head image did not extend far enough in that direction. The Linux script used to generate an aliased signal mask and to

adapt brain masks to the small-FOV images are listed in Appendix I. Figure 12 shows a slice from a whole brain FOV image on the top left and the corresponding slice from a small-FOV image on the top right. The signal outside the green box overlaying the whole brain image would have been superimposed inside the box if the FOV had been set to that size. The light blue masks in the bottom image panels depict the projection of aliased data onto the small-FOV image. The yellow mask in the bottom right is the brain mask from the whole brain FOV registered to the small-FOV image.

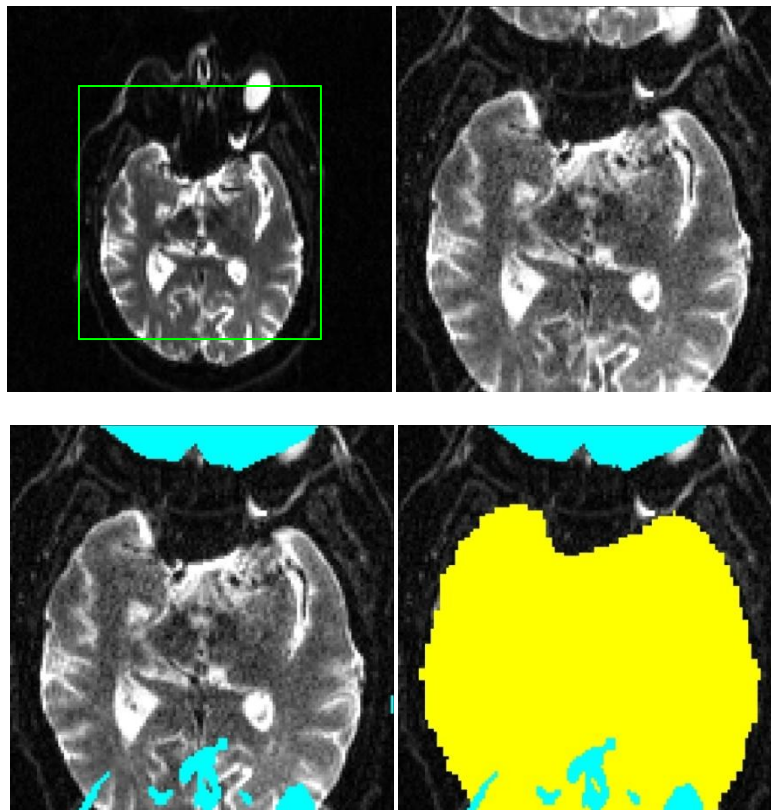


Figure 12. Brain mask for image with aliased signal: The FOV of the top left image covers the whole brain. The FOV of the top right image is smaller than the brain and exhibits aliased signal. The light blue mask on the bottom left depicts the projection of aliased data as estimated from the whole brain FOV image. The yellow mask in the bottom right shows the small-FOV image overlaid with the brain mask calculated for the whole brain FOV.

This method of predicting areas corrupted by aliased signal and generating a brain mask was applied to the GWIS data to register the whole head non-diffusion weighted image to the small-FOV image. Using the methods described here for removal of signal void artifacts and masking of aliased signal prior to image analysis, both the whole brain FOV and small-FOV GWIS DTI data were prepared for TBSS analysis.

3.7 TBSS Analysis of GWIS Data

The DTI data collected for the Gulf War Illness study were analyzed using the TBSS algorithm of FSL. For the whole head FOV DTI scans, the algorithm was used without modification. For the small-FOV DTI scans, a slight modification was made in the mask applied to the registered FA maps by the TBSS algorithm. This modification was required to remove voxels containing aliased signal from data analysis and to exclude regions inappropriately extrapolated beyond image boundaries by the non-linear registration. The limited extent in the superior direction of small-FOV DTI scans occasionally allows the non-linear registration used in TBSS to excessively extrapolate the region of the corpus callosum beyond the image boundary in the superior direction. The modification used to address these issues first adjusts the brain masks calculated by the BET algorithm of FSL by removing voxels where aliased signal is predicted to occur. The modified masks are then transformed with the affine matrices that the TBSS algorithm used for the scans. All transformed brain masks were superimposed so that only voxels valid in all FA maps were included in the final mask.

The Seabees study data and the national sample study data were analyzed separately since those studies are not drawn from the same population. The skeletonised FA maps generated with the TBSS algorithm were tested using the RANDOMISE algorithm of FSL to detect possible group differences. The first test was between the deployed and non-deployed control subjects. Absence of significant differences between the groups was used as the criterion for pooling the non-deployed controls with the deployed controls. The second test was between the national sample subjects with only Syndrome 2 and the national sample subjects with both Syndrome 2 and Syndrome 4.

Absence of significant differences between the groups was used as the criterion for pooling the subjects with both Syndrome 2 and Syndrome 4 with the subjects with only Syndrome 2. Subsequent to determining if the non-deployed controls would be pooled with the deployed controls, the deployed control group was compared to each of the three syndrome groups.

Since FA has been shown to decrease with age (Bhagat and Beaulieu 2004; Wu, Field et al. 2011; Lebel, Gee et al. 2012; Sala, Agosta et al. 2012), age was included as a confounding factor in the RANDOMISE analysis. The average age of subjects in each group are given separately for the Seabees and the national sample participants in Table 5 and Table 6 respectively. Other possible covariates such as gender (Huster, Westerhausen et al. 2009; Liu, Vidarsson et al. 2010; Chou, Cheng et al. 2011; Menzler, Belke et al. 2011; Wu, Field et al. 2011), PTSD or post traumatic stress disorder (Abe, Yamasue et al. 2006; Kim, Jeong et al. 2006; Schuff, Zhang et al. 2011; Zhang, Zhang et al. 2011), and MDD or major depressive disorder (Li, Ma et al. 2007; Kieseppa, Eerola et al. 2010; Zhu, Wang et al. 2011) may also account for some of the variance in the data and should be included in a full analysis, since they have been reported to affect FA and other parameters characterizing white matter. However, a comprehensive analysis of the GWIS DTI data is beyond the scope of this research, which is focused on methods for removing artifacts. Therefore the utility of the methods presented here were tested without including gender, PTSD, and MDD in the data analysis. The RANDOMISE routine was also used to test for differences between the FA maps generated from whole brain FOV scans and from the small-FOV scans by comparing the control group of the whole brain FOV data to the control group of the small-FOV data. The same comparison

was made for each of the three syndrome groups.

Table 5. Average Age of GWIS Seabees Participants

Group	Number in Group	Average Age	Stdev of Age
Control	17	61.2	6.6
Syndrome 1	11	51.4	6.1
Syndrome 2	17	62.9	6.4
Syndrome 3	13	56.8	6.3

Table 6. Average Age of GWIS National Sample Participants

Group	Number in Group	Average Age	Stdev of Age
Control	32	49.7	7.9
Syndrome 1	21	48.2	8.6
Syndrome 2	24	49.8	8.0
Syndrome 3	22	51.3	7.8

This method of analysis was applied for both the whole head FOV data and the small-FOV data once without making adjustments for signal void artifacts and once after making the adjustments. The conclusions drawn from each of these analyses were compared to see if adjusting for signal void artifacts impacted the conclusion of the DTI sub-core of the GWIS.

CHAPTER FOUR

RESULTS

4.1 Simulation of DTI Scans with Signal Void Artifacts

Graphs of the rotational velocities collected from $b=0$ images of the GWIS DTI scans are presented in Figure 13. These were used for simulating the effects of rotational motion on signal strength as discussed in Section 1.4.2.1. The hand drawn masks for simulating the vibration artifacts and the cardiac pulsation artifact are depicted in Figure 14. Figure 15 depicts the vibration artifact regressor which was used for simulating the vibration artifact in the simulated DTI scan.

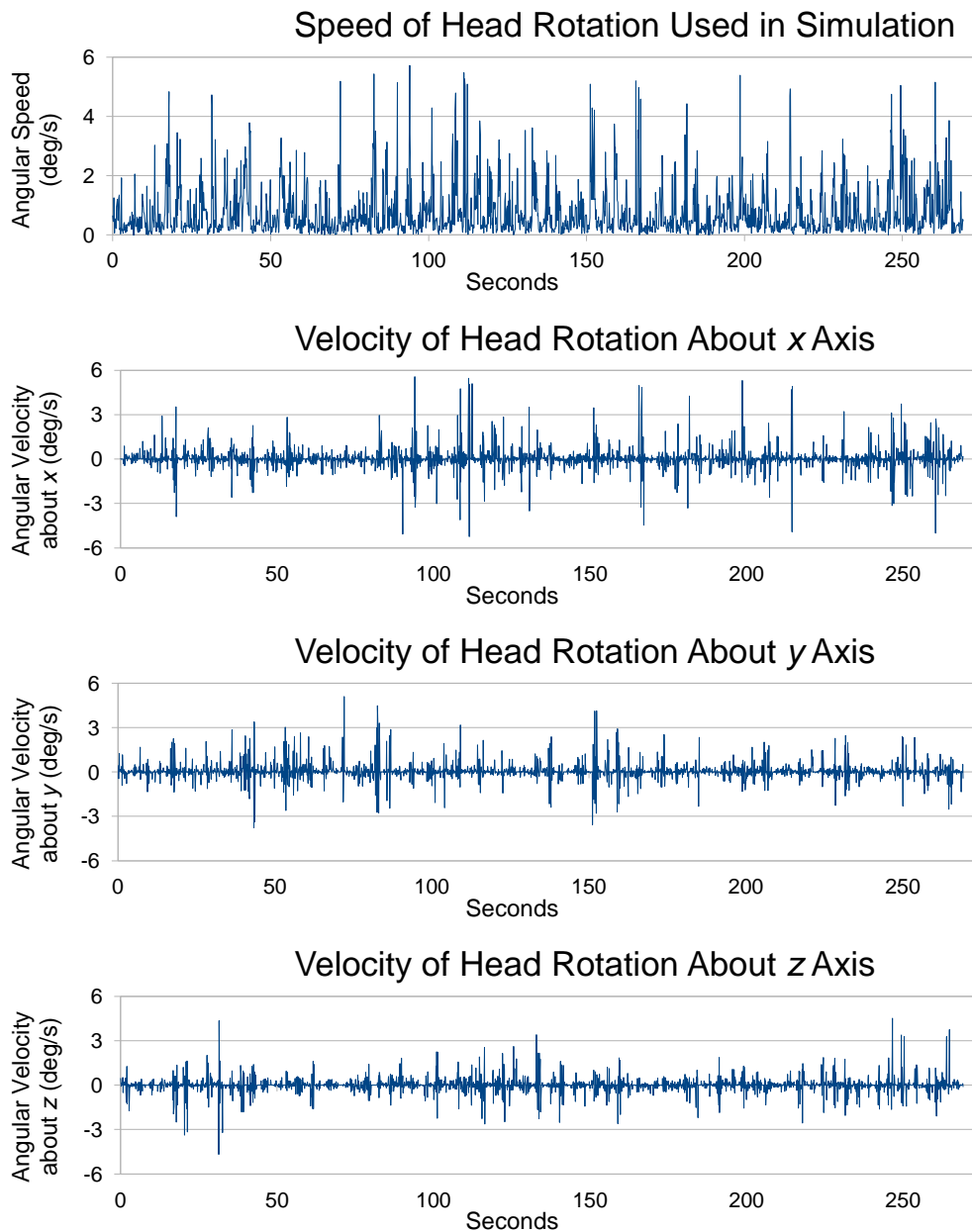


Figure 13. Rotational velocity of simulated head motion: The angular speed of the simulated head rotation is presented in the top panel. The x, y, and z components of the angular velocity of the simulated head rotation are presented in the lower panels.

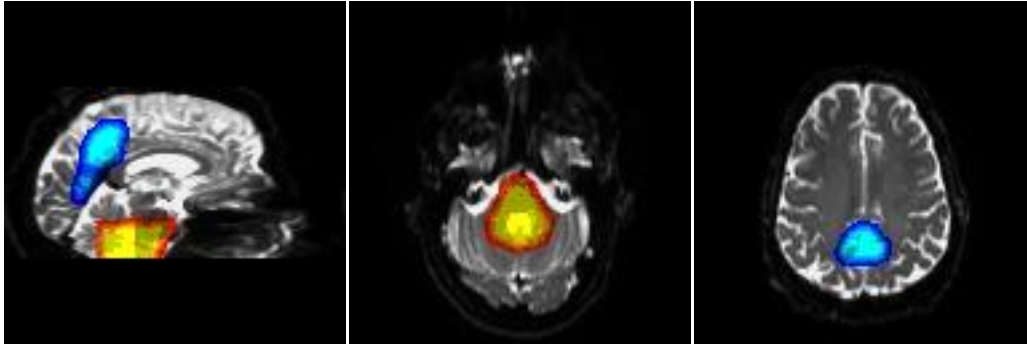


Figure 14. Masks for cardiac pulsation and vibration artifacts: Hand drawn masks were used in simulating signal void from vibration artifacts and cardiac pulsation artifacts. The signal under the light blue mask was multiplied by the value of the vibration regressor for the x component of the diffusion weighting. The signal under the yellow mask was multiplied by 0.3 when the simulated slice timing was within the first 6% of the cardiac cycle.

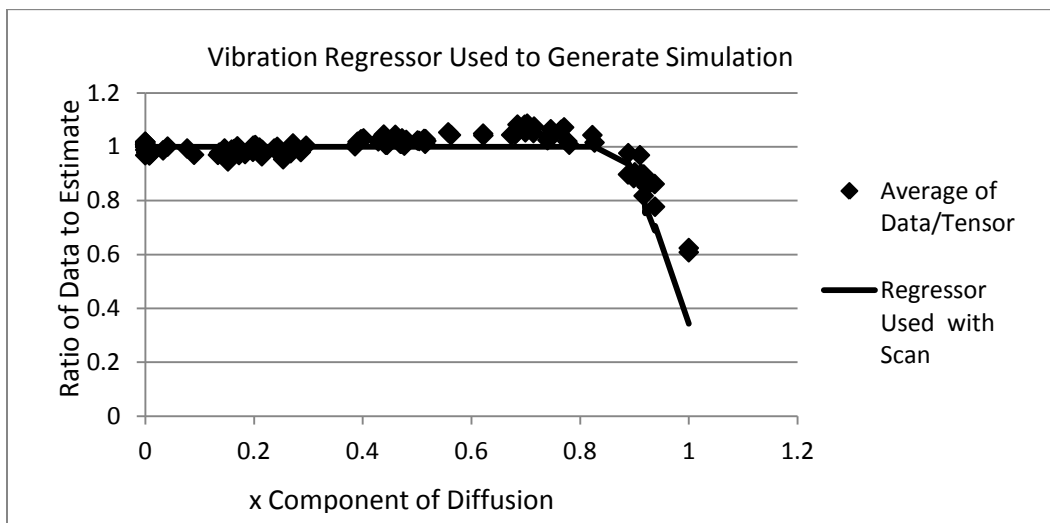


Figure 15. Vibration effect used for simulating the vibration artifact: Data were collected in an ROI of vibration artifacts in a scan of the GWIS. The expected values were calculated from tensors derived with the RESTORE algorithm and ratios of the actual data to the estimated were compiled. The line plots the regressor that was calculated for use with the DTIFIT algorithm.

The standard deviation of the noise of the GWIS scan that was used as a basis for the simulated DTI scan was 27.3 as calculated using the multiple scan method

outlined by Dietrich (Dietrich, Raya et al. 2007). The region of interest (ROI) for measuring the noise was a central portion of the lateral ventricles chosen to provide a set of measurements with constant signal. Independent Gaussian noise files with mean=0 and standard deviation=24.0 were added to simulate noise in the real and imaginary channels after the Fourier reconstruction as discussed in Section 3.1. The standard deviation of the resulting noise in the simulated image was 26.3. Figure 16 presents slices from a) the GWIS image used as the basis for the simulation, b) the simulated DTI scan before noise addition, and c) the simulated DTI scan after noise addition. Panels a through c are from a $b=0$ volume and Panels d through f are from a diffusion weighted volume with $b=1000$ s/mm^2 in the direction $[x,y,z] = [1.00,0.00,0.00]$.

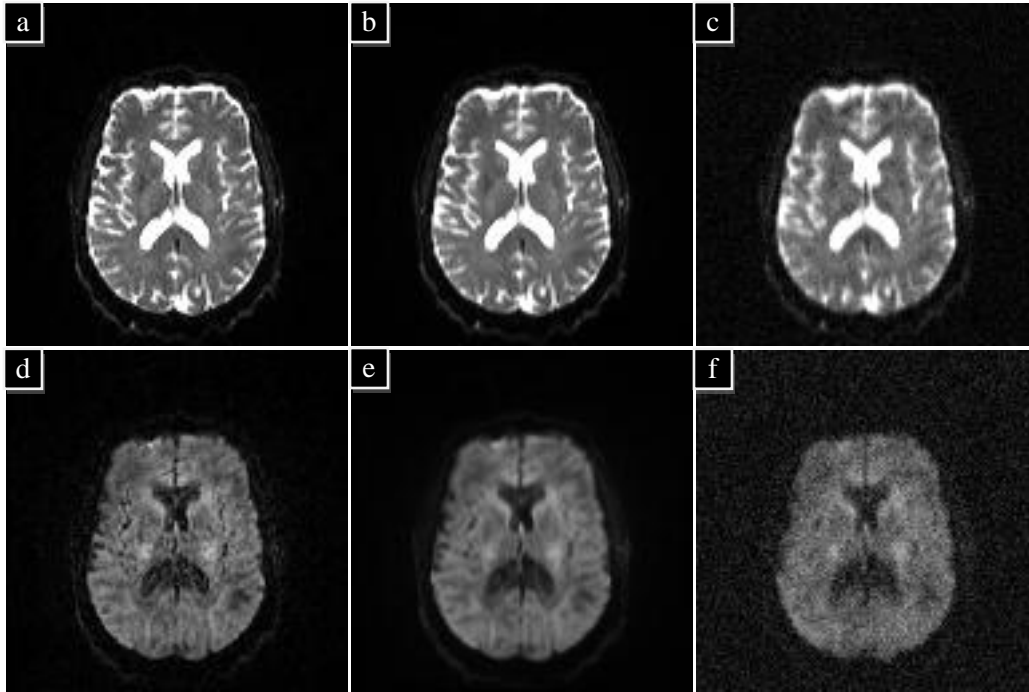


Figure 16. Simulated noise: The upper images are from a $b=0$ volume and the lower images are from a diffusion weighted volume with $b=1000 \text{ s/mm}^2$ in the direction $[x,y,z] = [1.00,0.00,0.00]$. The images on the left (a,d) are slices from a GWIS DTI scan. The images in the center (b,e) are slices from the simulated DTI scan before noise addition and the images on the right (c,f) are from the simulated scan after noise addition. (The intensity of the diffusion weighted images is scaled differently for display than is the intensity for $b=0$ images.)

A visual inspection of all 6400 diffusion weighted slices of the simulated DTI scan before noise addition produced the results given in Table 7. The slices identified as having motion-induced signal void were much darker than images without the artifact. An example of a slice in this category is given in Figure 17. The slices identified as having motion-induced image blurring did not have major signal loss, but blurring was evident. The region in which cardiac-induced signal void artifacts were simulated is depicted in Figure 14. This region was contained within the lowest 14 slices of the scan. The slices identified as having cardiac-induced signal void were much darker in the

region where the artifact was simulated. In addition to evaluating slices for the presence of motion-induced and cardiac-induced signal void artifacts, the presence of vibration-induced signal void artifacts was evaluated on a volume by volume basis. The artifacts appeared as dark regions in the medial parietal lobes for a limited number of diffusion weighted volumes. During the visual inspection, 3 volumes (3, 59, and 93) were detected to have vibration-induced signal void artifacts. These volumes had direction vectors $[x,y,z]$ of $[1,0,0]$, $[1,0,0]$, and $[0.94,0.34,0.08]$ respectively.

Table 7. Visually detected artifacts in simulated DTI scan.

Total # slices	Motion-induced signal void	Motion-induced image blurring	Cardiac-induced signal void
6400	8	62	75

An example of a slice with simulated motion-induced signal void artifact is presented in Figure 17 along with an image from the GWIS with motion-induced signal void artifact for comparison. The comparison image is the same as slice 36 of the volume displayed in Figure 3.

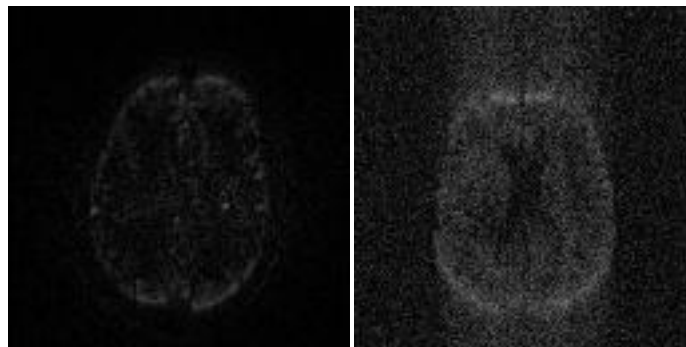


Figure 17. Simulated motion-induced signal void artifact: On the left is an image acquired during subject motion. On the right is an image with simulated motion-induced signal void artifact.

Slice 32 of the FA map calculated from a simulated DTI scan with no simulated artifacts is depicted in the left panel of Figure 18. The same slice for the FA map calculated from the original tensors is in the right panel.

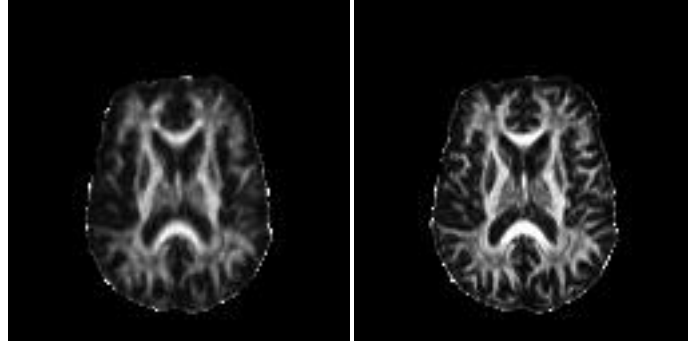


Figure 18. FA map from simulated DTI scan and original FA: The panel on the left is the FA map calculated from the simulated DTI scan. The panel on the right is the FA map calculated from the original tensors used to make the simulation.

4.2 Detection of Signal Void Artifacts

4.2.1 Detection of vibration artifacts

The parameters used with Equation 13 to define the vibration artifact co-regressor for the simulated DTI scan were $a=0.90$ and $b=0.19$. Plots of the co-regressor and the data used to design it are given in Figure 19. The co-regressor was used with the DTIFIT algorithm to generate a mask for the vibration artifact. Slices of that mask are overlaid on the third volume of the simulated DTI scan in Figure 20. The third volume was acquired with a diffusion weighting of $b=1000 \text{ s/mm}^2$ and direction $[x,y,z]=[1,0,0]$.

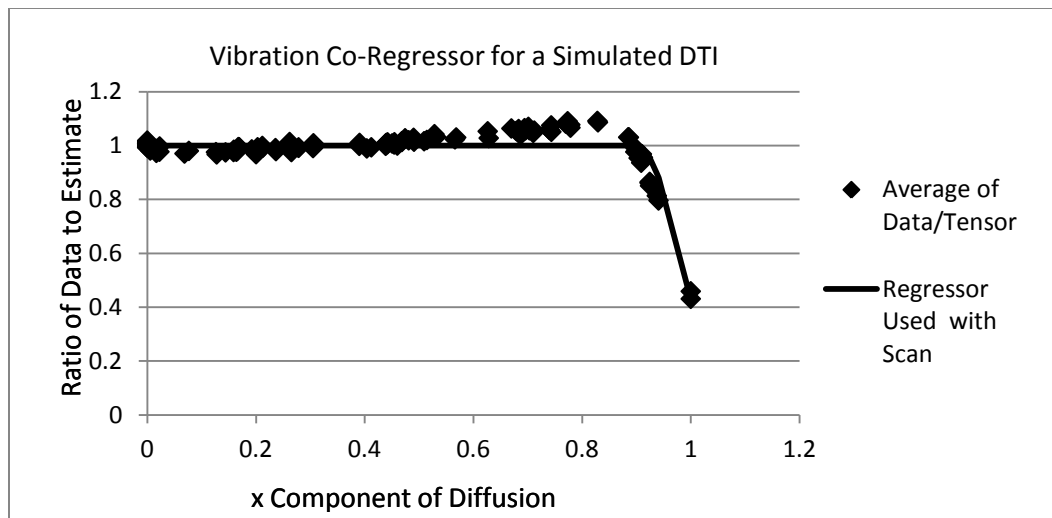


Figure 19. Vibration effect calculated from the simulated DTI scan: Data were collected from the simulated DTI scan in an ROI of vibration artifacts. The expected values were calculated from tensors derived with the RESTORE algorithm and ratios of the actual data to the estimated were compiled. The line plots the co-regressor that was calculated for use with the DTIFIT algorithm.

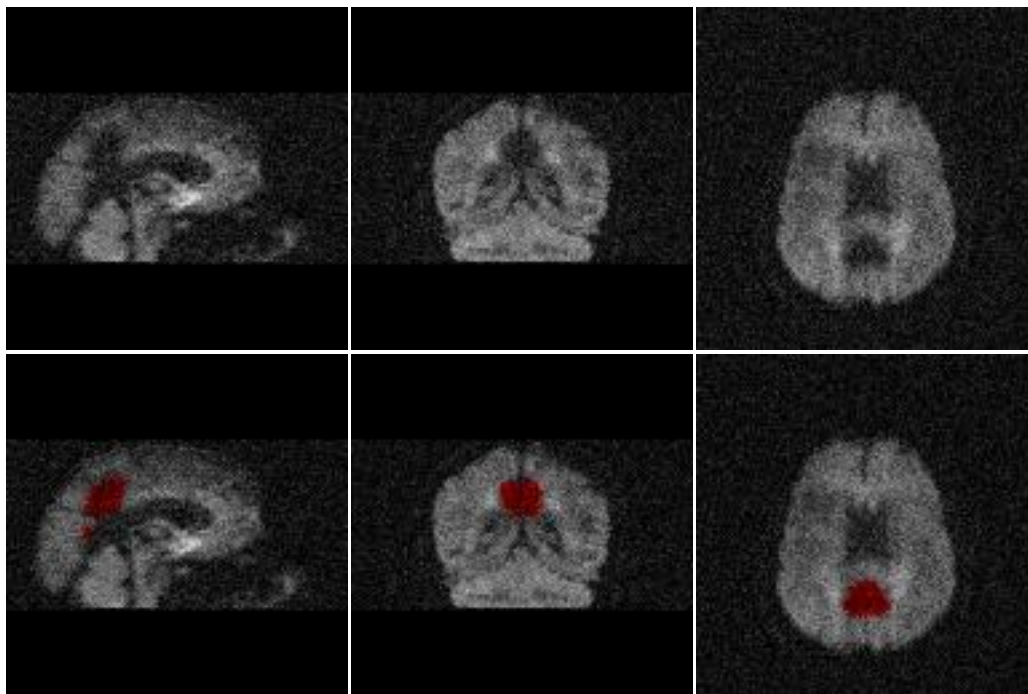


Figure 20. Vibration artifact detection for simulated image: The upper panels are slices from the simulated volume exhibiting the vibration artifact. In the lower panels the mask of the detected vibration artifact ROI is overlaid on the images in red.

The parameters used with Equation 13 to define the vibration artifact co-regressor for the whole head DTI scans for the GWIS subjects are given in Table 8. Co-regressors were calculated for 5 subjects from the national sample and 27 subjects from the Seabees. The parameters for the other subjects were outside the valid range defined in Section 3.3.2 and so those subjects are assumed not to exhibit the artifact. The co-regressors were used with the DTIFIT algorithm to generate masks for all GWIS scans exhibiting the vibration artifact. The data for Seabee GWS0018 are presented as an example. The co-regressor parameters were $a=0.87$ and $b=0.26$. Plots of the co-regressor and the data used to design it are given in Figure 21. In Figure 22, slices of the vibration mask calculated for Seabee GWS0018 are overlaid on the third volume of the DTI scan.

The third volume was acquired with a diffusion weighting of $b=1000 \text{ s/mm}^2$ and direction $[x,y,z]=[1,0,0]$.

Table 8. Coefficients for Vibration Artifact Co-regressor in GWIS.

GWIS Subject	Parameter a	Parameter b	Percentage of brain affected by vibration
National Sample 23	0.92	0.19	0.01
National Sample 29	0.92	0.29	0.28
National Sample 41	0.70	0.69	0.02
National Sample 49	0.87	0.90	0.62
National Sample 54	0.91	0.22	0.00
Seabee 06	0.83	0.64	0.09
Seabee 11	0.84	0.39	0.15
Seabee 12	0.66	1.25	0.37
Seabee 13	0.78	0.59	0.53
Seabee 14	0.84	0.49	0.01
Seabee 15	0.83	0.35	0.03
Seabee 18	0.87	0.26	0.01
Seabee 19	0.84	0.34	0.41
Seabee 21	0.88	0.38	0.13
Seabee 24	0.84	0.45	0.64
Seabee 26	0.72	1.10	0.12
Seabee 27	0.78	0.64	0.37
Seabee 29	0.86	0.31	0.18
Seabee 30	0.62	1.24	0.42
Seabee 31	0.81	0.83	0.04
Seabee 32	0.86	0.51	0.70
Seabee 33	0.85	0.56	0.37
Seabee 34	0.75	0.75	0.09
Seabee 35	0.90	0.48	0.65
Seabee 37	0.65	0.86	0.04
Seabee 38	0.84	0.46	0.34
Seabee 40	0.87	0.37	0.10
Seabee 41	0.74	0.90	0.07
Seabee 42	0.88	0.51	0.31
Seabee 46	0.82	0.62	0.01
Seabee 47	0.87	0.31	0.28
Seabee 49	0.93	0.34	0.02

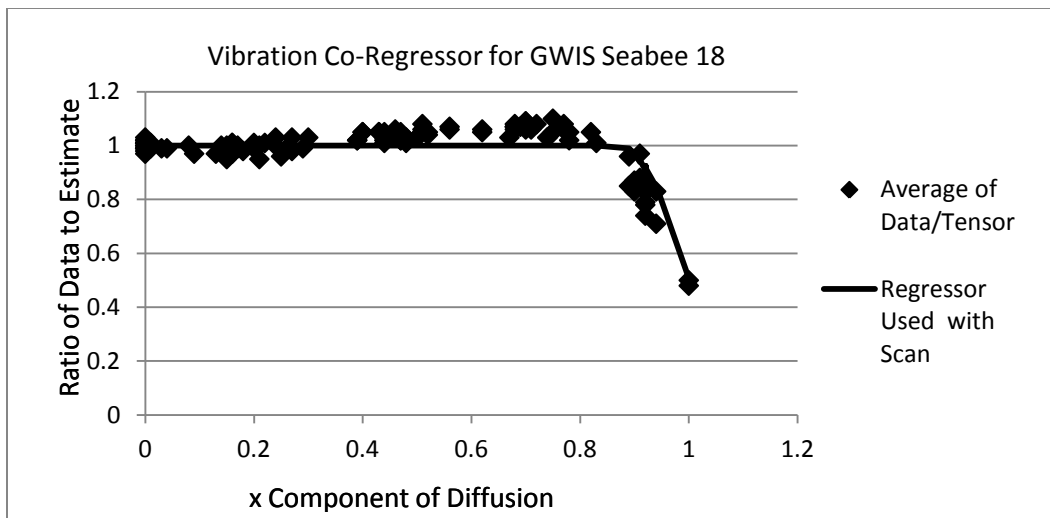


Figure 21. Vibration effect calculated from the GWIS DTI scan for Seabee GWS0018: Data were collected from the GWIS DTI scan in an ROI of vibration artifacts. The expected values were calculated from tensors derived with the RESTORE algorithm and ratios of the actual data to the estimated were compiled. The line plots the co-regressor that was calculated for use with the DTIFIT algorithm.

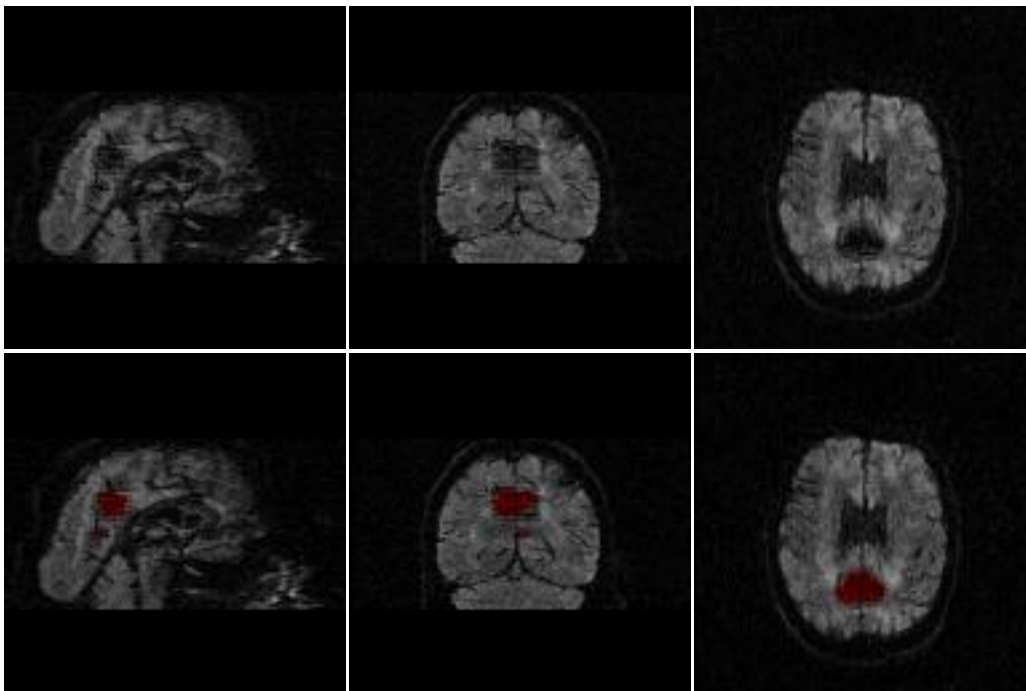


Figure 22. Vibration artifact detection for GWIS Seabee GWS0018: The upper panels are slices from a GWIS DTI scan exhibiting the vibration artifact. In the lower panels the mask of the detected vibration artifact ROI is overlaid on the images in red.

The locations of the vibration artifacts from all 32 subjects having the artifact are depicted in Figure 23. The vibration artifacts masks were co-registered to the average T1 weighted brain provided with the FSL software. The sum of all the masks are overlaid on the average T1 weighted image. The regions most affected by vibration-induced signal void artifacts were the medial parietal lobes, the region near the pituitary, and the inferior edge of the temporal lobes. The detected vibration-induced artifacts in the region of the pituitary were mostly outside the parenchyma of the brain. The detected artifacts in the medial parietal lobes were generally near boundaries between cortex and CSF, particularly boundaries that ran left to right. The detected artifacts at the inferior edges of

the temporal lobes also were near boundaries between cortex and CSF.

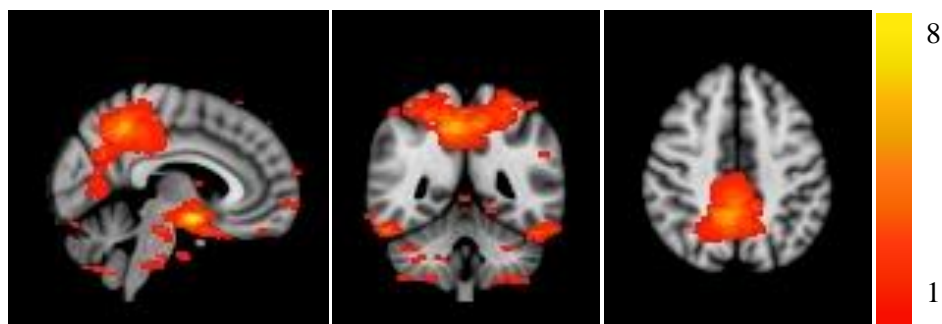


Figure 23. Location of vibration artifacts on standard brain: The underlays are sagittal, coronal and axial slices of the standard T1 weighted image supplied with FSL. The color overlay indicates the number of GWIS subjects that had vibration artifacts at a given voxel location. The legend on the right indicates the color scale.

The small-FOV DTI scans did not have clear visual evidence of vibration artifacts. The masks that were automatically produced did not appear to correspond to artifacts, but had many small ROIs scattered throughout the brain. Since the vibration artifact generally appears anatomically beyond the FOV acquired for the small-FOV scans and because no clear vibration artifacts were observed, the decision was made to not correct for vibration artifacts in the small-FOV DTI scans of the GWIS.

4.2.2 Detection of artifacts other than vibration artifacts for simulated data

The visual evaluation of the slices of the simulated DTI scan used to generate Table 7 was used to categorize the slices which were flagged for signal void artifacts at seven levels of detection sensitivity. The results are presented in Table 9. The slices flagged when a threshold of 10 was used are reported in the first row; subsequent rows report slices flagged at successively lower (more sensitive) thresholds. Of the 8 slices visually detected to have motion-induced signal void artifacts and reported in Table 7, 7

were flagged using the least sensitive threshold of 10. One of the motion-induced signal void artifacts was not flagged even with the most sensitive threshold of 4. That motion-induced artifact was near the vertex of the brain (slice 58). Of the 75 slices visually detected to have cardiac-induced signal void artifacts, 71 were flagged using a threshold of 5. Three of these slices were not flagged even with the most sensitive threshold of 4. These artifacts were all located in the three most inferior axial slices. One slice exhibiting the cardiac artifact was flagged at the threshold of 4 but not at higher thresholds. This instance of the cardiac artifact was visually more subtle than the other cardiac artifacts which were in slices flagged using a threshold of 5. Of the 62 slices that were visually assessed as exhibiting blurring, 13 were flagged when using a threshold of 4.

All slices flagged using a threshold of 6 or greater exhibited visually apparent artifacts. The 4 new slices flagged at a threshold of 5 included one slice (25%) that had no visually apparent artifacts, whereas the 10 new slices flagged at a threshold of 4 included 7 slices (70%) with no visually apparent artifacts.

The threshold selected for removing slices from further processing for the simulated data was 5. At this threshold level, the algorithm detected 7/8 (88%) of the motion-induced signal void artifacts and 71/75 (95%) of the cardiac-induced signal void artifacts. At the next lower threshold of 4, 7/10 (70%) of newly flagged slices exhibited no visually apparent artifacts.

The largest number of diffusion weighted volumes flagged for any one slice was 16 out of 100 for slice 9. These volumes were flagged primarily because of cardiac pulsation artifacts. Of the 50 slices unaffected by the simulated cardiac pulsation, 11 slices had two volumes flagged for signal void artifacts and 15 slices had one volume

flagged. The vibration artifact affected 12 out of 100 diffusion weighted volumes of the simulated DTI scan as determined by which diffusion weighting directions had an x component greater than parameter a of Equation 13. The vibration artifact mask described in Section 3.3.2 covered 0.87% of the total brain volume. Using the selected threshold value of 5, 92 of the 6400 diffusion weighted slices (1.4%) were removed from the simulated data for cardiac-induced or motion-induced signal void artifacts.

Table 9. Visual evaluation of flagged slices for simulated DTI scan

Threshold	# New Slices ^a	# Motion-Induced Artifacts ^b	# Cardiac-Induced Artifact	No Artifact
10	62	13 ^c	49	0
9	3	0	3	0
8	11 ^d	1	9	0
7	4	0	4	0
6	8	3	5	0
5	4	2	1	1
4	10 ^e	1	1	7

^a The slices flagged when a threshold of 10 was used are reported in the first row; subsequent rows report slices flagged at successively lower (more sensitive) thresholds.

^b Slices with motion-induced artifacts include the slices identified in Table 7 as having motion-induced signal void or motion-induced image blurring.

^c Seven of these 13 slices had motion-induced signal void artifacts. All other artifacts reported in this column were from motion-induced image blurring.

^d One slice detected at threshold 8 had subtle vibration artifact.

^e One slice detected at threshold 4 had subtle vibration artifact.

4.2.3 Detection of artifacts other than vibration artifacts for whole head FOV data

The results of visual evaluation of the flagged slices for the whole head FOV GWIS DTI scans are presented in Table 10. The slices flagged when a threshold of 10 was used are reported in the first row; subsequent rows report slices flagged at

successively lower (more sensitive) thresholds. All slices flagged using a threshold level of 6 or greater were reviewed visually. About 10% of the additional slices flagged at a threshold of 4 were selected randomly for visual review. During visual evaluation, many slices were found to have subtle artifacts which could not be clearly identified as a motion-induced or cardiac-induced artifact. These slices are recorded as having been flagged, but their artifact is not counted. As seen in Table 10, the visual evaluation of the flagged slices did not find any motion-induced artifacts below the threshold of 6. Very few cardiac-induced artifacts were seen below the threshold of 6. (~1% of slices flagged using a threshold of 4 but not flagged when using a threshold of 6 were visually evaluated as having cardiac-induced artifacts.) The percentage of slices flagged using a threshold of 5 but not flagged using a threshold of 6 which exhibited no visually discernable artifacts was 43%. Based on the fact that no motion-induced signal void artifacts were detected below the threshold of 6, the threshold for automatic signal void detection for the GWIS whole head FOV DTI scans was set at 6. The decrease in the percentage of cardiac-induced artifacts flagged and the increase in the percentage of flagged slices with no apparent artifacts confirm the selection of 6 as the threshold.

Table 10. Visual evaluation of flagged slices for whole head FOV GWIS DTI scans

Threshold	# New Slices ^a	# Motion-Induced Artifacts	# Cardiac-Induced Artifact	No Artifact ^b
10	246	66(27%)	44(18%)	4(2%)
9	63	5(8%)	9(14%)	4(6%)
8	81	1(1%)	21(26%)	6(7%)
7	138	2(1%)	27(20%)	21(15%)
6	286	3(1%)	41(14%)	74(26%)
5	543 ^c	0(0%)	1(1%)	29(43%)
4	1475 ^d	0(0%)	2(1%)	101(58%)

^a The slices flagged when a threshold of 10 was used are reported in the first row; subsequent rows report slices flagged at successively lower (more sensitive) thresholds.

^b During visual evaluation many slices were found to have subtle artifacts which could not be clearly identified as a motion-induced or cardiac-induced artifact. These slices are recorded as having been flagged, but their artifact is not counted.

^c Only 68 randomly selected slices of the 543 flagged slices were evaluated

^d Only 174 randomly selected slices of the 1475 flagged slices were evaluated

The largest number of volumes flagged for any one slice was 15 for slice 3 of subject 73 (GWN0073) from the national sample. These volumes were flagged primarily because of cardiac pulsation artifacts. After removing these 15 volumes, 85 diffusion weighted volumes were still available for calculating the diffusion tensors. There were 64 slices collected for each volume for 147 GWIS whole head FOV DTI scans and 60 slices for each volume for one GWIS whole head FOV DTI scan. For each subject receiving a DTI scan, 100 diffusion weighted volumes were collected making a total of 14,800 diffusion weighted volumes. The total number of slices for all subjects for which diffusion tensors were calculated was 9468, and the total number of slices collected for all diffusion weighted volumes and all subjects was 946,800. Artifacts were flagged in 814 slices in 453 different volumes of 98 different subjects, which was 0.09% of all

diffusion weighted slices in all volumes and subjects, 3.1% of all volumes and 66% of all subjects. Each flagged slice may affect more than one slice in the diffusion tensor maps because of the transform to correct for eddy current effects and subject motion. The number of diffusion tensor slices affected was 1496, which was 16% of the total.

The percentage of diffusion weighted slices acquired from the Seabees which were flagged for artifacts was 0.13% (451 of 345,200). The percentage of diffusion weighted slices acquired from the national sample which were flagged for artifacts was 0.06% (363 of 601,600).

4.2.4 Detection of artifacts other than vibration artifacts for small-FOV data

The results of visual evaluation of the flagged slices for the small-FOV GWIS DTI scans are presented in Table 11. The slices flagged when a threshold of 10 was used are reported in the first row; subsequent rows report slices flagged at successively lower (more sensitive) thresholds. All slices flagged using a threshold level of 6 or greater were reviewed visually. About 10% of the additional slices flagged at a threshold of 4 were selected randomly for visual review. During visual evaluation, many slices were found to have subtle artifacts which could not be clearly identified as a motion-induced or cardiac-induced artifact. These slices are recorded as having been flagged, but their artifact is not counted. As seen in Table 11, the visual evaluation of the flagged slices did not find any motion-induced artifacts below the threshold of 5. Very few cardiac-induced artifacts were seen below the threshold of 5. (~6% of slices flagged using a threshold of 4 but not flagged when using a threshold of 5 were visually evaluated as having cardiac-induced artifacts.) The percentage of slices flagged using a threshold of 4 but not flagged using a

threshold of 5 which exhibited no visually discernable artifacts was 54%. Based on the fact that no motion-induced signal void artifacts were detected below the threshold of 5, the threshold for automatic signal void detection for the GWIS small-FOV DTI scans was set at 5. The decrease in the percentage of cardiac-induced artifacts flagged and the increase in the percentage of flagged slices with no apparent artifacts confirm the selection of 5 as the threshold.

Table 11. Visual evaluation of flagged slices for small-FOV GWIS DTI scans

Threshold	# New Slices ^a	# Motion-Induced Artifacts	# Cardiac-Induced Artifact	No Artifact ^b
10	200	69(35%)	7(4%)	15(8%)
9	73	5(7%)	7(10%)	9(12%)
8	86	9(10%)	11(13%)	11(13%)
7	161	12(7%)	27(17%)	29(18%)
6	269	6(2%)	28(10%)	80(30%)
5	552 ^c	2(4%)	12(23%)	16(30%)
4	1489 ^d	0(0%)	8(6%)	75(54%)

^a The slices flagged when a threshold of 10 was used are reported in the first row; subsequent rows report slices flagged at successively lower (more sensitive) thresholds.

^b During visual evaluation many slices were found to have subtle artifacts which could not be clearly identified as a motion-induced or cardiac-induced artifact. These slices are recorded as having been flagged, but their artifact is not counted.

^c Only 53 randomly selected slices of the 552 flagged slices were evaluated

^d Only 140 randomly selected slices of the 1489 flagged slices were evaluated

The largest number of volumes flagged for any one slice was 32 for slice 23 of subject 57 (GWN0057) from the national sample. These volumes were very near the vertex of the brain and were flagged primarily because the co-registration of volumes to

correct for subject motion caused errors in the signal estimates for slices 23 and 24. After removing the 32 flagged volumes, 68 diffusion weighted volumes were still available for calculating the diffusion tensors. Slice 23 of subject GWN0057 had many more volumes excluded than any other slice from among the other subjects. The slice with the second most volumes removed was slice 2 of subject 26 (GWS0026) from the Seabees which had 21 volumes removed. These volumes were flagged primarily because of cardiac pulsation artifacts. After removing these 21 volumes, 79 diffusion weighted volumes were still available for calculating the diffusion tensors. There were 25 slices collected for each volume for 145 GWIS small-FOV DTI scans and 22 slices for each volume for two GWIS small-FOV DTI scans. For subjects receiving a DTI scan, 300 diffusion weighted volumes were collected for 140 DTI scans and 200 diffusion weighted volumes were collected for 7 DTI scans making a total of 43,400 diffusion weighted volumes. The total number of slices for all subjects for which diffusion tensors were calculated was 3669, and the total number of slices collected for all diffusion weighted volumes and all subjects was 1,083,200. Artifacts were flagged in 1341 slices in 733 different volumes of 119 different subjects, which was 0.12% of all diffusion weighted slices in all volumes and subjects, 1.7% of all volumes and 81% of all subjects. Each flagged slice may affect more than one slice in the diffusion tensor maps because of the transform to correct for eddy current effects and subject motion. The number of diffusion tensor slices affected was 1347, which was 37% of the total.

The percentage of diffusion weighted slices acquired from the Seabees which were flagged for artifacts was 0.18% (701 of 388,200). The percentage of diffusion weighted slices acquired from the national sample which were flagged for artifacts was

0.09% (640 of 695,000).

4.2.5 Additional artifacts detected while searching for signal void artifacts

The evaluation of many flagged slices is not reported in Table 10 or Table 11. The total number of whole head FOV slices that were removed was 814 but 486 of those slices had artifacts that were other than the types of artifacts reported in Table 10. For the small-FOV scans, the total number of slices that were removed was 1341 but an estimated 703 of those slices had artifacts that were other than the types of artifacts reported in Table 11. Many of the “artifacts” not included in Table 10 and Table 11 were simply too subtle to be clearly identified as artifacts. Some of these had regions that were slightly darker than expected but the possibility that those regions reflected accurate data could not be ruled out. The reason for some of the slices being flagged was clear even though they were not categorized as signal void artifacts. These reasons included intra-volume motion which caused parts of a volume to be misregistered with itself, vibration artifacts that were not accounted for by the vibration mask, and artifacts from sources not included in the above discussion.

Two of the artifacts not discussed above are presented in Figure 24. The first artifact, which is presented in the left-hand panel of Figure 24, is characterized by dark lines in the phase encoding direction. The origin of this artifact, which was observed in 8 slices of the GWIS whole head FOV DTI scans, has not been determined. The second artifact, which is presented in the right-hand panel of Figure 24, is characterized by the superposition of a periodic variation of intensity on the image. Sharp noise spikes at the

time of acquisition of the k-space signal introduce artificial periodic intensity variations into the reconstructed image. At the time this image was acquired there was a problem with the z gradient cable which introduced noise spikes in the k-space signal. Three slices of the GWIS whole head FOV DTI scans that were flagged by the signal void artifact detection algorithm exhibited periodic intensity variation when the threshold was set to 4. The slices presented in Figure 24 were both flagged and excluded from the tensor calculations by the methods presented here. All 8 slices observed to have the black line artifacts were removed as were two slices which had periodic intensity variations.

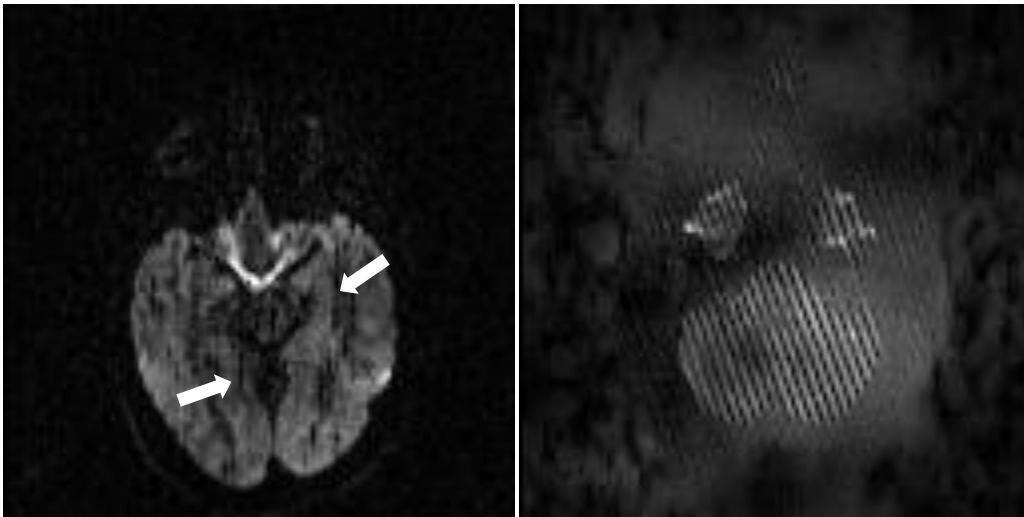


Figure 24. Two artifacts observed in GWIS DTI data: The image on the left exhibits the artifact of dark lines indicated with white arrows. The image on the right exhibits the artifact of a superimposed periodic spatial variation.

4.3 Removal of Signal Void Artifacts

4.3.1 Simulation Data

The diffusion tensors for the simulated DTI scan were calculated after excluding data affected by artifacts as discussed in Section 3.4 using the method discussed in Section 3.5. The effect on FA of excluding the affected volumes for slice 9 is presented visually in Figure 25.

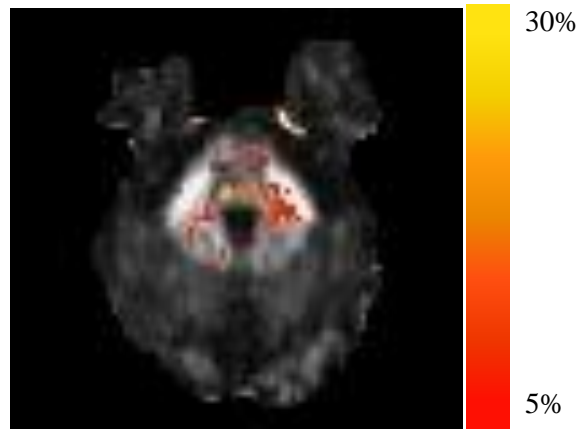


Figure 25. Impact of artifact removal on simulation FA: An FA map for the simulated DTI scan with artifacts is overlaid to indicate voxels strongly affected by removing signal void artifacts. FA was calculated before and after removing volumes containing artifacts. The color overlay indicates the percent change in FA for voxels with change $>5\%$ and $FA > 0.4$. The legend on the right indicates the color scale. The greatest FA change was 37.7 %.

The maximum difference in FA between the original tensors (that is, the tensors used to simulate the DTI scan) and the tensors calculated from the simulated DTI scan was 0.29 for slice 9 which had 519 voxels in the mask of voxels being tested for that slice. The averages of the maximum differences between the FA of the three simulations and the FA of the original tensors for the 47 slices that had signal void artifacts flagged

are given in Table 12. The maximum FA differences between the simulations and the original tensors are significantly different from 0 in each case. The averages of the paired differences between the three simulations of the maximum deviation of the FA of the simulation from the FA of the original tensors are given in Table 13. The maximum FA deviations from the original tensors were significantly greater for the simulation with signal void artifacts than for the baseline simulation. The FA deviations from the original tensors were also significantly greater for the simulation with signal void artifacts than for the simulation with flagged data removed. However, the FA deviations from the original tensors were not significantly different between the simulation with flagged data removed and the baseline simulation.

Table 12: Maximum FA differences Between Simulations and Original Tensors

Simulation	Mean	Min	Max	Standard Deviation	P value
Baseline	0.26	0.21	0.36	0.04	$<<10^{-10}$
With Artifacts	0.27	0.21	0.40	0.04	$<<10^{-10}$
Artifacts Removed	0.26	0.21	0.36	0.04	$<<10^{-10}$

Table 13: Comparisons of FA Deviation from Original Between Simulations

Comparison	Mean	Min	Max	Standard Deviation	P value
Artifacts minus Baseline	0.006	-0.048	0.036	0.014	0.003
Artifacts Removed minus Baseline	0.001	-0.025	0.040	0.010	0.18
Artifact minus Artifacts Removed	0.007	-0.012	0.057	0.012	0.0001

4.3.2 GWIS Whole Head FOV DTI Data

The GWIS whole head FOV DTI scan of the 45th subject of the national sample (GWN0045) was used to visualize the difference in the FA maps when signal void was present in the data compared to when it had been removed. During the 83rd volume of the scan, the subject apparently moved his head as indicated by the signal void artifacts in slices 38 and 40. Head motion around this time was confirmed by reviewing the affine transforms used to co-register the volumes. Rotation and translation parameters of the affine matrices used to register volumes 82, 83, and 84 to the first volume of the DTI scan are presented in Table 14. Between volumes 82 and 83, there were translations of the head in the superior direction of about 2.5 mm and in the posterior direction of about 1.2 mm; between volumes 83 and 84, there was also a rotation about the x axis of about 0.7°. DTIFIT for slice 39 was run once using all 112 volumes of the DTI scan and once using the remaining 111 volumes after volume 83 was removed. (Co-registration of the diffusion weighted volumes to the first b=0 image caused slices 38 and 40 of volume 83 to affect slice 39 of the tensor map.) Figure 26 presents slice 39 of the FA map calculated from the whole head FOV DTI scan of GWN0045 overlaid with a mask of the voxels where FA changed by more than 5% for FA greater than 0.4. The relevance of using a threshold of 5% was supported by the fact that significant differences in FA of a preliminary TBSS analysis differed by that amount.

Table 14. Rotation angles and translation distances for volumes in National Sample Subject GWN0045.

Volume	Ω_z (°)	Ω_x (°)	Ω_y (°)	I-S (mm)	R-L (mm)	A-P (mm)
Vol82	-0.22	-0.61	-0.33	0.09	-0.78	0.43
Vol83	-0.19	-0.57	-0.13	2.56	-0.82	1.61
Vol84	-0.24	-1.26	-0.44	1.83	-0.74	-0.19

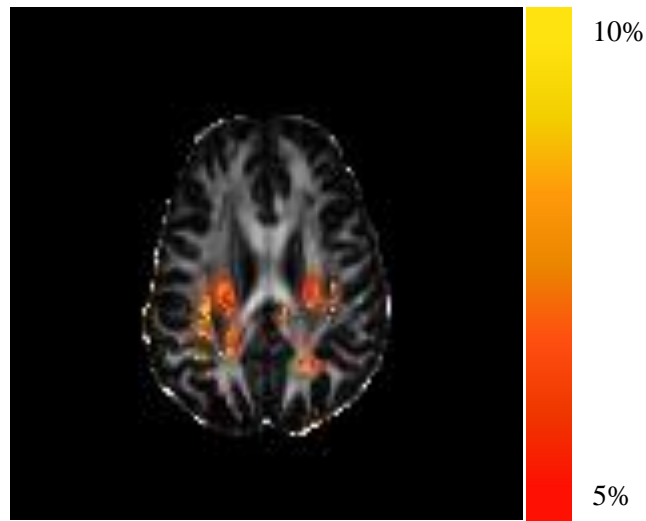


Figure 26. Impact of artifact removal on FA from the GWIS whole head FOV DTI scan from subject GWN0045: The FA map for the DTI scan is overlaid to indicate voxels strongly affected by signal void artifact. FA was calculated both including and excluding volume 83 which contained the artifact. The color overlay indicates the percent change in FA for voxels with change >5% and FA >0.4. The legend on the right indicates the color scale. The greatest FA change was 10.3%.

The averages of the maximum changes in FA caused by removing data flagged for artifacts are listed in Appendix J for the whole head FOV DTI scans for GWIS subjects. The averages of the maximum changes in FA caused by removing data from alternate volumes to those which were flagged are also listed in Appendix J. The averages

and standard deviations of the differences used in the paired t test comparing the FA changes for removing artifacts to the FA changes for removing alternate volumes are given in Appendix J as are the p values at which the one tailed comparison would be significant. Of the 98 subjects with data flagged for removal, 65 had significantly larger differences ($p \leq 0.05$) when the flagged data was removed as opposed to when alternate data was removed. There were 8 subjects for which the differences were larger when the alternate data was removed. Had a two tailed t test ($p \leq 0.05$) been performed to detect differences in either direction, 2 of these would have been flagged as significant. The t test using all adjusted slices for the comparison indicated that the FA changes which occurred with removing flagged data were significantly greater than the FA changes when removing alternate data by an amount of 0.01 with a p value $< 10^{-10}$.

4.3.3 GWIS Small-FOV DTI Data

The averages of the maximum changes in FA caused by removing data flagged for artifacts are listed in Appendix K for the small-FOV DTI scans for GWIS subjects. The averages of the maximum changes in FA caused by removing data from alternate volumes to those which were flagged are also listed in Appendix K. The averages and standard deviations of the differences used in the paired t test comparing the FA changes for removing artifacts to the FA changes for removing alternate volumes are given in Appendix K as are the p values at which the one tailed comparison would be significant. Of the 119 subjects with data flagged for removal, 105 had significantly larger differences ($p \leq 0.05$) when the flagged data was removed as opposed to when alternate data was removed. There were 6 subjects for which the differences were larger when the

alternate data was removed. Had a two tailed t test ($p \leq 0.05$) been performed to detect differences in either direction, none of these would have been flagged as significant. The t test using all adjusted slices for the comparison indicated that the FA changes which occurred with removing flagged data were significantly greater than the FA changes when removing alternate data by an amount of 0.0005 with a p value < 0.025 .

4.4 Aliased Signal Masks for Mean FA Maps

Aliased signal in the small-FOV DTI scans did not corrupt the FA maps in the regions of the brainstem for any of the subjects of the GWIS. The extent of the regions affected by aliased signal in the two populations of the GWIS is depicted in Figure 27 as a red mask overlaying the mean FA. The image on the left is the mean FA for all Seabees that was calculated using the small-FOV DTI scans. The aliased signal masks for all the small-FOV DTI scans collected from the Seabees are combined in the red mask to show all areas where aliased signal from at least one scan is present. The image on the right shows the extent of aliased signal for the small-FOV DTI scans of the national sample.

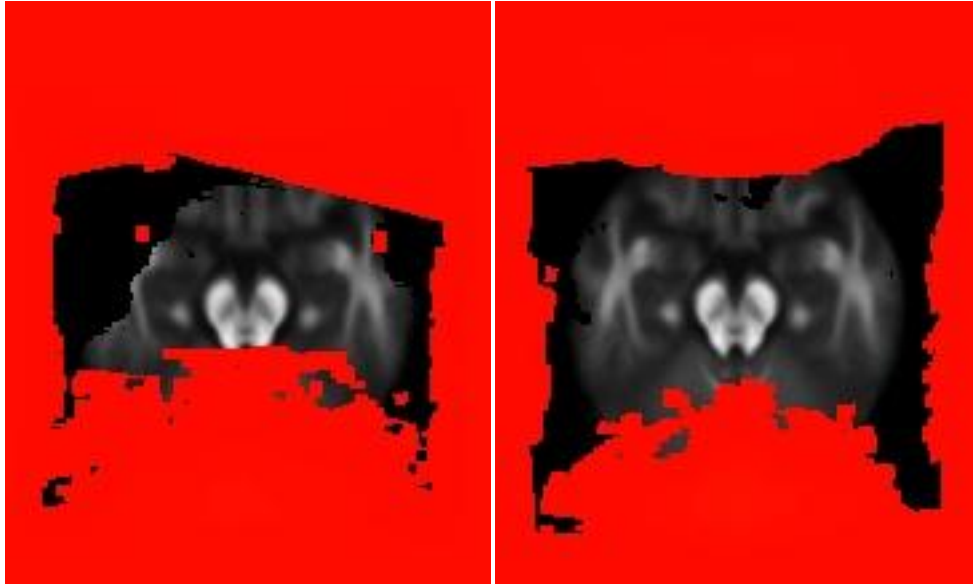


Figure 27. Region of small-FOV mean FA maps unaffected by aliased signal: The image on the left is the mean FA for all Seabees subjects of the GWIS. The aliased signal mask in red indicates all voxels which included potentially aliased signal for the small-FOV DTI Seabees scans. The image on the right is the mean FA for all national sample subjects. The aliased signal masks from the subjects of each study were co-registered using the linear portion of the TBSS registration.

4.5 Registration of FA Maps for Small-FOV DTI Scans

The FA map for subject GWS0009 of the GWIS was poorly registered using the unmodified TBSS algorithm. The modification described in Section 3.7 was applied and the results for subject GWS0009 are presented in Figure 28. The unmodified registration caused the corpus callosum to be stretched in the superior direction beyond the FOV of the original image acquisition. The mask that was applied was a combination of the brain mask generated by the BET algorithm of FSL and the aliased signal mask described in Section 3.6. Although the more obvious error along the superior boundary

was removed, the body of the corpus callosum appears to be missing compared to the target image.

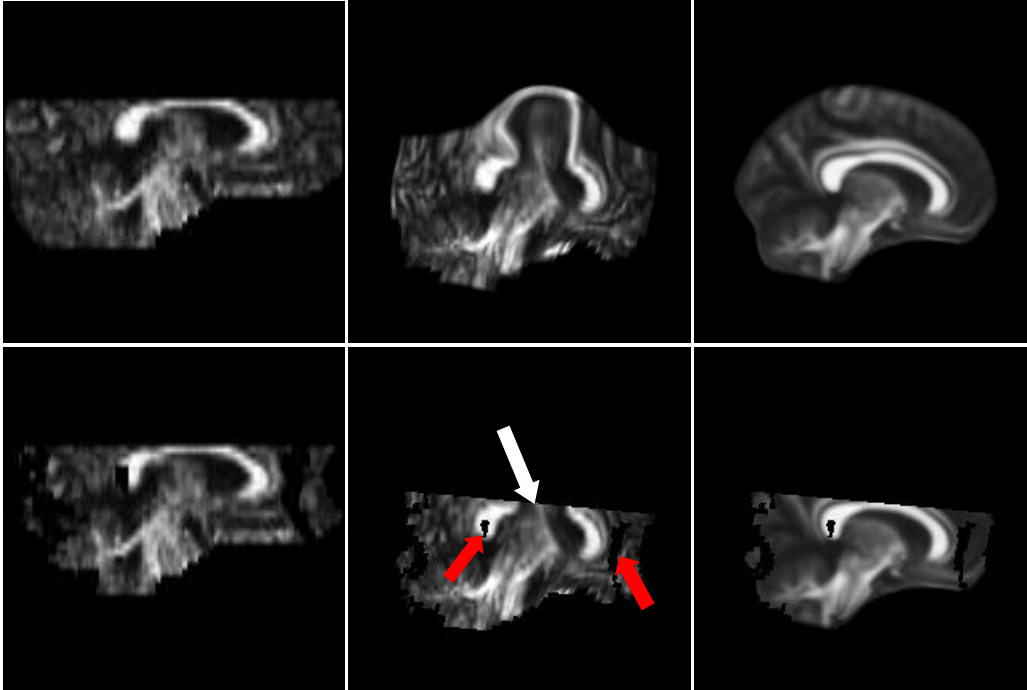


Figure 28. Registration errors in non-linear registration of FA maps from small-FOV DTI data: The image in the upper left is a sagittal slice of the FA map for the small-FOV DTI scan from subject GWS0009 of the GWIS. The image on the center top is the same image after non-linear registration performed by the TBSS algorithm. The image in the upper right is the target for the non-linear registration. The lower images are the same as the upper images but with the brain and aliased signal masks applied after appropriate linear transforms. The white arrow in the lower middle panel indicates the region of misregistration in the corpus callosum. The red arrows indicate regions eliminated by application of the aliased signal mask.

An additional error in the TBSS registration was detected in five subjects of the GWIS. The initial linear transform performed by the TBSS algorithm occasionally failed to provide an accurate starting point for the non-linear registration. The linear transformation had to be adjusted for five subjects. This was accomplished by including

the “-usesqform” parameter for the linear registration portion of the TBSS algorithm. The “-usesqform” parameter causes the FLIRT algorithm used by TBSS to initialize the registration search using information contained in the image header. The linear registration portion of the TBSS algorithm performed poorly for subject GWS0007 of the GWIS. A coronal slice of the incorrectly registered FA map and the corresponding slice of the FA map after correcting the registration are presented in Figure 29. With these adjustments, a visual inspection of the registered FA maps indicated that the TBSS registration was completed successfully.

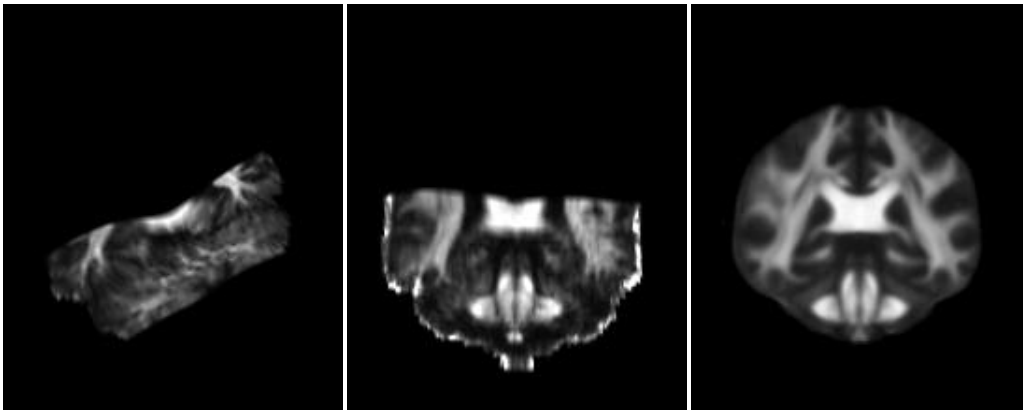


Figure 29. Registration error in linear registration of the FA map from small-FOV DTI data of subject GWS0007: The image on the left is a coronal slice of an FA map after non-linear registration using the TBSS algorithm. The image in the center is the result when the “-usesqform” parameter was used with the linear registration portion of TBSS. The FA map on the right is a coronal slice of the target that was used for the registration.

4.6 Results for Gulf War Illness Study DTI Group Analysis

After removing diffusion weighted data with signal void artifacts and masking out voxels with potentially aliased signal from the small-FOV scans, TBSS analysis was

conducted on the FA maps from the GWIS. Two axial slices (one from the whole head FOV scans and one from the small-FOV scans) of the skeletonised white matter tracts used by TBSS in the white matter co-registration process are presented for the Seabees data in Figure 30.

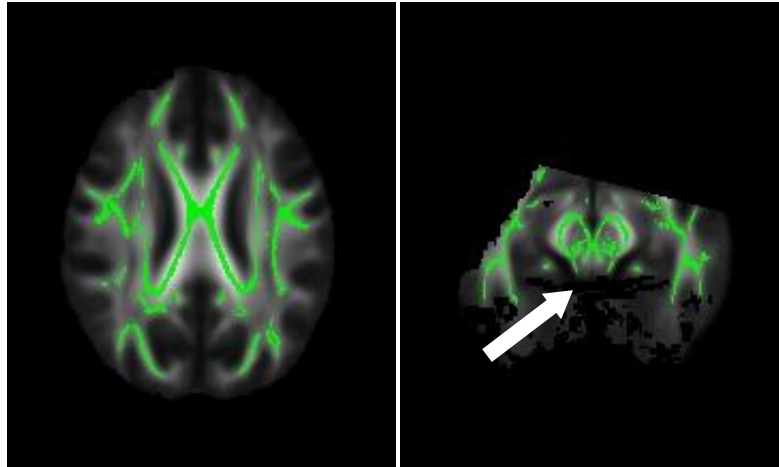


Figure 30. Skeletonised masks of white matter tracts: The images presented here are single axial slices of the mean FA generated by TBSS for the Seabees subjects in the GWIS with the mask of skeletonised white matter tracts overlaid in green. The image on the left is from the whole head FOV DTI scans and the image on the right is from the small-FOV DTI scans. A mask has been applied to the mean FA for the small-FOV scans to remove regions that are contaminated with aliased signal. The white arrow in the right panel indicates a region that has been removed due to aliased signal.

The tests between the deployed and non-deployed control groups failed to detect any differences at a p value threshold of 0.05. Tests between the national sample subjects with Syndrome 2 only and national sample subjects with Syndrome 2 and Syndrome 4 failed to detect any differences at a p value threshold of 0.05. These results were consistent between the tests of the whole head FOV DTI scans and those of the small-FOV DTI scans. The minimum p values for differences between these groups are given in Table 15. The deployed controls and the non-deployed controls were treated as a

single control group for subsequent analysis. Also, the subjects with both Syndrome 2 and Syndrome 4 were grouped together with the subjects that had only Syndrome 2 symptoms.

Table 15. Minimum p values for significance of FA differences between Sub-Groups

Study Group	FOV ^a	Comparison ^b	Minimum p value for FA comparisons
Seabees	WH	DC > NDC	0.55
Seabees	WH	NDC > DC	0.89
Seabees	PH	DC > NDC	0.17
Seabees	PH	NDC > DC	0.79
National Sample	WH	DC > NDC	0.40
National Sample	WH	NDC > DC	0.40
National Sample	PH	DC > NDC	0.25
National Sample	PH	NDC > DC	0.46
National Sample	WH	Syn2.4 > Syn2	0.34
National Sample	WH	Syn2 > Syn2.4	0.86
National Sample	PH	Syn2.4 > Syn2	0.39
National Sample	PH	Syn2 > Syn2.4	0.97

^aWH indicates scans with the FOV that covers the whole head. PH indicates scans with the small-FOV that only partially covers the head.

^bDC indicates deployed controls, NDC indicates non-deployed controls, Syn2.4 indicates subjects with both syndrome 2 and syndrome 4, and Syn2 indicates subjects with syndrome 2 alone.

After pooling the deployed and non-deployed control groups, as well as establishing a single Syndrome 2 group, comparisons were made between the control group and each of the syndrome groups. The tests between the syndrome 2 group and the controls for the Seabees detected voxels with significantly greater FA for the controls than for the syndrome 2 subjects. This was true for both the whole head FOV data and the small-FOV data. Significance was detected using a p value of 0.05. The comparisons between the control groups and each of the other syndrome groups all failed to detect any

significant differences in FA. The white matter tracts for which the control group had greater FA than the syndrome 2 group were not limited to a single white matter tract or localized region of the brain. Two axial slices of the FA map (one from the whole head FOV scans and one from the small-FOV scans) with an overlay indicating voxels where the controls FA is greater than syndrome 2 FA are given in Figure 31. The minimum p values for the comparisons between the controls and the various syndrome groups are given in Table 16.

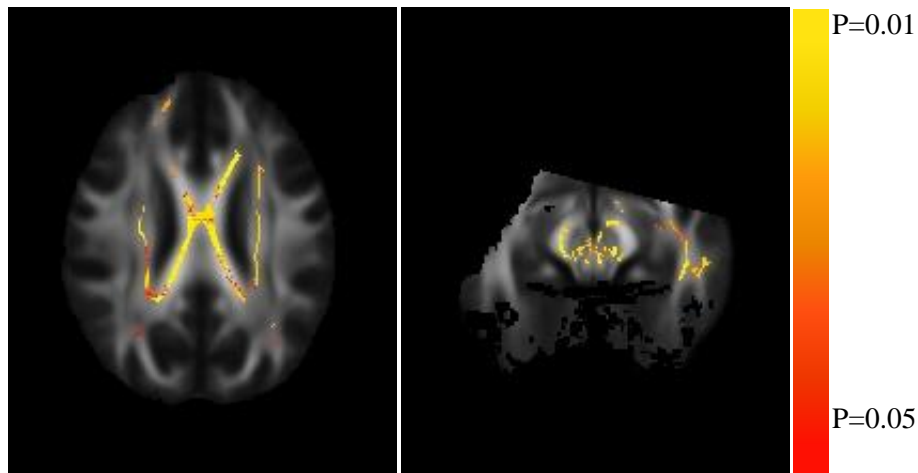


Figure 31. White matter tracts for which the control group had greater FA than the syndrome 2 group: On the left, the mean FA for an axial slice of the Seabees whole head FOV scans is overlaid with p values less than 0.05 for the comparison that the control FA is greater than syndrome 2 FA. On the right, the mean FA is given for an axial slice of the Seabees small-FOV scans with the corresponding overlay for those scans.

Table 16. Minimum p values for significance of FA differences between the controls and syndrome groups.

Study Group	FOV ^a	Comparison ^b	Minimum p value for FA comparisons
Seabees	WH	C > Syn1	0.35
Seabees	WH	Syn1 > C	0.49
Seabees	WH	C > Syn2	0.01
Seabees	WH	Syn2 > C	0.81
Seabees	WH	C > Syn3	0.46
Seabees	WH	Syn3 > C	0.39
Seabees	PH	C > Syn1	0.17
Seabees	PH	Syn1 > C	0.92
Seabees	PH	C > Syn2	0.01
Seabees	PH	Syn2 > C	1.00
Seabees	PH	C > Syn3	0.15
Seabees	PH	Syn3 > C	0.94
National Sample	WH	C > Syn1	0.12
National Sample	WH	Syn1 > C	0.38
National Sample	WH	C > Syn2	0.27
National Sample	WH	Syn2 > C	0.21
National Sample	WH	C > Syn3	0.07
National Sample	WH	Syn3 > C	0.89
National Sample	PH	C > Syn1	0.24
National Sample	PH	Syn1 > C	0.31
National Sample	PH	C > Syn2	0.62
National Sample	PH	Syn2 > C	0.13
National Sample	PH	C > Syn3	0.25
National Sample	PH	Syn3 > C	0.54

^aWH indicates scans with the FOV that covers the whole head. PH indicates scans with the small-FOV that only partially covers the head.

^bC indicates the group of deployed controls and non-deployed controls. Syn1, Syn2, and Syn3 indicate subjects in the three syndrome groups.

Comparisons between whole head FOV data and small-FOV data for each of the groups were conducted to determine if data from the different resolution scans could be pooled to increase the power of group analysis. These comparisons showed significant differences between the FA values derived from data collected at these resolutions. The FA of the whole head FOV data was greater than the FA of the small-FOV data at a p

value threshold of 0.05 for the control group and for each of the three syndrome groups. An axial slice of the FA map with an overlay indicating voxels where the Syndrome 2 FA for the whole head FOV scans of the Seabees is greater than the Syndrome 2 FA for the small-FOV scans of the Seabees is given in Figure 32. The minimum p values for the comparisons between the whole head FOV scans and the small-FOV scans for each syndrome group are given in Table 17. The whole head FOV data and the small-FOV data were not pooled for group analysis.

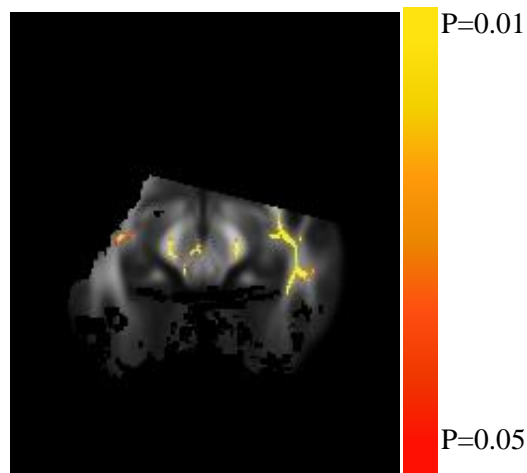


Figure 32. Comparison of FA from whole head FOV scans to FA from small-FOV scans: The mean FA for an axial slice of the Seabees small-FOV scans is overlaid with p values less than 0.05 for the comparison that the whole head FOV scans for the Syndrome 2 Seabees group had greater FA than the small-FOV scans for the Syndrome 2 Seabees group.

Table 17. Minimum p values for significance of FA differences between the whole head FOV scans and the small-FOV scans.

Study Group	Syndrome Group ^a	Comparison ^b	Minimum p value for FA comparisons
Seabees	C	WH > PH	0.001
Seabees	C	PH > WH	0.54
Seabees	Syn1	WH > PH	0.001
Seabees	Syn1	PH > WH	0.63
Seabees	Syn2	WH > PH	0.001
Seabees	Syn2	PH > WH	0.88
Seabees	Syn3	WH > PH	0.001
Seabees	Syn3	PH > WH	0.70
National Sample	C	WH > PH	0.001
National Sample	C	PH > WH	0.47
National Sample	Syn1	WH > PH	0.001
National Sample	Syn1	PH > WH	0.45
National Sample	Syn2	WH > PH	0.001
National Sample	Syn2	PH > WH	0.36
National Sample	Syn3	WH > PH	0.001
National Sample	Syn3	PH > WH	0.64

^aC indicates the group of deployed controls and non-deployed controls. Syn1, Syn2, and Syn3 indicate subjects in the three syndrome groups.

^bWH indicates scans with the FOV that covers the whole head. PH indicates scans with the small-FOV that only partially covers the head.

Comparisons between national sample data and the Seabees data were conducted to test whether the FA of the corresponding groups from the two cohorts were different. As discussed above, age was used as a covariate in the comparisons, but gender, PTSD and MDD were not included. A more thorough analysis of the GWIS data should consider these as possible confounding factors. The comparisons for the syndrome 2 groups showed significant differences for both the whole head and the small-FOV scans. The comparison between national sample data and the Seabees data for the control groups showed significant differences for the small-FOV scans. Axial slices of the whole head FOV and the small-FOV FA maps are given in Figure 33. The color overlays

indicate voxels where the Syndrome 2 FA for the national sample is greater than the Syndrome 2 FA for the Seabees. The minimum p values for the comparisons between the national sample and the Seabees for each syndrome group are given in Table 18.

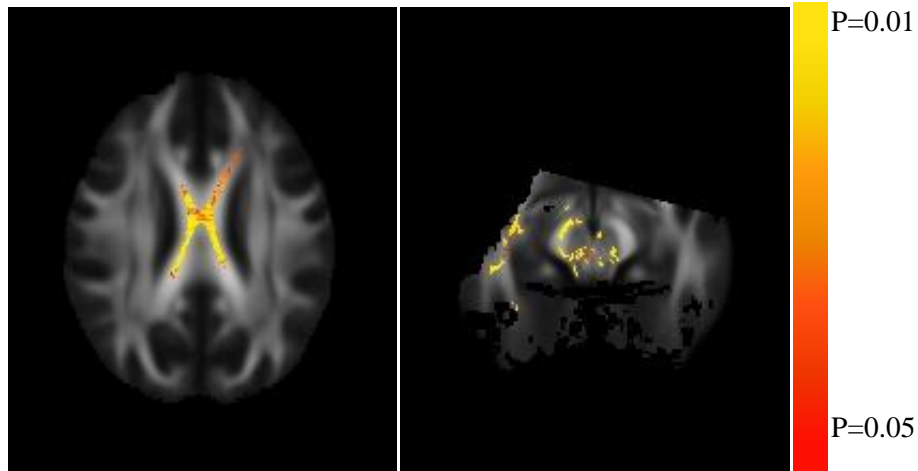


Figure 33. White matter tracts for which the national sample had greater FA than the Seabees for the syndrome 2 groups: On the left, the mean FA for an axial slice of the whole head FOV scans is overlaid with p values less than 0.05 for the comparison that the national sample syndrome 2 FA is greater than the Seabees syndrome 2 FA. On the right, the mean FA is given for an axial slice of the small-FOV scans with the corresponding overlay for those scans.

Table 18. Minimum p values for significance of FA differences between the national sample and the Seabees.

Syndrome Group ^a	FOV ^b	Comparison ^c	Minimum p value for FA comparisons
C	WH	Sea > Nat	0.13
C	WH	Nat > Sea	0.50
C	PH	Sea > Nat	0.05
C	PH	Nat > Sea	0.28
Syn1	WH	Sea > Nat	0.17
Syn1	WH	Nat > Sea	0.47
Syn1	PH	Sea > Nat	0.17
Syn1	PH	Nat > Sea	0.04
Syn2	WH	Sea > Nat	0.59
Syn2	WH	Nat > Sea	0.01
Syn2	PH	Sea > Nat	0.85
Syn2	PH	Nat > Sea	0.003
Syn3	WH	Sea > Nat	0.29
Syn3	WH	Nat > Sea	0.65
Syn3	PH	Sea > Nat	0.47
Syn3	PH	Nat > Sea	0.24

^aC indicates the group of deployed controls and non-deployed controls. Syn1, Syn2, and Syn3 indicate subjects in the three syndrome groups.

^bWH indicates scans with the FOV that covers the whole head. PH indicates scans with the small-FOV that only partially covers the head.

^cSea indicates scans from the Seabees. Nat indicates scans from the national sample.

Finally, the FA data derived without accounting for signal void artifacts were analyzed in the same way in which the adjusted data were analyzed. The minimum p values for the comparisons between the controls and the various syndrome groups are given in Table 19 for both adjusted data and unadjusted data. In both cases of removing the artifacts and of not removing the artifacts, the control group had significantly higher FA than the Syndrome 2 group for the Seabees at a p value threshold of 0.05. The majority of the voxels that had a significant difference in FA between controls and Syndrome 2 were the same for both cases. The numbers of voxels that were significant in only the adjusted data or only the unadjusted data are listed in Table 20. The voxels

unique to one case or the other were not in large clusters but were typically groups of four voxels or less. Figure 34 presents a slice of the FA map from the whole head FOV scans on the left and from the small-FOV scans on the right. The red mask indicates voxels which were significant when the data were adjusted but were not significant when the data were not adjusted. The blue mask indicates significant voxels which were unique to the unadjusted data.

Table 19. Minimum p values for significance of FA differences between the controls and syndrome groups when signal void was not removed.

Study Group	FOV ^a	Comparison ^b	Minimum p value for FA comparisons (adjusted)	Minimum p value for FA comparisons (unadjusted)
Seabees	WH	C > Syn1	0.35	0.36
Seabees	WH	Syn1 > C	0.49	0.52
Seabees	WH	C > Syn2	0.01	0.004
Seabees	WH	Syn2 > C	0.81	0.81
Seabees	WH	C > Syn3	0.46	0.44
Seabees	WH	Syn3 > C	0.39	0.42
Seabees	PH	C > Syn1	0.17	0.17
Seabees	PH	Syn1 > C	0.92	0.88
Seabees	PH	C > Syn2	0.01	0.004
Seabees	PH	Syn2 > C	1.00	1.000
Seabees	PH	C > Syn3	0.15	0.16
Seabees	PH	Syn3 > C	0.94	0.91
National Sample	WH	C > Syn1	0.12	0.13
National Sample	WH	Syn1 > C	0.38	0.38
National Sample	WH	C > Syn2	0.27	0.27
National Sample	WH	Syn2 > C	0.21	0.22
National Sample	WH	C > Syn3	0.07	0.07
National Sample	WH	Syn3 > C	0.89	0.88
National Sample	PH	C > Syn1	0.24	0.25
National Sample	PH	Syn1 > C	0.31	0.29
National Sample	PH	C > Syn2	0.62	0.6
National Sample	PH	Syn2 > C	0.13	0.14
National Sample	PH	C > Syn3	0.25	0.24
National Sample	PH	Syn3 > C	0.54	0.47

^aWH indicates scans with the FOV that covers the whole head. PH indicates scans with the small-FOV that only partially covers the head.

^bC indicates the group of deployed controls and non-deployed controls. Syn1, Syn2, and Syn3 indicate subjects in the three syndrome groups.

Table 20. Comparison of number of voxels showing significant differences between controls and Syndrome 2 for the Seabees.

FOV ^a	Common voxels	Unique to adjusted scans	Unique to unadjusted scans
WH	19289	1226	108
PH	3860	145	167

^aWH indicates scans with the FOV that covers the whole head. PH indicates scans with the small-FOV that only partially covers the head.

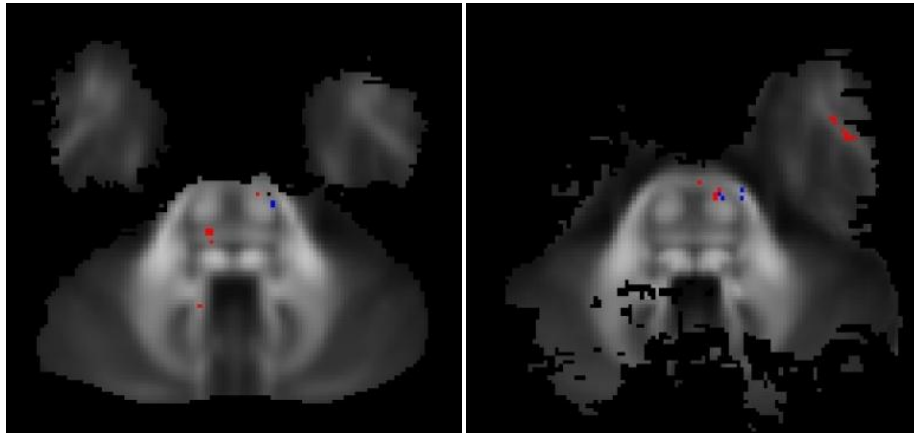


Figure 34. Voxels for which the significance of FA differences changed when artifacts were removed: The mean FA map on the left is from the whole head FOV scans for the Seabees. The mean FA map on the right is from the small-FOV scans for the Seabees. The red voxels indicate significantly greater FA for controls than for Syndrome 2 which were only detected after artifact removal. The blue voxels were only significant before artifact removal.

CHAPTER FIVE

DISCUSSION AND CONCLUSIONS

5.1 Discussion

This study has focused on finding solutions for accurately fitting diffusion weighted MRI data to a tensor model in the presence of signal void artifacts and on increasing image resolution beyond the limit which begins to introduce signal aliasing. To meet the aims of this study I ; 1) developed an innovative approach along with software tools to detect and remove signal void artifacts which are due to subject motion, cardiac pulsation-induced brain motion and scanner vibration-induced brain motion, 2) developed an innovative approach along with software tools to mask out aliased signal in DTI scans which have a field of view smaller than the subject head, and 3) showed that removing signal void artifacts from the DTI scans acquired for the Gulf War Illness study produced significant changes in FA for most subjects in which signal void artifacts were detected.

Signal void artifacts were characterized as either vibration-induced signal void artifacts or as other signal void artifacts. The vibration-induced signal void artifacts were different from the other signal void artifacts in that a single instance of the artifact spanned several slices and involved multiple volumes acquired with different diffusion weighting directions. The other signal void artifacts were associated with motion that occurred during the diffusion sensitization of an individual slice. This difference prompted a two step approach for detecting artifacts. The first step detected vibration-

induced signal void artifacts by employing a co-regressor in the diffusion tensor fitting. The tensors for the affected regions of the DTI scan were modified by solving for the tensors while excluding data from diffusion weighted volumes most susceptible to the artifact. The second step began by calculating tensors from all the diffusion weighted volumes in a DTI scan using the RESTORE algorithm and simulating the diffusion weighting volumes from the derived tensors. The simulated diffusion weighted volumes were then compared to the data of the original DTI scan. Slices of the original scans which had intensities lower than the simulated data by more than a given threshold were flagged as having artifacts. (The voxels affected by the vibration-induced artifacts were excluded from this search.) The tensors were calculated for each slice of the DTI scan using all the diffusion weighted volumes except for those affected by artifacts at that slice.

The method for masking out aliased signal was approached by utilizing *a priori* information about the subject anatomy gathered from an image acquired with sufficient FOV to avoid aliasing. A mask of signal producing tissue was generated and that map was then translated and scaled to overlay the diffusion weighted images from the DTI scan acquired with the smaller FOV. The aliasing of the signal was predicted by replicating the tissue mask in 2 dimensions with a period equal to the FOV of the DTI scan. An aliased signal mask was generated from this replicated tissue mask to exclude from further data analysis any voxels containing aliased signal.

The advantage of my approach to detecting and removing signal void artifacts over other robust tensor fitting approaches is that it identifies artifacts and removes them rather than merely minimizing the impact of outliers as the non-linear fitting and

recursive approaches do. Although the RESTORE algorithm attempts to remove the artifacts from the tensor solution, it potentially biases the tensors by removing outliers that may not be due to artifacts or noise. Furthermore, the RESTORE algorithm was not successful in removing the more subtle vibration-induced artifacts. This can be seen in Figure 19 where the tensors calculated using the RESTORE algorithm were used to simulate diffusion weighted data which was then compared to the data of the DTI scan. The ratios of the original diffusion weighted data to the simulated diffusion weighted data were greater than 1 for diffusion weighted volumes with x components in the range of 0.6 to 0.9. Examination of the outlier maps that RESTORE generated showed that only the vibration-induced artifacts in the diffusion weighted volumes with an x component of the diffusion weighting greater than 0.9 were flagged as outliers. Inclusion of the more subtle vibration-induced signal void artifacts in the tensor solution biased the simulation of the diffusion weighted volumes so that the simulated data had lower intensity for some diffusion weighting directions than the original DTI scan.

The mechanism for the vibration-induced artifacts is presumed to be tissue and fluid motion in the left and right directions which have a velocity gradient in the phase encode direction. An investigation of the fluid dynamics of the brain is beyond the scope of this study, but the many CSF/cortex boundaries and the deformability of the brain evidenced in cardiac pulsation related motion suggest many velocity gradients would be induced by vibrations in the brain. The mechanism for the motion-induced signal void artifacts was described as rigid-body rotations of the brain. This proved to be a good first order description of the artifact mechanism, but it does not account well for slices that have signal void that is localized in a slice. The rigid-body description predicts position

independent signal loss within a slice. To refine the rigid-body rotation model, angular acceleration and the fluid dynamics of the brain should be included. This modeling is beyond the scope of this research but is suggested as a mechanism which could explain why some slices had localized signal void artifacts. These same fluid dynamics considerations could be used to refine the model describing cardiac pulsation-induced artifacts as well.

There are other artifacts which were detected by the methods described here even though those artifacts were not targeted for detection. Images affected by two such artifacts were presented in Figure 24. The artifact detection method flagged slices with the artifact of the dark streaks because the signal in the streaks was substantially less than the expected signal. The artifact detection method should detect any artifacts that are characterized by markedly lower signal. The artifact in the image on the right in Figure 24 appeared in many diffusion weighted volumes but with a much more subtle effect. The periodic pattern superimposed on the image was typically faint and often hard to detect visually. It is not surprising that only the worst example of this artifact was detected with this method. However, when an artifact occurs that causes dramatic reduction in the signal, the method presented here should detect it.

Although the artifact detection method relies on tensor fitting as a step in the process, the results are still valid even when the diffusivity of the underlying tissue is not well described by a tensor. This is because the tensors are only used to generate an estimate of the expected signal to be compared with the actual diffusion weighted data. Signal estimates which are derived from tensors which only roughly fit the underlying tissue diffusivity will still be much closer to the actual signal than a signal void artifact

would be. The artifact detection process relies on the large deviation of signal void artifacts from the estimated signal. Relatively small errors in the signal estimation will not have undue impact on the artifact detection process. Once the slices with signal void artifacts are detected, they can be appropriately removed in the fitting algorithm for whatever diffusion model is used.

In the current study, the artifact detection method was only applied to brain imaging. However, the method is generally applicable to diffusion weighted imaging of targets which are prone to move, particularly when the images are acquired with single shot EPI. DTI is currently being used for evaluating other organs such as the prostate (Gurses, Tasdelen et al. 2011; Kim, Jang et al. 2011). Sinha compared the quality of cardiac gated in vivo prostate DTI data to data acquired without cardiac gating. He found that the apparent diffusion coefficients were greater in the case of ungated imaging and attributed the increase to “spurious contributions from physiological motion” (Sinha and Sinha 2004). Perhaps the detection and removal of signal void artifacts in prostate DTI imaging would give similar improvement to the data quality as did cardiac gating, but without the large increase in imaging time.

This artifact detection method is uniquely suited for data which can be simulated from a mathematical model in the way that diffusion weighted images can be simulated from the tensor data. An example of how it might be used in another modality would be for detecting artifacts in individual projections of CT scans. If there were a noise source which resulted in drastically altered intensity in a limited number of projections, this method could be adapted to detect the projections with the artifact. The back projected CT image could be used to simulate the original projects for comparison

to the recorded data.

The method of generating a simulated DTI scan proved to be useful for testing the artifact detection and removal methods. The detection method was sensitive enough to flag diffusion weighted images with simulated artifacts even after noise was added to the simulated images. Although simulating noise in the real and imaginary channels of the simulation DTI scan produced a noise measurement that was similar to the noise measurement in a real DTI scan, the visual appearance of the noise was somewhat different, particularly in the image background. This reflects the fact that the simulated noise was uncorrelated and spatially independent, whereas the noise in the acquired images was not uncorrelated and was not spatially independent. Since the images were reconstructed using parallel reconstruction to reduce acquisition time, the noise is not spatially independent as noted by Dietrich (Dietrich, Raya et al. 2007). Since the image reconstruction algorithm used apodization and partial Fourier reconstruction, the structure of the noise was modified by the interpolation which introduced spatial correlation in the noise.

Detection of signal void artifacts using simulated data was able to show that the affected slices were indeed being detected since the artifacts could be visually detected before noise addition. Simulated cardiac pulsation-induced artifacts were reliably detected except for in cases when the artifact appeared near the top or bottom of the ROI in which the artifact was simulated. The artifact near the top of the affected region was generally subtle because the mask borders had a gradual transition between affected and unaffected voxels. Cardiac pulsation-induced artifacts at the bottom of the images may have been missed because some of the volumes in the scan did not extend as

far down as the volume with the artifact. When the subject motion was simulated, the field of view changed causing the field of view in some volumes not to overlap at the bottom of the co-registered images. Only slices overlapped by all volumes were evaluated for signal void artifacts.

I was the only rater to perform the visual evaluation of flagged slices for the presence of artifacts. This raises the question of how sensitive the artifact detection method is to the accuracy of my evaluations and how transferable the method is to other researchers. The primary purpose of visual evaluation was for setting a threshold level for excluding slices from the tensor solutions. The consequence of adjusting the threshold level upward would be to allow more artifacts to influence the tensors introducing more error. Adjusting the threshold level downward would exclude data from accurate slices which would reduce the signal to noise ratio of the tensors. Although data from a second rater is not available to test the reliability of my ratings, the sensitivity of the results to the choice of threshold level was fairly low. This is because as the threshold was adjusted toward the final level, the appearance of the artifacts in the additional flagged slices was more subtle. These artifacts would have increasingly smaller effects on the tensors. On the other hand, the number of slices removed from the data at the threshold level which I selected was not excessive so the impact on signal to noise was minimal. Selecting the next lower threshold level would have only removed another 0.1% of the data in the GWIS scans. If the artifact detection method is indeed insensitive to errors in selecting the threshold level, the results have not appreciably been affected by only using one rater. Furthermore, other researchers should be able to easily obtain reliable results using the method. Nevertheless, this assumption should be tested to increase confidence in the

robustness and in the transportability of the method.

The threshold selection was performed on data combined from two populations, the Seabees and the national sample. Even though the rate of incidence of artifacts was different between the populations, the impact of signal void artifacts on individual images is dependent on the magnitude of the uncorrupted signal and the magnitude of the image noise which are determined by the imaging parameters. Therefore, the statistical characteristics of the artifacts were related to the imaging parameters rather than to the populations. Thus, separate threshold levels for the whole head FOV scans and the small-FOV scans is appropriate while a single threshold level for different cohorts is appropriate. It is interesting to note that the older population of the Seabees had a higher rate of artifacts than the national sample. The reasons for this difference are not yet known.

The FA of the simulated DTI scan was significantly affected by adding artifacts to the simulation. When the artifacts were detected and removed, the difference in FA from the simulation without artifacts was insignificant. This showed three things; 1) the presence of artifacts significantly affects the FA values of a DTI scan, 2) removing slices flagged for artifacts reduces the impact of artifacts to the level of insignificance, and 3) removing flagged slices does not introduce significant bias into the data. The change in FA caused by the removal of artifacts in the GWIS scans was significantly greater than the change in FA caused by the removal of alternate slices for 170 of the 217 scans that had slices flagged. Two of the 217 scans showed a significantly greater change when the alternate slices were removed, but in each of these cases only two adjacent slices of the FA map were altered because of a single flagged slice. This makes the paired t test less

reliable since the changes in the two samples of the paired t test were not totally independent. Based on the increased change of FA when flagged slices were removed and on the findings from the study of the simulated DTI scan, I conclude that automatic removal of signal void artifacts improves the accuracy of the FA data derived from DTI scans when signal void artifacts are present. The fact that the majority of the GWIS subjects had data flagged for removal is an indication that signal void artifacts are a typical feature of DTI scans with the sequence parameters used in that study. Applying the artifact detection method to all DTI data would be an appropriate step in quality control of DTI scans.

It was shown that errors were introduced into some FA maps of the small-FOV DTI scans when TBSS registered the FA maps to the target map. The error in the registration of the corpus callosum shown in Figure 28 appears to be a symptom of not having data above the corpus callosum to compare to the target data. An attempt was made to resolve this issue by masking the target image before the registration. However, that approach did not resolve the matter. It may be that accurate registration of images like the small-FOV data will require modification of the TBSS procedure. TBSS uses the FSL FNIRT algorithm to generate an initial registration which is later refined with the registration of skeletonised FA maps. The non-linear registration step could be refined by adjusting FNIRT input parameters or FNIRT could be replaced with a registration process that is more robust. Further effort is required to refine and validate TBSS results in the region of the corpus callosum when data above that point are missing.

Statistical tests using the TBSS algorithm with the GWIS DTI data showed that the FA along white matter tracts for Syndrome 2 subjects was significantly less than the

corresponding FA for control subjects in the Seabees study. These differences were not limited to a single white matter tract or localized region of the brain. These results agree with the results for the whole head FOV FA data that were reported earlier. (McColl, Li et al. 2009) The additional finding that this is true for the small-FOV scans is first reported here. There were no statistically significant differences between groups for the national sample data. This may be due to additional factors introduced to the subject population when it was expanded from the fairly homogeneous group of Seabees to the total population of veterans of the First Gulf War. Differences in other tensor properties such as mean diffusivity, axial diffusivity or radial diffusivity have not been considered here. Expanding the study to these quantities will be a straight forward application of the methods developed here.

TBSS analysis showed that the FA from whole head FOV DTI scans was consistently greater than the FA from small-FOV scans. This was not the expected result since the small-FOV scans had greater resolution in the axial plane. It was anticipated that the smaller voxel size would allow better resolution of crossing fibers and yield higher FA. In addition to the difference in resolution, a major difference between the whole head FOV scans and the small-FOV scans was the signal to noise ratio. An attempt was made to increase the SNR of the small-FOV scans by acquiring three times as many images for averaging. However, due to the noise floor issues discussed in Section 1.4.4.2, the high FA values in low SNR scans are reduced and the low FA values are increased. The increase of SNR that comes with more averages does not counter the biases introduced with low SNR of the individual images. Further investigation is required to determine whether lower SNR is the cause of the lower FA values in the small-FOV

scans. As a result of these differences, the FA from the small-FOV scans cannot be directly compared to the FA from the whole head FOV scans.

TBSS analysis showed that the FA for the Syndrome 2 group of the national sample was higher than the FA for the Seabees. This may indicate that the differences in the national sample population and the Seabees population are clustered in the Syndrome 2 groups. However, the small-FOV scans also showed that FA was greater in the national sample for the control groups and for the Syndrome 1 groups. These results may indicate that comparisons with the small-FOV scans are more sensitive than those with whole head FOV scans. Further investigation is required to confirm this conclusion. In particular, a more thorough analysis of the GWIS data should be conducted which includes gender, PTSD and MDD as covariates. These DTI results also confirm that, with respect to white matter water diffusivity properties, the Seabees are not representative of the 1991 Gulf War U.S. veteran population.

TBSS analysis produced very similar results using the original data and using the data with artifacts removed. This is somewhat of a surprising result given the magnitude of the errors when signal void artifacts are introduced and given that artifact removal significantly changes the FA values. On the other hand, TBSS analysis measures group averages and utilizes spatial information in testing for clusters in the data. The FA error in a single scan is averaged with the FA of the scans of the other group members. The group sizes in the GWIS ranged from 11 to 31 and the FA difference between groups with significant differences was on the order of 0.05. The error in a group average introduced by a single artifact would likely be less than a tenth of the significant group differences. The finding that artifact removal has little influence on the TBSS results

indicates that TBSS is robust in the presence of artifacts. Other analysis methods which do not rely on averages between groups, such as tractography using individual scans, are likely to show greater differences when comparing scans corrupted by artifacts with scans where the artifacts are removed.

5.2 Conclusions

When analyzing DTI data, the presence of signal void artifacts should be assessed and steps should be taken to remove affected slices. In large studies it is nearly impossible to visually assess all collected data. An automated approach such as the one presented here should be used to assess the data for artifacts and to remove the affected slices. The automated method for removing artifacts presented here was demonstrated on MRI DTI scans of the head. However, the method could be adapted for use with DTI scans of other organs such as the prostate. Furthermore, this method may be applicable to any imaging modality in which the original data can be reconstructed from a mathematical model that is fit using error minimization. An example would be CT scans if an artifact were introduced which only affected a limited number of projections.

When using a field of view smaller than the object being imaged, a larger field of view image with similar geometric distortion should also be acquired. This is true unless the signal outside the field of view is suppressed. The image with the larger field of view can be used as *a priori* information for predicting where aliased signal will occur. The larger field of view image should have contrast and geometric distortion as closely matched as possible to the small field of view image. The field of view should be just

large enough to avoid signal aliasing artifacts. For a DTI scan collected with EPI readout, such a reference scan should only take a few seconds.

The physiological factors of heart rate and respiration should be monitored and recording in a way that can be correlated with the image acquisition timing. Gating for the phases of the cardiac and respiratory cycles would be ideal, but the increase in the required scan time is generally considered unacceptable. The availability of physiologic data would make detecting and accounting for these factors during image processing more accurate.

5.3 Future Work

Since the solution of applying cardiac gating for avoiding the cardiac pulsation-induced artifacts is generally undesirable, a compromise would be to monitor the cardiac cycle and note which image slices are acquired during the portion of the cardiac cycle which produces artifacts. Then before the DTI scan has been completed, and as close in time to the affected slice as possible, the slice should be reimaged and the new image should replace the potentially affected slice in the image volume. The same approach could be taken for motion-induced signal void artifacts. The subject motion at the time of diffusion sensitization should be monitored. A prediction of the likelihood of a signal void artifact could be made based on the characteristics of the motion and the direction of the diffusion weighting. Then the slice should be reacquired if a motion-induced signal void artifact is predicted. Even if slice reimagining is not implemented, a record of the motion during diffusion sensitization could be used to flag slices for removal during image processing.

A more careful analysis of the GWIS should be conducted which includes gender, PTSD and MDD as covariates. Other studies have shown that MDD affects white matter integrity (Li, Ma et al. 2007; Zhu, Wang et al. 2011) so MDD should be included as a covariate when analyzing the GWIS data. Several subjects from both the Seabees (n=9) and the national sample (n=22) were diagnosed with PTSD. The association of PTSD with changes in FA has been demonstrated by others (Abe, Yamasue et al. 2006; Zhang, Zhang et al. 2011) so PTSD should also be included in the analysis.

APPENDIX A **Diffusion Weighting Vectors**

Vector components for the 56 diffusion sensitizing gradients and their b values.

Vector #	x	y	z	b(s/mm ²)
0	0.00000	0.00000	0.00000	0.00000
1	0.00000	0.00000	0.00000	0.00000
2	0.00000	0.00000	0.00000	0.00000
3	1.00000	0.00000	0.00200	1000.00000
4	0.39019	0.92073	0.00131	1000.00000
5	-0.07654	0.53791	-0.83952	995.00000
6	0.89831	-0.41591	-0.14164	1000.00000
7	-0.20532	-0.77759	-0.59431	995.00000
8	-0.68674	-0.35340	-0.63522	995.00000
9	0.70176	0.45636	-0.54706	995.00000
10	-0.00500	0.99965	-0.02603	1000.00000
11	0.76975	0.08080	-0.63321	995.00000
12	-0.20199	-0.92917	0.30959	1000.00000
13	0.17082	-0.92578	0.33726	1000.00000
14	0.46066	-0.75765	0.46234	1000.00000
15	-0.44138	-0.57554	-0.68843	995.00000
16	-0.69644	0.68839	-0.20270	1000.00000
17	-0.43913	0.01117	0.89836	1000.00000

18	-0.68286	-0.72962	-0.03683	1000.00000
19	0.71238	-0.45284	0.53614	1000.00000
20	0.20076	-0.22078	0.95444	1000.00000
21	-0.29709	-0.76736	0.56824	1000.00000
22	-0.74423	0.46188	0.48248	1000.00000
23	0.56468	0.75072	-0.34287	995.00000
24	-0.62828	0.25263	0.73583	1000.00000
25	0.92465	-0.14433	-0.35241	1000.00000
26	0.27741	0.55319	-0.78551	995.00000
27	-0.16376	-0.23787	0.95739	1000.00000
28	0.23639	-0.94938	-0.20687	1000.00000
29	0.88696	-0.42426	0.18253	1000.00000
30	0.02318	-0.09067	-0.99561	995.00000
31	0.16650	0.94323	0.28738	1000.00000
32	0.82794	0.52187	-0.20533	1000.00000
33	-0.26542	0.32566	0.90747	1000.00000
34	-0.49181	0.13419	-0.86030	995.00000
35	-0.52467	-0.31258	0.79184	1000.00000
36	-0.46844	-0.19590	-0.86150	995.00000
37	-0.93736	-0.33977	-0.07693	1000.00000
38	-0.91198	0.15249	-0.38085	1000.00000
39	0.67936	-0.71530	-0.16378	1000.00000

40	-0.44187	0.89497	-0.06147	1000.00000
41	0.92479	0.20602	-0.31988	995.00000
42	-0.74001	0.03199	-0.67183	995.00000
43	0.77839	0.53305	0.33161	1000.00000
44	0.15232	-0.82308	-0.54711	995.00000
45	-0.45962	0.49152	-0.73970	995.00000
46	-0.12840	0.76355	-0.63285	995.00000
47	0.47530	-0.75764	-0.44730	995.00000
48	-0.20239	-0.36737	-0.90779	995.00000
49	-0.51336	-0.77557	-0.36736	1000.00000
50	0.90868	0.17966	0.37685	1000.00000
51	0.40402	-0.56397	-0.72021	995.00000
52	-0.01719	0.59330	0.80480	1000.00000
53	0.00000	0.00000	0.00000	0.00000
54	0.00000	0.00000	0.00000	0.00000
55	0.00000	0.00000	0.00000	0.00000

APPENDIX B

Scripts for Simulation of Motion-Induced Signal Void Artifacts

The script “dwi_sim_EC.sh” is used to simulate a DTI scan starting with a non-diffusion weighted reference volume, a tensor map of the diffusion tensors as generated by the DTIFIT algorithm of FSL, a set of affine matrices for simulating motion and eddy current geometric distortions, and a set of diffusion weighting vectors for the simulation scan.

```
simulation_dir=/home/keith/GWS/Results/simulation
cd $simulation_dir
num=0;
bvals=(`cat bvals_2c`);
cat bvecs_2c|
while read -a bvec;do
    vol=dwi_sim_vol`zeropad $num 4`;
    vol_EC=dwi_sim_EC_vol`zeropad $num 4`;
    vol_tensor=dwi_sim_tensor_vol`zeropad $num 4`;
    S0_EC=dti2c_fit_S0_EC_vol`zeropad $num 4`
    mat=ECmat_vol`zeropad $num 4`.mat
    bval=${bvals[$num]};
    if test $bval -ne 0;then
        bvec_norm=`echo "scale=6;sqrt (${bvec[0]}^2 + ${bvec[1]}^2 +
${bvec[2]}^2)"|bc`;
        b_x=`echo "scale=6;$bval * ${bvec[0]} / $bvec_norm"|bc`;
```

```

b_y=`echo "scale=6;$bval * ${bvec[1]} / $bvec_norm"|bc`;
b_z=`echo "scale=6;$bval * ${bvec[2]} / $bvec_norm"|bc`;

else

b_x=0;

b_y=0;

b_z=0;

fi;

vecreg -i dti2c_fit_tensor -o EC_tensor -r dti2clas -t inv_mat/inv_$mat

fslmaths img_1 -mul $b_x bvec_x;

fslmaths img_1 -mul $b_y bvec_y;

fslmaths img_1 -mul $b_z bvec_z;

fslmerge -t bvec_1 bvec_x bvec_y bvec_z

flirt -in dti2c_fit_S0 -ref dti2clas -out $S0_EC -applyxfm -init inv_mat/inv_$mat


fslsplit EC_tensor EC_tensor -t

fslmerge -t EC_tensor_1 EC_tensor0000 EC_tensor0001 EC_tensor0002

fslmerge -t EC_tensor_2 EC_tensor0001 EC_tensor0003 EC_tensor0004

fslmerge -t EC_tensor_3 EC_tensor0002 EC_tensor0004 EC_tensor0005


fslmaths EC_tensor_1 -mul bvec_1 -Tmean -mul 3 -sqr btensor1_2

fslmaths EC_tensor_2 -mul bvec_1 -Tmean -mul 3 -sqr btensor2_2

fslmaths EC_tensor_3 -mul bvec_1 -Tmean -mul 3 -sqr btensor3_2

```

```

fslmaths btensor1_2 -add btensor2_2 -add btensor3_2 -sqrt -mul -1 -exp -mul $S0_EC
$vol_tensor

```

```

num=`expr $num + 1`;
# test $num -gt 5 && exit;

done

```

```

imrm EC_tensor*

imrm btensor*

imrm bvec*

```

```

images=`imglob dti2c_fit_S0_EC_vol????*`

fslmerge -t dwi_sim_S0_EC $images

imrm $images

```

```

images=`imglob dwi_sim_tensor_vol????*`

fslmerge -t dwi_sim_tensor $images

imrm $images

```


The script “simulate_motion_artifacts.sh” is used to simulate the motion-induced signal loss mechanisms described above. The signal loss is applied to a simulated DTI scan. The script requires as input a simulated DTI scan, a motion profile, and the profile of the diffusion weightings simulated in the scan. The script prepares simulation parameters for each slice of the simulation DTI scan and calls the script “add_phase_grad_slice.sh” to perform the simulation. To allow quick execution, the volumes are divided into eight groups which are processed in parallel.

```
simulate_dir=/home/keith/GWS/Results/simulation;

G=0.03023;

d=0.02221;

D=0.03842;

zdim=2.0;

fov=512;#twice actual fov so rotated phase image covers mag image

xdim=2.0;

ydim=2.0;

tdim=8.3;

xdim_4=.5

ydim_4=.5


cd $simulate_dir;

### Set up 512x512 image as ref for interpolation with xdim, ydim 1/4 of original
```

```

fslcreatehd 512 512 1 1 $xdim_4 $ydim_4 $zdim $tdim 0 0 0 4 512_zero

fslsplit dwi_sim_tensor dwi_sim_tensor_vol;

vols=(`imglob dwi_sim_tensor_vol*`);

bvec_x=(`head -1 bvecs_2c_trans|tail -1`)
bvec_y=(`head -2 bvecs_2c_trans|tail -1`)
bvec_z=(`head -3 bvecs_2c_trans|tail -1`)

bvals=(`head -1 bvals_2c_trans|tail -1`)

#for ((i=0;i<${#vols[@]};i++));do

vol_section=`expr ${#vols[@]} / 8`

start1=`expr 0 \* $vol_section`
stop1=`expr 1 \* $vol_section`
start2=$stop1
stop2=`expr 2 \* $vol_section`
start3=$stop2
stop3=`expr 3 \* $vol_section`
start4=$stop3
stop4=`expr 4 \* $vol_section`
start5=$stop4
stop5=`expr 5 \* $vol_section`
start6=$stop5
stop6=`expr 6 \* $vol_section`
start7=$stop6
stop7=`expr 7 \* $vol_section`

```

```

start8=$stop7

stop8=${#vols[@]}

for ((i=$start1;i<$stop1;i++));do

    ivol=`zeropad $i 4`;

    ivol_x=`expr $i \* 3 + 1`

    ivol_y=`expr $i \* 3 + 2`

    ivol_z=`expr $i \* 3 + 3`

    ivol_d=`expr $i + 1`

    num_Wdeg=`head -1 profile_mag|wc|awk '{print $2}`

    Wvec_x=(`head -$ivol_x profile_vec|tail -1`)

    Wvec_y=(`head -$ivol_y profile_vec|tail -1`)

    Wvec_z=(`head -$ivol_z profile_vec|tail -1`)

    Wdeg=(`head -$ivol_d profile_mag|tail -1`)

    G_val=`echo "scale=5;$G*${bvals[$i]}/1000"|bc`;

    degs=(`for ((k=0;k<${#Wdeg[@]};k++));do echo ${Wdeg[$k]};done|sort -u`)

    echo $ivol_d $num_Wdeg ${Wdeg[@]} ${degs[@]} ${#degs[@]}

    if test ${#degs[@]} -gt 2;then #revise volume only if motion not zero (all same)

        mkdir -p vol$ivol

        cd vol$ivol

        imrm slice*;

        fslsplit ../${vols[$i]} slice -z;

        slice_names=(`imglob slice*`);

```

```

for ((j=0;j<${#slice_names[@]};j++));do

    j_1=`expr $j + 1`;

    if test ${Wdeg[$j_1]} != 0;then

        flirt -in ${slice_names[$j]} -ref ../512_zero -applyxfm -init ../eye.mat -out

${slice_names[$j]}

        echo "${bvec_x[$i]} ${bvec_y[$i]} ${bvec_z[$i]} $G_val $d $D

${Wvec_x[$j_1]} ${Wvec_y[$j_1]} ${Wvec_z[$j_1]} ${Wdeg[$j_1]} $fov $xdim

$ydim $zdim $tdim ${slice_names[$j]}"| bash $simulate_dir/add_phase_grad_slice.sh;

    else

        imcp ${slice_names[$j]} abs_adjusted_${slice_names[$j]}

    fi;

done;

adjusted_slices=`imglob abs_adjusted_slice*`;

fslmerge -z $simulate_dir/adjusted_dwi_sim_vol$ivol $adjusted_slices;

#   imrm slice*;

#   imrm adjusted_slice*;

cd $simulate_dir/

else

    imcp ${vols[$i]} adjusted_dwi_sim_vol$ivol

fi

done>sim_mot_art1.output&

for ((i=$start2;i<$stop2;i++));do

```

```

ivol=`zeropad $i 4`;

ivol_x=`expr $i \* 3 + 1`

ivol_y=`expr $i \* 3 + 2`

ivol_z=`expr $i \* 3 + 3`

ivol_d=`expr $i + 1`

num_Wdeg=`head -1 profile_mag|wc|awk '{print $2}`

Wvec_x=(`head -$ivol_x profile_vec|tail -1`)

Wvec_y=(`head -$ivol_y profile_vec|tail -1`)

Wvec_z=(`head -$ivol_z profile_vec|tail -1`)

Wdeg=(`head -$ivol_d profile_mag|tail -1`)

G_val=`echo "scale=5;$G*${bvals[$i]}/1000"|bc`;

degs=(`for ((k=0;k<${#Wdeg[@]};k++));do echo ${Wdeg[$k]};done|sort -u`)

echo $ivol_d $num_Wdeg ${Wdeg[@]} ${degs[@]} ${#degs[@]}

if test ${#degs[@]} -gt 2;then #revise volume only if motion not zero (all same)

    mkdir -p vol$ivol

    cd vol$ivol

    imrm slice*;

    fslsplit ../${vols[$i]} slice -z;

    slice_names=(`imglob slice*`);

    for ((j=0;j<${#slice_names[@]};j++));do

        j_1=`expr $j + 1`;

        if test ${Wdeg[$j_1]} != 0;then

            flirt -in ${slice_names[$j]} -ref ../512_zero -applyxfm -init ../eye.mat -out

```

```

${slice_names[$j]}

    echo "${bvec_x[$i]} ${bvec_y[$i]} ${bvec_z[$i]} $G_val $d $D

${Wvec_x[$j_1]} ${Wvec_y[$j_1]} ${Wvec_z[$j_1]} ${Wdeg[$j_1]} $fov $xdim
$ydim $zdim $tdim ${slice_names[$j]}"| bash $simulate_dir/add_phase_grad_slice.sh;

    else

        imcp ${slice_names[$j]} abs_adjusted_${slice_names[$j]}

    fi;

done;

adjusted_slices=`imglob abs_adjusted_slice*`;

fslmerge -z $simulate_dir/adjusted_dwi_sim_vol$ivol $adjusted_slices;

#   imrm slice*;

#   imrm adjusted_slice*;

cd $simulate_dir/

else

    imcp ${vols[$i]} adjusted_dwi_sim_vol$ivol

fi

done>sim_mot_art2.output&

for ((i=$start3;i<$stop3;i++));do

    ivol=`zeropad $i 4`;

    ivol_x=`expr $i \* 3 + 1`

    ivol_y=`expr $i \* 3 + 2`

    ivol_z=`expr $i \* 3 + 3`

```

```

ivol_d=`expr $i + 1`

num_Wdeg=`head -1 profile_mag|wc|awk '{print $2}`

Wvec_x=(`head -$ivol_x profile_vec|tail -1`)

Wvec_y=(`head -$ivol_y profile_vec|tail -1`)

Wvec_z=(`head -$ivol_z profile_vec|tail -1`)

Wdeg=(`head -$ivol_d profile_mag|tail -1`)

G_val=`echo "scale=5;$G*${bvals[$i]}/1000"|bc`;

degs=(`for ((k=0;k<${#Wdeg[@]};k++));do echo ${Wdeg[$k]};done|sort -u`)

echo $ivol_d $num_Wdeg ${Wdeg[@]} ${degs[@]} ${#degs[@]}

if test ${#degs[@]} -gt 2;then #revise volume only if motion not zero (all same)

    mkdir -p vol$ivol

    cd vol$ivol

    imrm slice*;

    fslsplit ../${vols[$i]} slice -z;

    slice_names=(`imglob slice*`);

    for ((j=0;j<${#slice_names[@]};j++));do

        j_1=`expr $j + 1`;

        if test ${Wdeg[$j_1]} != 0;then

            flirt -in ${slice_names[$j]} -ref ../512_zero -applyxfm -init ../eye.mat -out

            ${slice_names[$j]}

            echo "${bvec_x[$i]} ${bvec_y[$i]} ${bvec_z[$i]} $G_val $d $D

            ${Wvec_x[$j_1]} ${Wvec_y[$j_1]} ${Wvec_z[$j_1]} ${Wdeg[$j_1]} $fov $xdim

            $ydim $zdim $tdim ${slice_names[$j]}"| bash $simulate_dir/add_phase_grad_slice.sh;

```

```

else

    imcp ${slice_names[$j]} abs_adjusted_${slice_names[$j]}

fi;

done;

adjusted_slices=`imglob abs_adjusted_slice*`;

fslmerge -z $simulate_dir/adjusted_dwi_sim_vol$ivol $adjusted_slices;

#   imrm slice*;

#   imrm adjusted_slice*;

cd $simulate_dir/

else

    imcp ${vols[$i]} adjusted_dwi_sim_vol$ivol

fi

done>sim_mot_art3.output&

for ((i=$start4;i<$stop4;i++));do

    ivol=`zeropad $i 4`;

    ivol_x=`expr $i \* 3 + 1`

    ivol_y=`expr $i \* 3 + 2`

    ivol_z=`expr $i \* 3 + 3`

    ivol_d=`expr $i + 1`

    num_Wdeg=`head -1 profile_mag|wc|awk '{print $2}`

    Wvec_x=(`head -$ivol_x profile_vec|tail -1`)

    Wvec_y=(`head -$ivol_y profile_vec|tail -1`)

```



```

Wvec_z=(`head -$ivol_z profile_vec|tail -1`)
Wdeg=(`head -$ivol_d profile_mag|tail -1`)
G_val=`echo "scale=5;$G*${bvals[$i]}/1000"|bc`;
degs=(`for ((k=0;k<${#Wdeg[@]};k++));do echo ${Wdeg[$k]};done|sort -u`)
echo $ivol_d $num_Wdeg ${Wdeg[@]} ${degs[@]} ${#degs[@]}
if test ${#degs[@]} -gt 2;then #revise volume only if motion not zero (all same)
    mkdir -p vol$ivol
    cd vol$ivol
    imrm slice*;
    fslsplit ../${vols[$i]} slice -z;
    slice_names=(`imglob slice*`);
    for ((j=0;j<${#slice_names[@]};j++));do
        j_1=`expr $j + 1`;
        if test ${Wdeg[$j_1]} != 0;then
            flirt -in ${slice_names[$j]} -ref ../512_zero -applyxfm -init ../eye.mat -out
            ${slice_names[$j]}
            echo "${bvec_x[$i]} ${bvec_y[$i]} ${bvec_z[$i]} $G_val $d $D
            ${Wvec_x[$j_1]} ${Wvec_y[$j_1]} ${Wvec_z[$j_1]} ${Wdeg[$j_1]} $fov $xdim
            $ydim $zdim $tdim ${slice_names[$j]}"| bash $simulate_dir/add_phase_grad_slice.sh;
        else
            imcp ${slice_names[$j]} abs_adjusted_${slice_names[$j]}
        fi;
    done;

```

```

        adjusted_slices=`imglob abs_adjusted_slice*`;    fslmerge -z
$simulate_dir/adjusted_dwi_sim_vol$ivol $adjusted_slices;

#    imrm slice*;

#    imrm adjusted_slice*;

    cd $simulate_dir/

else

    imcp ${vols[$i]} adjusted_dwi_sim_vol$ivol

fi

done>sim_mot_art4.output&

for ((i=$start5;i<$stop5;i++));do

    ivol=`zeropad $i 4`;

    ivol_x=`expr $i \* 3 + 1`

    ivol_y=`expr $i \* 3 + 2`

    ivol_z=`expr $i \* 3 + 3`

    ivol_d=`expr $i + 1`

    num_Wdeg=`head -1 profile_mag|wc|awk '{print $2}`

    Wvec_x=(`head -$ivol_x profile_vec|tail -1`)

    Wvec_y=(`head -$ivol_y profile_vec|tail -1`)

    Wvec_z=(`head -$ivol_z profile_vec|tail -1`)

    Wdeg=(`head -$ivol_d profile_mag|tail -1`)

    G_val=`echo "scale=5;$G*${bvals[$i]}/1000"|bc`;

```

```

degsg=(`for ((k=0;k<${#Wdeg[@]};k++));do echo ${Wdeg[k]};done|sort -u`)
echo $ivol_d $num_Wdeg ${Wdeg[@]} ${degsg[@]} ${#degsg[@]}

if test ${#degsg[@]} -gt 2;then #revise volume only if motion not zero (all same)

    mkdir -p vol$ivol

    cd vol$ivol

    imrm slice*;

    fslsplit ../${vols[$i]} slice -z;

    slice_names=(`imglob slice*`);

    for ((j=0;j<${#slice_names[@]};j++));do

        j_1=`expr $j + 1`;

        if test ${Wdeg[$j_1]} != 0;then

            flirt -in ${slice_names[$j]} -ref ../512_zero -applyxfm -init ../eye.mat -out
            ${slice_names[$j]}

            echo "${bvec_x[$i]} ${bvec_y[$i]} ${bvec_z[$i]} $G_val $d $D
            ${Wvec_x[$j_1]} ${Wvec_y[$j_1]} ${Wvec_z[$j_1]} ${Wdeg[$j_1]} $fov $xdim
            $ydim $zdim $tdim ${slice_names[$j]}"| bash $simulate_dir/add_phase_grad_slice.sh;

        else

            imcp ${slice_names[$j]} abs_adjusted_${slice_names[$j]}

        fi;

    done;

    adjusted_slices=`imglob abs_adjusted_slice*`;

    fslmerge -z $simulate_dir/adjusted_dwi_sim_vol$ivol $adjusted_slices;

#    imrm slice*;

```

```

#   imrm adjusted_slice*;

    cd $simulate_dir/

else

    imcp ${vols[$i]} adjusted_dwi_sim_vol$ivol

fi

done>sim_mot_art5.output&

for ((i=$start6;i<$stop6;i++));do

    ivol=`zeropad $i 4`;

    ivol_x=`expr $i \* 3 + 1`

    ivol_y=`expr $i \* 3 + 2`

    ivol_z=`expr $i \* 3 + 3`

    ivol_d=`expr $i + 1`

    num_Wdeg=`head -1 profile_mag|wc|awk '{print $2}'`

    Wvec_x=(`head -$ivol_x profile_vec|tail -1`)

    Wvec_y=(`head -$ivol_y profile_vec|tail -1`)

    Wvec_z=(`head -$ivol_z profile_vec|tail -1`)

    Wdeg=(`head -$ivol_d profile_mag|tail -1`)

    G_val=`echo "scale=5;$G*${bvals[$i]}/1000"|bc`;

    degs=(`for ((k=0;k<${#Wdeg[@]};k++));do echo ${Wdeg[$k]};done|sort -u`)

    echo $ivol_d $num_Wdeg ${Wdeg[@]} ${degs[@]} ${#degs[@]}

    if test ${#degs[@]} -gt 2;then #revise volume only if motion not zero (all same)

        mkdir -p vol$ivol

```

```

cd vol$ivol

imrm slice*;

fslsplit ../${vols[$i]} slice -z;

slice_names=(`imglob slice*`);

for ((j=0;j<${#slice_names[@]};j++));do

    j_1=`expr $j + 1`;

    if test ${Wdeg[$j_1]} != 0;then

        flirt -in ${slice_names[$j]} -ref ../512_zero -applyxfm -init ../eye.mat -out

${slice_names[$j]}

        echo "${bvec_x[$i]} ${bvec_y[$i]} ${bvec_z[$i]} $G_val $d $D

${Wvec_x[$j_1]} ${Wvec_y[$j_1]} ${Wvec_z[$j_1]} ${Wdeg[$j_1]} $fov $xdim

$ydim $zdim $tdim ${slice_names[$j]}"| bash $simulate_dir/add_phase_grad_slice.sh;

    else

        imcp ${slice_names[$j]} abs_adjusted_${slice_names[$j]}

    fi;

done;

adjusted_slices=`imglob abs_adjusted_slice*`;

fslmerge -z $simulate_dir/adjusted_dwi_sim_vol$ivol $adjusted_slices;

#   imrm slice*;

#   imrm adjusted_slice*;

cd $simulate_dir/

else

    imcp ${vols[$i]} adjusted_dwi_sim_vol$ivol

```

fi

done>sim_mot_art6.output&

for ((i=\$start7;i<\$stop7;i++));do

ivol=`zeropad \$i 4`;

ivol_x=`expr \$i * 3 + 1`

ivol_y=`expr \$i * 3 + 2`

ivol_z=`expr \$i * 3 + 3`

ivol_d=`expr \$i + 1`

num_Wdeg=`head -1 profile_mag|wc|awk '{print \$2}`

Wvec_x=(`head -\$ivol_x profile_vec|tail -1`)

Wvec_y=(`head -\$ivol_y profile_vec|tail -1`)

Wvec_z=(`head -\$ivol_z profile_vec|tail -1`)

Wdeg=(`head -\$ivol_d profile_mag|tail -1`)

G_val=`echo "scale=5;\$G*\${bvals[\$i]}/1000"|bc`;

degs=(`for ((k=0;k<\${#Wdeg[@]};k++));do echo \${Wdeg[\$k]};done|sort -u`)

echo \$ivol_d \$num_Wdeg \${Wdeg[@]} \${degs[@]} \${#degs[@]}

if test \${#degs[@]} -gt 2;then #revise volume only if motion not zero (all same)

mkdir -p vol\$ivol

cd vol\$ivol

imrm slice*;

fsplit ../\${vols[\$i]} slice -z;

slice_names=(`imglob slice*`);

```

for ((j=0;j<${#slice_names[@]};j++));do

    j_1=`expr $j + 1`;

    if test ${Wdeg[$j_1]} != 0;then

        flirt -in ${slice_names[$j]} -ref ../512_zero -applyxfm -init ../eye.mat -out

${slice_names[$j]}

        echo "${bvec_x[$i]} ${bvec_y[$i]} ${bvec_z[$i]} $G_val $d $D

${Wvec_x[$j_1]} ${Wvec_y[$j_1]} ${Wvec_z[$j_1]} ${Wdeg[$j_1]} $fov $xdim

$ydim $zdim $tdim ${slice_names[$j]}"| bash $simulate_dir/add_phase_grad_slice.sh;

    else

        imcp ${slice_names[$j]} abs_adjusted_${slice_names[$j]}

    fi;

done;

adjusted_slices=`imglob abs_adjusted_slice*`;

fslmerge -z $simulate_dir/adjusted_dwi_sim_vol$ivol $adjusted_slices;

#   imrm slice*;

#   imrm adjusted_slice*;

cd $simulate_dir/

else

    imcp ${vols[$i]} adjusted_dwi_sim_vol$ivol

fi

done>sim_mot_art7.output&

for ((i=$start8;i<$stop8;i++));do

```

```

ivol=`zeropad $i 4`;

ivol_x=`expr $i \* 3 + 1`

ivol_y=`expr $i \* 3 + 2`

ivol_z=`expr $i \* 3 + 3`

ivol_d=`expr $i + 1`

num_Wdeg=`head -1 profile_mag|wc|awk '{print $2}`

Wvec_x=(`head -$ivol_x profile_vec|tail -1`)

Wvec_y=(`head -$ivol_y profile_vec|tail -1`)

Wvec_z=(`head -$ivol_z profile_vec|tail -1`)

Wdeg=(`head -$ivol_d profile_mag|tail -1`)

G_val=`echo "scale=5;$G*${bvals[$i]}/1000"|bc`;

degs=(`for ((k=0;k<${#Wdeg[@]};k++));do echo ${Wdeg[$k]};done|sort -u`)

echo $ivol_d $num_Wdeg ${Wdeg[@]} ${degs[@]} ${#degs[@]}

if test ${#degs[@]} -gt 2;then #revise volume only if motion not zero (all same)

    mkdir -p vol$ivol

    cd vol$ivol

    imrm slice*;

    fslsplit ../${vols[$i]} slice -z;

    slice_names=(`imglob slice*`);

    for ((j=0;j<${#slice_names[@]};j++));do

        j_1=`expr $j + 1`;

        if test ${Wdeg[$j_1]} != 0;then

            flirt -in ${slice_names[$j]} -ref ../512_zero -applyxfm -init ../eye.mat -out

```



```

${slice_names[$j]}

    echo "${bvec_x[$i]} ${bvec_y[$i]} ${bvec_z[$i]} $G_val $d $D

${Wvec_x[$j_1]} ${Wvec_y[$j_1]} ${Wvec_z[$j_1]} ${Wdeg[$j_1]} $fov $xdim
$ydim $zdim $tdim ${slice_names[$j]}"| bash $simulate_dir/add_phase_grad_slice.sh;

    else

        imcp ${slice_names[$j]} abs_adjusted_${slice_names[$j]}

    fi;

done;

adjusted_slices=`imglob abs_adjusted_slice*`;

fslmerge -z $simulate_dir/adjusted_dwi_sim_vol$ivol $adjusted_slices;

#   imrm slice*;

#   imrm adjusted_slice*;

cd $simulate_dir/

else

    imcp ${vols[$i]} adjusted_dwi_sim_vol$ivol

fi

done>sim_mot_art8.output&

#vols_512=`imglob 512_dwi_sim_tensor_vol*`;

#imrm $vols_512

#imrm 512_zero

```

```
#adjusted_vols=`imglob adjusted_dwi_sim_vol*`;
#fslmerge -t motion_adjusted_dwi_sim $adjusted_vols;
#imrm $adjusted_vols;
#imrm ${vols[@]};
```

The script “add_phase_grad_slice.sh” simulates signal loss due to subject motion during diffusion weighting. This script is called from “simulate_motion_artifacts.sh”

```
gamma=267500000
G=0.03023;
d=0.02221;
D=0.03842;
zdim=2.0
bvec=(0 -1 0)
bval=1000
Wvec=(0 0 1)
Wdeg=10.0
read b_x b_y b_z G d D W_x W_y W_z Wdeg fov xdim ydim zdim tdim input_image;
bvec=($b_x $b_y $b_z);
Wvec=($W_x $W_y $W_z);
Wval=`echo "scale=5; ${Wdeg}*4*a(1)/180"|bc -l`;#scale to radians
#grad_dir=bvec X Wvec
grad_dir=(`echo "scale=12; ${bvec[1]} * ${Wvec[2]} - ${bvec[2]} * ${Wvec[1]}"|bc`
`echo "scale=12; ${bvec[2]} * ${Wvec[0]} - ${bvec[0]} * ${Wvec[2]}"|bc` `echo
"scale=12; ${bvec[0]} * ${Wvec[1]} - ${bvec[1]} * ${Wvec[0]}"|bc`);
#grad_mag=gamma * gradient mag * Omega * pulse duration * pulse separation
grad_mag=`echo "5 k $gamma $G * $Wval * $d * $D * p"|sed s/_/_/dc`;
```

```

grad_z=`echo "5 k ${grad_dir[2]} $grad_mag * p"|sed s/-/_/|sed s/-/_/|dc`
phi_z=`echo "5 k $grad_z $zdim * 1000 / p"|sed s/-/_/|dc`
echo "grad_z=$grad_z phi_z=$phi_z grad_dir[0]={grad_dir[0]}
grad_dir[1]={grad_dir[1]} grad_dir[2]={grad_dir[2]}"
z_factor=`echo "scale=12; if ( ${phi_z} ) sqrt((1-c($phi_z))^2+s($phi_z)^2)/$phi_z else
1"|bc -l`

phi=`echo "scale=5; if ( ${grad_dir[0]} ) 0 else 90"|bc` #prevents divide by 0

if ! test $phi = 90;then
    phi=`echo "scale=5; 45/a(1)*a(${grad_dir[1]}/${grad_dir[0]})"|bc -l`
elif test `echo "${grad_dir[1]}"|sed s/-/_/` != ${grad_dir[1]};then
    phi=270;
fi;

if test `echo "${grad_dir[0]}"|sed s/-/_/` != ${grad_dir[0]};then
    phi=`echo "scale=5; $phi + 180"|bc`;
fi

if test `echo "${phi}"|sed s/-/_/` != ${phi};then
    phi=`echo "scale=5; $phi + 360"|bc`;
fi

```

```

grad_factor=`echo "scale=5;

${grad_mag}*sqrt(${grad_dir[0]}^2+${grad_dir[1]}^2)"|bc`

grad_factor=`dc -e "0 k $grad_factor $fov * 1000 / p"`

phi=`dc -e "0 k $phi 1 / p"`

if test $phi -lt 0 -o $phi -gt 360;then

    echo "Phi must be between 0 and 360.";

    exit;

fi;

if test $phi -le 90;then

    rot_phi=-$phi;

    dx=`expr $fov / 2`;

    dy=0;

    direction=1

elif test $phi -le 180;then

    rot_phi=`expr 180 - $phi`;

    dx=0;

    dy=`expr $fov / 2`;

    direction=-1

elif test $phi -le 270;then

    rot_phi=`expr 180 - $phi`;

    dx=`expr $fov / 2`;

    dy=0;

    direction=-1

```

```

else

    rot_phi=`expr 360 - $phi`;

    dx=0;

    dy=`expr $fov / 2`;

    direction=1

fi;

echo "phi=$phi rot_phi=$rot_phi rot_center(x,y)=$(dx,$dy) direction=$direction

grad_factor=$grad_factor z_factor=$z_factor"

#exit

fslcreatehd 1 2 1 1 $fov $fov $zdim $tdim 0 0 0 16 zero_1x2x1

fslmaths zero_1x2x1 -add 1 pi_1x2x1

fslmerge -x sin_2x2x1 zero_1x2x1 pi_1x2x1

fslmaths sin_2x2x1 -mul $grad_factor sin_2x2x1


in_image=${input_image}

in_image_scaled=${in_image}_scaled

fslmaths $in_image -mul $z_factor $in_image_scaled -odt float


makerot -t $rot_phi -c ${dx},${dy},0 -o ${phi}.mat

flirt -in sin_2x2x1 -ref ${in_image} -applyxfm -init ${phi}.mat -out

sin_2x2x1_${phi}_${grad_factor}

fslmaths sin_2x2x1_${phi}_${grad_factor} -mul $direction

sin_2x2x1_${phi}_${grad_factor}

```

```

fslcomplex -complexpolar $in_image_scaled sin_2x2x1_{$phi}_{$grad_factor}
adjusted_{$in_image}

fslfft adjusted_{$in_image} adjusted_{$in_image}_fft

fslcomplex -realcartesian adjusted_{$in_image}_fft adjusted_{$in_image}_fft_real
adjusted_{$in_image}_fft_imag

fslroi adjusted_{$in_image}_fft_real adjusted_{$in_image}_fft_real_1 0 64 0 16 0 1
fslroi adjusted_{$in_image}_fft_real adjusted_{$in_image}_fft_real_2 448 64 0 16 0 1
fslroi adjusted_{$in_image}_fft_real adjusted_{$in_image}_fft_real_3 0 64 16 48 0 1
fslroi adjusted_{$in_image}_fft_real adjusted_{$in_image}_fft_real_4 448 64 16 48 0 1
#fslroi adjusted_{$in_image}_fft_real adjusted_{$in_image}_fft_real_5 0 64 448 48 0 1
#fslroi adjusted_{$in_image}_fft_real adjusted_{$in_image}_fft_real_6 448 64 448 48 0
1

fslroi adjusted_{$in_image}_fft_real adjusted_{$in_image}_fft_real_7 0 64 496 16 0 1
fslroi adjusted_{$in_image}_fft_real adjusted_{$in_image}_fft_real_8 448 64 496 16 0 1
fslroi adjusted_{$in_image}_fft_imag adjusted_{$in_image}_fft_imag_1 0 64 0 16 0 1
fslroi adjusted_{$in_image}_fft_imag adjusted_{$in_image}_fft_imag_2 448 64 0 16 0 1
fslroi adjusted_{$in_image}_fft_imag adjusted_{$in_image}_fft_imag_3 0 64 16 48 0 1
fslroi adjusted_{$in_image}_fft_imag adjusted_{$in_image}_fft_imag_4 448 64 16 48 0
1
#fslroi adjusted_{$in_image}_fft_imag adjusted_{$in_image}_fft_imag_5 0 64 448 48 0
1
#fslroi adjusted_{$in_image}_fft_imag adjusted_{$in_image}_fft_imag_6 448 64 448 48
0 1

```

```
fslroi adjusted_${in_image}_fft_imag adjusted_${in_image}_fft_imag_7 0 64 496 16 0 1
fslroi adjusted_${in_image}_fft_imag adjusted_${in_image}_fft_imag_8 448 64 496 16
0 1
```

```
fslmerge -x adjusted_${in_image}_fft_real_1_2 adjusted_${in_image}_fft_real_1
adjusted_${in_image}_fft_real_2
fslmerge -x adjusted_${in_image}_fft_real_3_4 adjusted_${in_image}_fft_real_3
adjusted_${in_image}_fft_real_4
#fslmerge -x adjusted_${in_image}_fft_real_5_6 adjusted_${in_image}_fft_real_5
adjusted_${in_image}_fft_real_6
fslswapdim adjusted_${in_image}_fft_real_3_4 -x -y z
adjusted_${in_image}_fft_real_5_6
fslmaths adjusted_${in_image}_fft_real_5_6 -mul 0 adjusted_${in_image}_fft_real_5_6
fslmerge -x adjusted_${in_image}_fft_real_7_8 adjusted_${in_image}_fft_real_7
adjusted_${in_image}_fft_real_8
fslmerge -y adjusted_${in_image}_fft_real_resamp adjusted_${in_image}_fft_real_1_2
adjusted_${in_image}_fft_real_3_4 adjusted_${in_image}_fft_real_5_6
adjusted_${in_image}_fft_real_7_8
```



```

fslmerge -x adjusted_${in_image}_fft_imag_1_2 adjusted_${in_image}_fft_imag_1
adjusted_${in_image}_fft_imag_2

fslmerge -x adjusted_${in_image}_fft_imag_3_4 adjusted_${in_image}_fft_imag_3
adjusted_${in_image}_fft_imag_4

#fslmerge -x adjusted_${in_image}_fft_imag_5_6 adjusted_${in_image}_fft_imag_5
adjusted_${in_image}_fft_imag_6

fslswapdim adjusted_${in_image}_fft_imag_3_4 -x -y z
adjusted_${in_image}_fft_imag_5_6

fslmaths adjusted_${in_image}_fft_imag_5_6 -mul -1
adjusted_${in_image}_fft_imag_5_6

fslmaths adjusted_${in_image}_fft_imag_5_6 -mul -0
adjusted_${in_image}_fft_imag_5_6

fslmerge -x adjusted_${in_image}_fft_imag_7_8 adjusted_${in_image}_fft_imag_7
adjusted_${in_image}_fft_imag_8

fslmerge -y adjusted_${in_image}_fft_imag_resamp
adjusted_${in_image}_fft_imag_1_2 adjusted_${in_image}_fft_imag_3_4
adjusted_${in_image}_fft_imag_5_6 adjusted_${in_image}_fft_imag_7_8


fslcomplex -complex adjusted_${in_image}_fft_real_resamp
adjusted_${in_image}_fft_imag_resamp adjusted_${in_image}_fft_resamp

fslfft adjusted_${in_image}_fft_resamp adjusted_${in_image}_resamp -inv

fslcomplex -realabs adjusted_${in_image}_resamp abs_adjusted_${in_image}

```

```
fslmaths abs_adjusted_${in_image} -div 16 abs_adjusted_${in_image}
```

```
fslchpixmap abs_adjusted_${in_image} $xdim $ydim $zdim
```

```
# imrm sin_2x2x1*
```

```
# rm ${phi}.mat
```

```
imrm pi_1x2x1
```

```
imrm zero_1x2x1
```

APPENDIX C

Script for Estimating Expected Signal in a Diffusion Weighted Image

The script “dwi_sim_EC.sh” is a slight modification of the script with the same name in Appendix B. The script is used to estimate the expected signal of a DTI scan starting with the non-diffusion weighted reference volume, the tensor map of the diffusion tensors as generated by the RESTORE algorithm implemented in Camino, the set of affine matrices used to correct motion and eddy current geometric distortions of the original DTI scan, and the set of diffusion weighting vectors used in acquiring the DTI scan.

```
while read tree;do

    sim_dir=/home/keith/GWS/DWI_void_slice_exclusion/2c/$tree

    if test ! -f $sim_dir/inv_ECmat_vol0000.mat;then

        echo "First run inv_EC_mat.sh for $tree";

        continue;

    fi

    cd $sim_dir

    num=0;

    bvals=(`cat bvals_2c`);

    fslmaths restore_S0 -mul 0 img_0

    fslmaths img_0 -add 1 img_1

    cat bvecs_2c|

        while read -a bvec;do
```

```

vol=dwi_sim_vol`zeropad $num 4`;
vol_EC=dwi_sim_EC_vol`zeropad $num 4`;
vol_tensor=dwi_sim_tensor_vol`zeropad $num 4`;
S0_EC=restore_S0_EC_vol`zeropad $num 4`
mat=ECmat_vol`zeropad $num 4`.mat
bval=${bvals[$num]};
if test $bval -ne 0;then
    bvec_norm=`echo "scale=6;sqrt (${bvec[0]}^2 + ${bvec[1]}^2 +
${bvec[2]}^2)"|bc`;
    b_x=`echo "scale=6;$bval * ${bvec[0]} / $bvec_norm"|bc`;
    b_y=`echo "scale=6;$bval * ${bvec[1]} / $bvec_norm"|bc`;
    b_z=`echo "scale=6;$bval * ${bvec[2]} / $bvec_norm"|bc`;
else
    b_x=0;
    b_y=0;
    b_z=0;
fi;
vecreg -i restore_tensor -o EC_tensor -r dti2clas -t inv_$mat
fslmaths img_1 -mul $b_x bvec_x;
fslmaths img_1 -mul $b_y bvec_y;
fslmaths img_1 -mul $b_z bvec_z;
fslmerge -t bvec_1 bvec_x bvec_y bvec_z
flirt -in restore_S0 -ref dti2clas -out $S0_EC -applyxfm -init inv_$mat

```

```

fslsplit EC_tensor EC_tensor -t

fslmerge -t EC_tensor_1 EC_tensor0000 EC_tensor0001 EC_tensor0002
fslmerge -t EC_tensor_2 EC_tensor0001 EC_tensor0003 EC_tensor0004
fslmerge -t EC_tensor_3 EC_tensor0002 EC_tensor0004 EC_tensor0005


fslmaths EC_tensor_1 -mul bvec_1 -Tmean -mul 3 -sqr btensor1_2
fslmaths EC_tensor_2 -mul bvec_1 -Tmean -mul 3 -sqr btensor2_2
fslmaths EC_tensor_3 -mul bvec_1 -Tmean -mul 3 -sqr btensor3_2


fslmaths btensor1_2 -add btensor2_2 -add btensor3_2 -sqrt -mul -1000000 -exp -mul
$S0_EC $vol_tensor


num=`expr $num + 1`;
# test $num -gt 5 && exit;

done


images=`imglob restore_S0_EC_vol????*`

fslmerge -t restore_S0_EC $images

imrm $images


images=`imglob dwi_sim_tensor_vol????*`

```

```
fslmerge -t dwi_sim_restore_tensor $images
```

```
imrm $images
```

```
done
```

APPENDIX D

Scripts for Detecting Vibration-Induced Signal Void Artifacts

The script called “dtifit_regressor.sh” is used to apply the co-regressor defined by Gallichan as the tensors are fit using the DTIFIT algorithm of FSL. The influence of the co-regressor at each voxel is used to generate a preliminary mask of the voxels affected by the vibration artifact.

```
while read tree;do

    data_dir=/home/keith/GWS/DWI_void_slice_exclusion/2c/$tree

    sim_dir=/home/keith/GWS/Results/signal_void_detection/vibration/2c/$tree

    if test ! `imtest $data_dir/dti2cEC` ;then

        echo "First run copy_raw_data.sh for $tree";

        continue;

    fi;

    mkdir -p $sim_dir

    cd $sim_dir;

    cat $data_dir/bvecs_2c|while read -a bvec;do

        vec_norm=`echo "scale=8;sqrt(${bvec[0]}^2+${bvec[1]}^2+${bvec[2]}^2)"|bc -l`

        if test `echo "$vec_norm < 0.01"|bc` = 1 ;then

            vib_regressor=1;

        else

            vec_x=`echo "scale=8;${bvec[0]}/$vec_norm"|bc -l`

            if test `echo "$vec_x < 0.61"|bc` = 1 ;then
```

```

vib_regressor=1;

else

vib_regressor=`echo "scale=8;(c(4*a(1)*(sqrt($vec_x^2)-0.61)/1.08))^2"|bc -l`

fi;

fi;

echo $vib_regressor

done>vib_regressor

dtifit -k $data_dir/dti2cEC -o vib_regr -m $data_dir/dti2cEC_brain_mask -r
$data_dir/bvecs_2c -b $data_dir/bvals_2c --sse --cni=vib_regressor;

fslmaths vib_regr_cnicope -mul -1 -thr .3 -bin -kernel 2D -ero -dilM -bin -mul -1 -add 1
vib_reg_mask;

done;

```


The script called “regressor_design.sh” computes the average of the ratios of the measured signals to the expected signals for each diffusion direction. The slope of the decrease of the average ratios as the x component of the diffusion direction increases is calculated.

```
while read tree;do

    echo $tree

    data_dir=/home/keith/GWS/DWI_void_slice_exclusion/2c/$tree

    regress_dir=/home/keith/GWS/Results/signal_void_detection/vibration/2c/$tree

    mkdir -p $regress_dir

    cd $regress_dir

    cp $data_dir/bvecs_2c_rot_trans ./
    cp $data_dir/bvecs_2c_rot_trans ./
    cp $data_dir/bvecs_2c_rot_trans ./
    cp $data_dir/bvals_2c ./

    fslmaths vib_regr_cnicope -mul -1 -thr .5 -bin -kernel 2D -ero -dilM -bin -mul -1 -add 1
vib_reg_mask;

    fslmaths vib_reg_mask -mul -1 -add 1 -roi 0 128 0 128 2 60 0 1 vib_reg_mask_ero

    fslmaths $data_dir/dti2cEC -div $data_dir/dwi_sim_restore_tensor -mas
vib_reg_mask_ero reduction -odt float

    fsl2ascii reduction reduction
```

```

b_x=(`head -1 bvecs_2c_rot_trans|tail -1`)
b_y=(`head -2 bvecs_2c_rot_trans|tail -1`)
b_z=(`head -3 bvecs_2c_rot_trans|tail -1`)
bvals=(`cat bvals_2c`)

for ((i=0;i<${#bvals[@]};i++));do

    b_norm[i]=`echo "scale=12;sqrt(${b_x[i]} ^ 2 + ${b_y[i]} ^ 2 + ${b_z[i]} ^ 2)"|bc`

    b_norm[i]=`echo "scale=12; if ( ${b_norm[i]} ) ${b_norm[i]} else 1"|bc`

done

sumX=0

sumY=0

sumXY=0

sumXX=0

N=0

# for ((i=0;i<2;i++));do

for ((i=0;i<${#bvals[@]};i++));do

    r_x=`echo "12 k ${b_x[i]} ${b_norm[i]} / p"|sed s/-//|dc`

    vol=`zeropad $i 5`

    num=0

    sum=0

    cat reduction$vol|grep "[1-9]">temp$vol

    while read -a samples;do

        for ((j=0;j<${#samples[@]};j++));do

            if ! test ${samples[j]} = 0;then

```

```

        num=`expr $num + 1`

        sum=`echo "8 k $sum ${samples[$j]} + p"|dc`

    fi

done

done<temp$vol

rm temp$vol

if test $num != 0;then

    average=`echo "8 k $sum $num / p"|dc`

    echo "$r_x $average"

fi

done>r_x_average.txt

cat r_x_average.txt|sort -r| while read r_x average;do

    N=`expr $N + 1`;

    sumX=`echo "8 k $sumX $r_x + p"|dc`;

    sumY=`echo "8 k $sumY $average + p"|dc`;

    sumXX=`echo "8 k $sumXX $r_x $r_x * + p"|dc`;

    sumXY=`echo "8 k $sumXY $r_x $average * + p"|dc`;

    if test `echo "scale=5;if ($average > 1.0) 1 else 0"|bc` = 1; then

        exit;

    elif test $N -gt 2;then

        slope=`echo "8 k $N $sumXY * $sumX $sumY * - $N $sumXX *

$sumX $sumX * - / p"|dc`;

        intercept=`echo "8 k $sumY $slope $sumX * - $N / p"|sed s/-/_/|dc`;

```

```
        echo "N = $N slope = $slope intercept =  
$intercept">regressor_${tree}.txt  
        fi;  
    done;  
  
    rm reduction0*  
  
done
```

The script called “collect_regressors.sh” generates the scan specific co-regressor to be used with the DTIFIT algorithm of FSL to refine the mask of the voxels affected by the vibration artifact.

```
while read tree;do

  if test -e $tree/regressor_${tree}.txt;then

    slope=`cat $tree/regressor_${tree}.txt|awk '{print $6}'`;

    intercept=`cat $tree/regressor_${tree}.txt|awk '{print $9}'`;

    slope=`echo $slope|sed s/_/_/`;

    intercept=`echo $intercept|sed s/_/_/`;

    a=`echo "8 k 1 $intercept - $slope / p"|dc`;

    a_=`echo $a|sed s/_/_/`;

    b=`echo "8 k 0 $intercept - $slope / $a_ - p"|dc`;

    echo $tree $intercept $slope $a $b

    if test `echo "scale=8; if ($a > .5 && $a < 1.0) 1 else 0"|bc` = 1;then

      echo $tree

      echo -n "">$tree/x_regressor

      cat $tree/r_x_average.txt| while read r_x average;do

        echo `echo "scale=8; if ($r_x < $a) 1 else c(3.14159 * ($r_x - $a)/(2 * $b)) ^ 2"|bc`

      -l`>>$tree/x_regressor

      done;

    fi;

  fi;
```

done

APPENDIX E

Scripts for Detecting Other Signal Void Artifacts

The script called “compare_dti2c_2_sim_robust_zscores_dim4.sh” is used to generate a robust z score for each slice of each volume in a DTI scan. The z score reflects how the maximum difference of the expected and measured signal in a slice compares to other volumes at the same slice level. The script requires as input a DTI scan before eddy current correction and an image of the expected signal levels for the scan. The vibration artifact mask and a brain mask, both registered to the original data, are also required.

```
while read tree;do

    data_dir=/home/keith/GWS/DWI_void_slice_exclusion/2c/$tree

    sim_dir=/home/keith/GWS/Results/signal_void_detection/other/2c/$tree

    vib_dir=/home/keith/GWS/Results/signal_void_detection/vibration/2c/$tree

    if ! test `imtest $data_dir/dwi_sim_restore_tensor` = 1;then

        echo "First run dwi_sim_EC.sh for $tree";

        continue;

    fi

    if ! test `imtest $vib_dir/vib_mask_dwi` = 1;then

        echo "No vibration mask for $tree";

        continue

    fi

    mkdir -p $sim_dir

    cd $sim_dir
```

```

dim1=`fslsize $data_dir/dti2clas |grep "\bdim1\b"|awk '{print $2}'`
dim2=`fslsize $data_dir/dti2clas |grep "\bdim2\b"|awk '{print $2}'`
dim3=`fslinfo $data_dir/dti2clas |grep "\bdim3\b"|awk '{print $2}'`
dim4=`fslinfo $data_dir/dti2clas |grep "\bdim4\b"|awk '{print $2}'`

num_b0=`expr $dim4 / 56 \* 6`

num_dwi=`expr $dim4 / 56 \* 50`

fslmaths $data_dir/adj_brain_mask -mas $vib_dir/vib_mask_dwi -kernel 2D -ero -ero
adj_brain_mask

fslmaths adj_brain_mask -Xmean -Ymean adj_brain_mask_XYmean

fslsplit $data_dir/diff_adj_brain vol

fslsplit adj_brain_mask maskvol

for ((i=0;i<$dim4;i++));do

    vol_num=`zeropad $i 4`

    fslsplit vol$vol_num slice -z

    fslsplit maskvol$vol_num maskslice -z

    pctl_95=(`for ((i=0;i<64;i++));do echo 0;done`)

    for ((j=0;j<$dim3;j++));do

        slice_num=`zeropad $j 4`

        pctl_95[$j]=`fslstats slice$slice_num -k maskslice$slice_num -p 95`

    done

    echo ${pctl_95[@]}

done>diff_pctl_95.$tree

imrm vol*

```



```

imrm maskvol*

imrm slice*

imrm maskslice*

for ((i=0;i<$dim3;i++));do

    while read -a pctl_95;do

        echo -n "${pctl_95[i]} "

    done<diff_pctl_95.$tree

    echo ""

done>diff_pctl_95_trans.$tree

fslasciizimg diff_pctl_95_trans.$tree 1 1 $dim3 $dim4 2 2 2 8.3 diff_pctl_95.nii.gz

```

```

min_mean=`fslstats diff_pctl_95 -R|awk '{print $1}'`

offset=`echo "score=0;2 * sqrt($min_mean^2)/1"|bc`

b0_perc_adj=`fslstats $data_dir/b0_mask_XYmean -m`

b0_perc_25=`echo "100 - 75 * $b0_perc_adj"|bc`

b0_perc_50=`echo "100 - 50 * $b0_perc_adj"|bc`

b0_perc_75=`echo "100 - 25 * $b0_perc_adj"|bc`

dwi_perc_adj=`fslstats $data_dir/dwi_mask_XYmean -m`

dwi_perc_25=`echo "100 - 75 * $dwi_perc_adj"|bc`

```

```

dwi_perc_50=`echo "100 - 50 * $dwi_perc_adj"|bc`

dwi_perc_75=`echo "100 - 25 * $dwi_perc_adj"|bc`

# robust z scores for pctl_95 of dwi_sim_restore_tensor-dti2clas

fslmaths diff_pctl_95 -add $offset -mas $data_dir/b0_mask_XYmean -Tperc
$b0_perc_50 -sub $offset diff_pctl_95_b0mask_XYmean_Tmedian

fslmaths diff_pctl_95 -add $offset -mas $data_dir/b0_mask_XYmean -Tperc
$b0_perc_25 -sub $offset diff_pctl_95_b0mask_XYmean_Tperc_25

fslmaths diff_pctl_95 -add $offset -mas $data_dir/b0_mask_XYmean -Tperc
$b0_perc_75 -sub $offset diff_pctl_95_b0mask_XYmean_Tperc_75

fslmaths diff_pctl_95_b0mask_XYmean_Tperc_75 -sub
diff_pctl_95_b0mask_XYmean_Tperc_25 -mul 0.7413
diff_pctl_95_b0mask_XYmean_robust_stdev

fslmaths diff_pctl_95 -sub diff_pctl_95_b0mask_XYmean_Tmedian -div
diff_pctl_95_b0mask_XYmean_robust_stdev
diff_pctl_95_b0mask_XYmean_robust_zscore


fslmaths diff_pctl_95 -add $offset -mas $data_dir/dwi_mask_XYmean -Tperc
$dwi_perc_50 -sub $offset diff_pctl_95_dwimask_XYmean_Tmedian

fslmaths diff_pctl_95 -add $offset -mas $data_dir/dwi_mask_XYmean -Tperc
$dwi_perc_25 -sub $offset diff_pctl_95_dwimask_XYmean_Tperc_25

fslmaths diff_pctl_95 -add $offset -mas $data_dir/dwi_mask_XYmean -Tperc
$dwi_perc_75 -sub $offset diff_pctl_95_dwimask_XYmean_Tperc_75

```

```

fslmaths diff_pctl_95_dwimask_XYmean_Tperc_75 -sub
diff_pctl_95_dwimask_XYmean_Tperc_25 -mul 0.7413
diff_pctl_95_dwimask_XYmean_robust_stdev

fslmaths diff_pctl_95 -sub diff_pctl_95_dwimask_XYmean_Tmedian -div
diff_pctl_95_dwimask_XYmean_robust_stdev
diff_pctl_95_dwimask_XYmean_robust_zscore


fsl2ascii diff_pctl_95_b0mask_XYmean_robust_zscore
diff_pctl_95_b0mask_XYmean_robust_zscore

diff_filenames=(`ls diff_pctl_95_b0mask_XYmean_robust_zscore0*`)

fsl2ascii adj_brain_mask_XYmean adj_brain_mask_XYmean
mask_filenames=(`ls adj_brain_mask_XYmean0*`)

echo -n "">b0mask_pctl_95_robust_zscores.txt

for ((j=0+3;j<${num_b0}+3;j++));do

    i=`expr $j / 6 \* 56 + $j % 6 - 3`;

    cat ${diff_filenames[$i]}|awk 'NF > 0 {ORS=" ";print
$1}'>>b0mask_pctl_95_robust_zscores.txt;

    for ((k=${dim3};k<65;k++));do echo -n "0
">>b0mask_pctl_95_robust_zscores.txt;done;

    cat ${mask_filenames[$i]}|awk 'NF > 0 {ORS=" ";print
$1}'>>b0mask_pctl_95_robust_zscores.txt;

```

```

    for ((k=$dim3;k<65;k++));do echo -n "0
">>b0mask_pctl_95_robust_zscores.txt;done;

    echo "${tree:0:7}vol`zeropad $i 4`">>b0mask_pctl_95_robust_zscores.txt;

done;

rm ${diff_filenames[@]};

rm ${mask_filenames[@]};


fsl2ascii diff_pctl_95_dwimask_XYmean_robust_zscore
diff_pctl_95_dwimask_XYmean_robust_zscore

diff_filenames=(`ls diff_pctl_95_dwimask_XYmean_robust_zscore0*`)

fsl2ascii adj_brain_mask_XYmean adj_brain_mask_XYmean

mask_filenames=(`ls adj_brain_mask_XYmean0*`)

echo -n "">dwimask_pctl_95_robust_zscores.txt

for ((j=0;j<${num_dwi};j++));do

    i=`expr $j / 50 \* 56 + $j % 50 + 3`;

    cat ${diff_filenames[$i]}|awk 'NF > 0 {ORS=" ";print
$1}'>>dwimask_pctl_95_robust_zscores.txt;

    for ((k=$dim3;k<65;k++));do echo -n "0

">>dwimask_pctl_95_robust_zscores.txt;done;

    cat ${mask_filenames[$i]}|awk 'NF > 0 {ORS=" ";print
$1}'>>dwimask_pctl_95_robust_zscores.txt;

    for ((k=$dim3;k<65;k++));do echo -n "0

">>dwimask_pctl_95_robust_zscores.txt;done;

```

```
    echo "${tree:0:7}vol`zeropad $i 4`">>dwimask_pctl_95_robust_zscores.txt;

done;

rm ${diff_filenames[@]};

rm ${mask_filenames[@]};

done
```

The script called “generate_motion_mask.sh” produces a 4D artifact mask for a DTI scan. Each slice with an artifact z score greater than the specified threshold is rendered with a value of 1 and all other slices are given a 0.

```
while read tree thr;do

    sim_dir=/home/keith/GWS/DWI_void_slice_exclusion/2c/$tree

    detect_dir=/home/keith/GWS/Results/signal_void_detection/other/2c/$tree

    max_slices=65;

    max_slices2=130;

    if test ! -e $detect_dir/diff_pctl_95_trans.$tree;then

        echo "First run compare_dti2c_2_sim_zscores_dim4.sh for $tree";

        continue;

    fi

    cd $detect_dir

    for ((i=0;i<$max_slices;i++));do

        min_area[$i]=1;

    done

    while read -a zscores;do

        for ((i=$max_slices;i<$max_slices2;i++));do

            j=`expr $i - $max_slices`;

            if test _${zscores[$i]}%e* } != _${zscores[$i]};then zscores[$i]=0;fi;

            if test `echo "${zscores[$i]} < ${min_area[$j]}"|bc` = 1 ;then

min_area[$j]=${zscores[$i]};fi;
```

```

done

done<dwimask_pctl_95_robust_zscores.txt

num_vols=`wc dwimask_pctl_95_robust_zscores.txt|awk '{print $1}'`

for ((i=0;i<$num_vols;i++));do

    vol_slices[$i]="";

done

vol=0;

while read -a zscores;do

    for ((i=0;i<$max_slices;i++));do

        j=`expr $i - 0`;

        if test _${zscores[$i]%e*} != _${zscores[$i]};then zscores[$i]=0;fi;

        if test `echo "${zscores[$i]} > $thr"|bc` = 1 -a `echo "${min_area[$j]} > .03"|bc` =
1;then

            vol_slices[$vol]="${vol_slices[$vol]} `zeropad $j 3`";

        fi;

    done;

    vol=`expr $vol + 1`;

done<dwimask_pctl_95_robust_zscores.txt

fslmaths $sim_dir/dti2clas -mul 0 artifact_mask -odt short

fslroi artifact_mask ones_mask 0 1

fslmaths ones_mask -add 1 ones_mask

fslsplit ones_mask ones_mask_slice -z

fslsplit artifact_mask artifact_mask_vol

```

```

mask_vols=`imglob artifact_mask_vol0*`

for ((i=0;i<num_vols;i++));do

    slices=(${vol_slices[$i]});

    if test _${slices[0]} != _ ;then

        vol_num=`expr $i / 50 \* 56 + $i % 50 + 3`;

        vol_num=`zeropad $vol_num 4`

        echo ${tree}vol$vol_num ${slices[@]};

        fslsplit artifact_mask_vol$vol_num temp_vol_slice -z;

        slice_files=`imglob temp_vol_slice0*`

        for ((j=0;j<${#slices[@]};j++));do

            imrm temp_vol_slice`zeropad ${slices[$j]} 4`;

            imcp ones_mask_slice`zeropad ${slices[$j]} 4` temp_vol_slice`zeropad
${slices[$j]} 4`;

        done

        imrm artifact_mask_vol$vol_num

        fslmerge -z artifact_mask_vol$vol_num $slice_files

        imrm $slice_files

    fi

done>motion_vol_slices_${thr}.txt

fslmerge -t artifact_mask_${thr} $mask_vols

imrm $mask_vols

ones_mask=`imglob ones_mask*`

imrm $ones_mask

```


done

The script called “artifact_mask_2_EC.sh” applies the eddy current and motion geometric corrections to the artifact masks to account for all image voxels which have influence from artifacts.

```
while read tree thr;do

    sim_dir=/home/keith/GWS/DWI_void_slice_exclusion/2c/$tree

    detect_dir=/home/keith/GWS/Results/signal_void_detection/other/2c/$tree

    if test ! -f $sim_dir/inv_ECmat_vol0000.mat;then

        echo "First run inv_EC_mat.sh for $tree";

        continue;

    fi

    cd $detect_dir

    fslsplit artifact_mask_${thr} artifact_mask_vol

    dim4=`fslinfo $sim_dir/dti2clas|grep "\bdim4\b"|awk '{print $2}'`

    for ((num=0;num<$dim4;num++));do

        vol=vol`zeropad $num 4`;

        mat=$sim_dir/ECmat_vol`zeropad $num 4`.mat

        flirt -in artifact_mask_${vol} -ref $sim_dir/dti2cEC -out artifact_mask_EC_${vol} -

    applyxfm -init $mat

    done

    imrm artifact_mask_vol*

    mask_list=`imglob artifact_mask_EC_vol*`

    fslmerge -t artifact_mask_${thr}_EC $mask_list
```

imrm \$mask_list

done

The script called “set_vols_4_slice.sh” lists all volumes at each slice of a DTI scan which are flagged as being contaminated with signal void artifacts. A list of all combinations of excluded volumes is also generated.

```
while read tree thr;do

sim_dir=/home/keith/GWS/DWI_void_slice_exclusion/2c/$tree

detect_dir=/home/keith/GWS/Results/signal_void_detection/other/2c/$tree

cd $detect_dir

fslmaths artifact_mask_${thr}_EC -bin artifact_mask_EC_bin

fslmaths artifact_mask_EC_bin -Xmean -Ymean -bin artifact_mask_EC_bin_XY

fsl2ascii artifact_mask_EC_bin_XY artifact_mask_EC_bin_XY

dim3=`fslinfo $sim_dir/dti2clas|grep "\bdim3\b"|awk '{print $2}'`

dim4=`fslinfo $sim_dir/dti2clas|grep "\bdim4\b"|awk '{print $2}'`

for ((i=0;i<$dim4;i++));do

vol=`zeropad $i 5`

slices=(`cat artifact_mask_EC_bin_XY$vol|grep .|awk '{ORS=" ";print $1}'`)

for ((j=0;j<$dim3;j++));do

if test ${slices[$j]} = 1;then

slice_vols[$j]="${slice_vols[$j]} `zeropad $i 3`"

fi

done

done

for ((j=0;j<$dim3;j++));do
```

```
    echo $j ${slice_vols[$j]}  
done>slice_vols_$thr  
for ((j=0;j<$dim3;j++));do  
    echo ${slice_vols[$j]}  
done|grep .|sort -u >vol_combinations_$thr  
rm artifact_mask_EC_bin_XY0*  
done
```

A second script called “set_vols_4_slice.sh” (same name as above but a modified script) adds the volumes affected by the vibration artifact to the volumes to be removed for each slice.

```
while read tree thr;do

    detect_dir=/home/keith/GWS/Results/signal_void_detection/other/2c/$tree
    vib_dir=/home/keith/GWS/Results/signal_void_detection/vibration/2c/$tree
    cd $vib_dir

    regressor=(`cat x_regressor`)
    excl_vols=""

    for ((i=0;i<${#regressor[@]};i++));do
        if ! test ${regressor[$i]} = 1;then
            excl_vols="$excl_vols `zeropad $i 3`"
        fi;
    done;

    while read slice slice_vols;do

        vols=(`echo "$slice_vols $excl_vols"|tr " " "\n"|sort -u`)

        echo "$slice ${vols[@]}"

    done<${detect_dir/slice_vols_$thr|tee slice_vols_$thr|

        while read slice slice_vols;do

            echo $slice_vols;
```

```
done|grep .|sort -u >vol_combinations_$thr
```

```
done
```

APPENDIX F

Scripts for Removing Signal Void Artifacts

The script called “dtifit_combinations.sh” calculates an FA map for each slice of the DTI scan using only the data which is not affected by the signal void artifacts.

```
while read tree thr;do

sim_dir=/home/keith/GWS/DWI_void_slice_exclusion/2c/$tree

vib_dir=/home/keith/GWS/Results/signal_void_detection/vibration/2c/$tree

cd $vib_dir

imrm dti2cEC_vol*

imrm dti2cEC_wo*

rm bvals_wo*

rm bvecs_wo*

fslroi $sim_dir/dti2cEC img_1 0 1

fslmaths img_1 -mul 0 -add 1 img_1

dtifit -k $sim_dir/dti2cEC -o dti2cEC_wo -m img_1 -r $sim_dir/bvecs_2c_rot -b

$sim_dir/bvals_2c --sse

dim4=`fslinfo $sim_dir/dti2clas|grep "\bdim4\b"|awk '{print $2}'`

fslsplit $sim_dir/dti2cEC dti2cEC_vol

cat vol_combinations_${thr}|while read -a vols;do

name=""

lastvol=-1

echo -n "">temp_bvecs
```



```

echo -n "">temp_bvals

for ((i=0;i<${#vols[@]};i++));do

    vol=`zeropad ${vols[$i]} 4`

    immv dti2cEC_vol$vol hold_dti2cEC_vol$vol

    name="${name}-${vol}"

    head -$vol $sim_dir/bvecs_2c_rot |tail -`expr $vol - $lastvol - 1`>>temp_bvecs

    head -$vol $sim_dir/bvals_2c |tail -`expr $vol - $lastvol - 1`>>temp_bvals

    lastvol=$vol

done

vol=$dim4

head -$vol $sim_dir/bvecs_2c_rot |tail -`expr $vol - $lastvol - 1`>>temp_bvecs

mv temp_bvecs bvecs_wo$name

head -$vol $sim_dir/bvals_2c |tail -`expr $vol - $lastvol - 1`>>temp_bvals

mv temp_bvals bvals_wo$name

images=`imglob dti2cEC_vol*`

fslmerge -t dti2cEC_wo$name $images

dtifit -k dti2cEC_wo$name -o dti2cEC_wo$name -m img_1 -r bvecs_wo$name -b
bvals_wo$name --sse

for ((i=0;i<${#vols[@]};i++));do

    vol=`zeropad ${vols[$i]} 4`

    immv hold_dti2cEC_vol$vol dti2cEC_vol$vol

done

done

```

```
images=`imglob dti2cEC_vol*`  
imrm $images  
done
```

The script called “FA_combinations_merge.sh” selects the slices from the FA maps generated by “dtifit_combinations.sh” which have no contribution from the corrupted data and combines them into a single FA map.

```
while read tree thr;do

    sim_dir=/home/keith/GWS/DWI_void_slice_exclusion/2c/$tree

    vib_dir=/home/keith/GWS/Results/signal_void_detection/vibration/2c/$tree

    cd $vib_dir

    fslsplit dti2cEC_wo_FA dti2cEC_wo_FA_slice -z

    cat vol_combinations_${thr}|while read -a vols;do

        name=""

        for ((i=0;i<${#vols[@]};i++));do

            vol=`zeropad ${vols[$i]} 4`

            name="${name}-${vol}"

        done

        fslsplit dti2cEC_wo_${name}_FA dti2cEC_wo_${name}_FA_slice -z

    done

    cat slice_vols_${thr}|while read -a slices;do

        slice=`zeropad ${slices[0]} 4`

        name=""

        for ((i=1;i<${#slices[@]};i++));do
```

```

    vol=`zeropad ${slices[$i]} 4`

    name="${name}-${vol}"

done

if test _${slices[1]} != _;then

    imrm dti2cEC_wo_FA_slice$slice

    immv dti2cEC_wo${name}_FA_slice$slice dti2cEC_wo_FA_slice$slice

fi

done

images=`imglob dti2cEC_wo_FA_slice*`

fslmerge -z dti2c_corr_${thr}_FA $images

imrm $images

cat vol_combinations_${thr}|while read -a vols;do

    name=""

    for ((i=0;i<${#vols[@]};i++));do

        vol=`zeropad ${vols[$i]} 4`

        name="${name}-${vol}"

    done

    imrm dti2cEC_wo${name}_FA_slice*

done

done

```

The script called “void_combinations_merge.sh” combines the FA map that was generated after excluding data flagged for signal void artifacts with the FA map that was generated after excluding both the data flagged for signal void artifacts and the data from volumes affected by the vibration artifact.

```
while read tree thr;do

    detect_dir=/home/keith/GWS/Results/signal_void_detection/other/2c/$tree
    vib_dir=/home/keith/GWS/Results/signal_void_detection/vibration/2c/$tree
    cd $vib_dir

    fslmaths vib_refine.5_mask -mul -1 -add 1 -mul dti2c_corr_${thr}_FA
    dti2c_corr_${thr}_FA_mask

    fslmaths vib_refine.5_mask -mul $detect_dir/dti2c_corr_${thr}_FA -add
    dti2c_corr_${thr}_FA_mask dti2c_corr_${thr}_FA_combined

done
```

APPENDIX G

Scripts for Quantifying FA Changes of Simulated DTI Scan

The script “adj_brain_mask.sh” is used to adjust the brain mask by removing regions of non-diffusion weighted signal greater than two standard deviations above the mean. This is to remove the ventricles and areas with signal pile-up from the assessment of FA changes.

```
sig=24.0

vib_dir=/home/keith/GWS/Results/simulation/detect/vibration

sim_dir=/home/keith/GWS/Results/simulation/vib_art

sim_scan=$sim_dir/motion_adjusted_dwi_vib_cardiac_sim_$sig

fslroi $sim_scan img_0 0 1

fslmaths img_0 -mul 0 img_0

fslmaths img_0 -add 1 img_1

dim1=`fslsize $sim_scan |grep "\bdim1\b"|awk '{print $2}'`

dim2=`fslsize $sim_scan |grep "\bdim2\b"|awk '{print $2}'`

dim3=`fslinfo $sim_scan |grep "\bdim3\b"|awk '{print $2}'`

dim4=`fslinfo $sim_scan |grep "\bdim4\b"|awk '{print $2}'`

num_b0=`expr $dim4 / 56 \* 6`

num_dwi=`expr $dim4 / 56 \* 50`
```

```

b0_mask_files=`for ((i=0;i<3;i++));do echo -n "img_1 ";done;for ((i=0;i<50;i++));do
echo -n "img_0 ";done;for ((i=0;i<6;i++));do echo -n "img_1 ";done;for
((i=0;i<50;i++));do echo -n "img_0 ";done;for ((i=0;i<6;i++));do echo -n "img_1
";done;for ((i=0;i<50;i++));do echo -n "img_0 ";done;for ((i=0;i<6;i++));do echo -n
"img_1 ";done;for ((i=0;i<50;i++));do echo -n "img_0 ";done;for ((i=0;i<6;i++));do echo
-n "img_1 ";done;for ((i=0;i<50;i++));do echo -n "img_0 ";done;for ((i=0;i<6;i++));do
echo -n "img_1 ";done;for ((i=0;i<50;i++));do echo -n "img_0 ";done;for
((i=0;i<3;i++));do echo -n "img_1 ";done;`;

fslmerge -t b0_mask $b0_mask_files;

fslroi b0_mask b0_mask 0 $dim4

dwi_mask_files=`for ((i=0;i<3;i++));do echo -n "img_0 ";done;for ((i=0;i<50;i++));do
echo -n "img_1 ";done;for ((i=0;i<6;i++));do echo -n "img_0 ";done;for
((i=0;i<50;i++));do echo -n "img_1 ";done;for ((i=0;i<6;i++));do echo -n "img_0
";done;for ((i=0;i<50;i++));do echo -n "img_1 ";done;for ((i=0;i<6;i++));do echo -n
"img_0 ";done;for ((i=0;i<50;i++));do echo -n "img_1 ";done;for ((i=0;i<6;i++));do echo
-n "img_0 ";done;for ((i=0;i<50;i++));do echo -n "img_1 ";done;for ((i=0;i<6;i++));do
echo -n "img_0 ";done;for ((i=0;i<50;i++));do echo -n "img_1 ";done;for
((i=0;i<3;i++));do echo -n "img_0 ";done;`;

fslmerge -t dwi_mask $dwi_mask_files;

fslroi dwi_mask dwi_mask 0 $dim4

fslmaths b0_mask -Xmean -Ymean b0_mask_XYmean -odt float;

fslmaths b0_mask -Xmean -Ymean -Zmean b0_mask_XYZmean -odt float;

fslmaths b0_mask_XYmean -Tmean b0_mask_XYmean_Tmean;

```

```
fslmaths dwi_mask -Xmean -Ymean dwi_mask_XYmean -odt float;
```

```
fslmaths dwi_mask -Xmean -Ymean -Zmean dwi_mask_XYZmean -odt float;
```

```
fslmaths dwi_mask_XYmean -Tmean dwi_mask_XYmean_Tmean;
```

```
fslmaths dwi_sim_restore_S0 -mas dwi_brain_mask dwi_sim_S0_brain
```

```
fslmaths dwi_brain_mask -Xmean -Ymean -Zmean dwi_brain_mask_XYZmean;
```

```
fslmaths dwi_sim_S0_brain -Xmean -Ymean -Zmean -div dwi_brain_mask_XYZmean  
dwi_sim_S0_brain_XYZmean;
```

```
fslmaths dwi_sim_S0_brain_XYZmean -sqr dwi_sim_S0_brain_XYZmean2;
```

```
fslmaths dwi_sim_S0_brain -sqr -Xmean -Ymean -Zmean -div  
dwi_brain_mask_XYZmean -sub dwi_sim_S0_brain_XYZmean2 -sqrt  
dwi_sim_S0_brain_XYZstd;
```

```
fslmaths dwi_sim_S0_brain_XYZstd -mul 2.0 -add dwi_sim_S0_brain_XYZmean  
dwi_sim_S0_brain_XYZ2z;
```

```
b0_thr=`fslstats dwi_sim_S0_brain_XYZ2z -k b0_mask_XYZmean -m`;
```

```
dwi_thr=`fslstats dwi_sim_S0_brain_XYZ2z -k dwi_mask_XYZmean -m`;
```

```
fslmaths dwi_sim_S0_brain -thr $b0_thr -bin -mul -1 -add 1 -mas b0_mask -mul  
dwi_brain_mask b0_adj_brain_mask
```

```
fslmaths dwi_sim_S0_brain -thr $dwi_thr -bin -mul -1 -add 1 -mas dwi_mask -mul  
dwi_brain_mask dwi_adj_brain_mask
```



```
fslmaths b0_adj_brain_mask -add dwi_adj_brain_mask adj_brain_mask
```

The script called “make_FA_tissue_mask.sh” applies the eddy current geometric correction to the brain mask adjusted with the script “adj_brain_mask.sh” above and makes a mask of voxels included in all diffusion weighted volumes. It then removes regions from the FA mask which have mean diffusivity less than one half of the average mean diffusivity, thus removing any remaining non-tissue voxels.

```
sim_dir=/home/keith/GWS/Results/simulation/detect
sim_scan=$sim_dir/motion_vib_cardiac_sim_24.0_EC
fslsplit $sim_dir/adj_brain_mask adj_brain_mask_vol
dim4=`fslinfo $sim_scan|grep "\bdim4\b"|awk '{print $2}'`
for ((num=0;num<$dim4;num++));do
    vol=vol`zeropad $num 4`;
    mat=$sim_dir/mat/ECmat_vol`zeropad $num 4`.mat
    flirt -in adj_brain_mask_$vol -ref $sim_scan -out adj_brain_mask_EC_$vol -
applyxfm -init $mat
done
mask_list=`imglob adj_brain_mask_vol*`
mask_EC_list=`imglob adj_brain_mask_EC_vol*`
fslmerge -t FA_tissue_mask $mask_EC_list
MD_mean=`fslstats $sim_dir/dwi_sim_EC_wo_MD -M`
MD_stdev=`fslstats $sim_dir/dwi_sim_EC_wo_MD -S`
MD_5z=`dc -e "5 k $MD_mean $MD_stdev 5 * - p"``
```

```
MD_2=`dc -e "5 k $MD_mean 2 / p"`  
fslmaths FA_tissue_mask -Tmean -thr 1 -bin -mul $sim_dir/dwi_sim_EC_wo_MD -  
thr $MD_2 -bin FA_tissue_mask  
imrm $mask_list  
imrm $mask_EC_list  
echo "$MD_mean $MD_stdev $MD_5z $MD_2"
```

The script called “max_FA_diff.sh” calculates the robust maximum for each slice of FA differences within the FA tissue mask. The FA differences calculated are between the FA map used to generate the simulations and the three simulations (no motion effect, corrupted with signal void from motion effect, and corrupted simulation adjusted by removal of detected signal void). The FA differences were also calculated between each of the three simulations.

```
thr=5.0;
```

```
compare_FA_dir=/home/keith/GWS/Results/simulation/compare_output
```

```
true_FA_dir=/home/keith/GWS/Results/simulation
```

```
sim_FA_dir=/home/keith/GWS/Results/simulation/simulate_zero_motion_artifacts
```

```
corr_FA_dir=/home/keith/GWS/Results/simulation/vib_art
```

```
detect_dir=/home/keith/GWS/Results/simulation/detect/vibration
```

```
true_FA=$true_FA_dir/dti2c_fit_FA
```

```
sim_FA=$sim_FA_dir/motion_adjusted_dwi_sim_24.0_fit_FA
```

```
corr_FA=$corr_FA_dir/motion_vib_cardiac_sim_24.0_EC_fit_FA
```

```
detect_FA=$detect_dir/dwi_sim_corr_${thr}_FA_combined
```

```
fslmaths $true_FA -sub $detect_FA -abs true_detect_abs
```

```
fslmaths $true_FA -sub $sim_FA -abs true_sim_abs
```

```
fslmaths $true_FA -sub $corr_FA -abs true_corr_abs
```

```
fslmaths $sim_FA -sub $detect_FA -abs sim_detect_abs
```

```
fslmaths $sim_FA -sub $corr_FA -abs sim_corr_abs
```

```
fslmaths $detect_FA -sub $corr_FA -abs detect_corr_abs
```

```

dim1=`fslsize $true_FA|grep "\bdim1\b"|awk '{print $2}'`
dim2=`fslsize $true_FA|grep "\bdim2\b"|awk '{print $2}'`
dim3=`fslsize $true_FA|grep "\bdim3\b"|awk '{print $2}'`

fslmaths $true_FA -mul 0 -add 1 img_1 -odt int

fslmaths $sim_FA -thr .2 -bin -mul $compare_FA_dir/FA_tissue_mask temp_mask

for ((i=0;i<$dim3;i++));do

# for i in 9;do

    fslmaths temp_mask -roi 0 $dim1 0 $dim2 $i 1 0 1 temp_mask_slice

    true_detect_max[$i]=`fslstats true_detect_abs -k temp_mask_slice -r|awk '{print $2}'`

    true_sim_max[$i]=`fslstats true_sim_abs -k temp_mask_slice -r|awk '{print $2}'`

    true_corr_max[$i]=`fslstats true_corr_abs -k temp_mask_slice -r|awk '{print $2}'`

    sim_detect_max[$i]=`fslstats sim_detect_abs -k temp_mask_slice -r|awk '{print $2}'`

    sim_corr_max[$i]=`fslstats sim_corr_abs -k temp_mask_slice -r|awk '{print $2}'`

    detect_corr_max[$i]=`fslstats detect_corr_abs -k temp_mask_slice -r|awk '{print $2}'`

    samples[$i]=`fslstats temp_mask_slice -V|awk '{print $1}'`

done

echo "true_detect_max true_sim_max true_corr_max sim_detect_max sim_corr_max
detect_corr_max samples">max_FA_diffs.txt

echo true_detect_max ${true_detect_max[@]}>>max_FA_diffs.txt

echo true_sim_max ${true_sim_max[@]}>>max_FA_diffs.txt

```

```
echo true_corr_max ${true_corr_max[@]}>>max_FA_diffs.txt  
echo sim_detect_max ${sim_detect_max[@]}>>max_FA_diffs.txt  
echo sim_corr_max ${sim_corr_max[@]}>>max_FA_diffs.txt  
echo detect_corr_max ${detect_corr_max[@]}>>max_FA_diffs.txt  
echo samples ${samples[@]}>>max_FA_diffs.txt
```

APPENDIX H

Scripts for Quantifying FA Changes of GWIS DTI Scans

The script called “switch_deleted_volumes.sh” identifies volumes with the same or similar diffusion direction as volumes that are flagged for removal due to signal void. The scripts listed in Appendix F are then applied to remove the data from these alternate volumes from the calculation of the FA map rather than removing the data from the flagged volumes.

```
thr=$1;

while read tree;do

    bval_dir=/home/keith/GWS/DWI_void_slice_exclusion/2c/$tree

    data_dir=/home/keith/GWS/Results/signal_void_detection/other/2c/$tree;

    sim_dir=/home/keith/GWS/Results/signal_void_detection/compare_output/$tree;

    mkdir -p $sim_dir

    cd $sim_dir;

#   rm -f vol_list;

    all_vols="";

    cat $data_dir/motion_vol_slices_${thr}.txt|awk '{print $1}'|while read vol;do

        if test _${vol:0:1} = _g;then

            echo -n "$vol ";

            all_vols="${all_vols}${vol:15:4} "

            head -`expr ${vol:15:4} + 1` $bval_dir/bvecs_2c|tail -1;

        else
```

```

echo -n "$vol ";

all_vols="${all_vols}${vol:10:4} "

head -`expr ${vol:10:4} + 1` $bval_dir/bvecs_2c|tail -1;

fi;

#vol_list=(`echo $all_vols`);

echo $all_vols>vol_list_${thr};

done>vec_list

if test ! -e vol_list_${thr};then

    continue

fi

echo "Replacing excluded volumes for $tree"

in_vol_list=(`cat vol_list_${thr}`);

out_vol_list=();

#  echo ${in_vol_list[@]}

for ((i=0;i<${#in_vol_list[@]};i++));do

    if test ${in_vol_list[$i]} -le 55;then

        out_vol_list[$i]=`expr ${in_vol_list[$i]} + 56`;

    else

        out_vol_list[$i]=`expr ${in_vol_list[$i]} - 56`;

    fi

done

#  echo ${out_vol_list[@]}

for ((i=0;i<${#out_vol_list[@]};i++));do

```



```

for ((j=0;j<${#in_vol_list[@]};j++));do

    if test ${in_vol_list[$j]} -eq ${out_vol_list[$i]};then

        echo "replacement invalid ${in_vol_list[$j]} ${out_vol_list[$j]}"

        in_vol_num=`zeropad ${in_vol_list[$j]} 4`

        in_vol_num=`expr $in_vol_num + 1`

        bvec=(`head -$in_vol_num $bval_dir/bvecs_2c|tail -1`);

        k=0;

        norm=`echo "scale=6;sqrt(${bvec[0]}^2+${bvec[1]}^2+${bvec[2]}^2)"|bc`;

        vec_x=`echo "scale=6;${bvec[0]}/$norm"| bc`;

        vec_y=`echo "scale=6;${bvec[1]}/$norm"| bc`;

        vec_z=`echo "scale=6;${bvec[2]}/$norm"| bc`;

        while read -a bvec;do

            if test `expr $k % 56` -gt 2 -a `expr $k % 56` -lt 53;then

                norm=`echo "scale=6;sqrt(${bvec[0]}^2+${bvec[1]}^2+${bvec[2]}^2)"|bc`;

                dot=`echo

"scale=6;${vec_x}*${bvec[0]}/${norm}+${vec_y}*${bvec[1]}/${norm}+${vec_z}*${
bvec[2]}/${norm}"|bc`;

                if test `echo "$dot > .8"|bc` = 1 ;then

                    vol_num=`zeropad $k 4`;

                    match=0;

                    for ((l=0;l<${#in_vol_list[@]};l++));do

#                        echo $vol_num

                        if test `expr $vol_num % 56` -eq `expr ${in_vol_list[$l]} % 56`;then

```

```

        match=1;

    fi;

done;

for ((l=0;l<${#out_vol_list[@]};l++));do

#     echo $vol_num

    if test `expr $vol_num % 56` -eq `expr ${out_vol_list[$l]} % 56`;then

        match=1;

    fi;

done;

if test $match -eq 0;then

    vol_num2=`expr $vol_num + 56`

    vol_num2=`zeropad $vol_num2 4`

    echo "replace ${in_vol_list[$j]} with $vol_num";

    echo "replace ${in_vol_list[$i]} with $vol_num2";

    out_vol_list[$i]=$vol_num

    out_vol_list[$j]=$vol_num2

    break;

fi;

fi;

#     echo $i $dot

fi;

    k=`expr $k + 1`;

#     echo ${vol_list[@]};

```

```

done<$bval_dir/bvecs_2c;

fi

done

done

echo ${in_vol_list[@]}

echo ${out_vol_list[@]}

cp $data_dir/vol_combinations_${thr} new_vol_combinations_${thr}

cp $data_dir/slice_vols_${thr} new_slice_vols_${thr}

for ((i=0;i<${#out_vol_list[@]};i++));do

    in_vol=`zeropad ${in_vol_list[$i]} 3`

    in_vol=${in_vol: -3};

    out_vol=`zeropad ${out_vol_list[$i]} 3`

    out_vol=${out_vol: -3};

    cp new_vol_combinations_${thr} temp_vol_combinations_${thr}

    cat temp_vol_combinations_${thr}|sed s/${in_vol}/${out_vol}/|while read vols;do echo

`echo $vols|tr " " "\n"|sort`;done>new_vol_combinations_${thr}

    cp new_slice_vols_${thr} temp_slice_vols_${thr}

    cat temp_slice_vols_${thr}|sed s/${in_vol}/${out_vol}/|while read slice vols;do echo -n

"$slice ";echo `echo $vols|tr " " "\n"|sort`;done>new_slice_vols_${thr}

done

done

```

The script called “max_FA_diff.sh” calculates the robust maximum for each slice of FA differences within the FA tissue mask. The FA differences calculated are between the FA map calculated without removing signal void artifacts and the FA map after removing signal void artifacts. The FA differences between the FA map without removing data and the FA map removing data alternate to the signal void artifacts were also calculated.

```
thr=6.0;

while read tree;do

    data_dir=/home/keith/GWS/DWI_void_slice_exclusion/2c/$tree

    detect_dir=/home/keith/GWS/Results/signal_void_detection/other/2c/$tree

    vib_dir=/home/keith/GWS/Results/signal_void_detection/vibration/2c/$tree

    compare_dir=/home/keith/GWS/Results/signal_void_detection/compare_output/$tree

    compare_vib_dir=/home/keith/GWS/Results/signal_void_detection/compare_output/vibr
ation/$tree

    if test `wc $detect_dir/motion_vol_slices_${thr}.txt|awk '{print $1}'` = 0;then

        echo "no slices removed for $tree"

        continue

    fi

    if test -e $vib_dir/x_regressor;then

        detect_FA=$vib_dir/dti2c_corr_${thr}_FA_combined_brain

        compare_FA=$compare_vib_dir/dti2c_corr_${thr}_FA_combined_brain
```

```

else

    detect_FA=$detect_dir/dti2c_corr_${thr}_FA_brain

    compare_FA=$compare_dir/dti2c_corr_${thr}_FA_brain

fi

cd $compare_dir

echo "Processing $tree.";

fslmaths $detect_dir/dti2cEC_wo_FA -sub $detect_FA -abs dti2c_corr_abs

fslmaths $detect_dir/dti2cEC_wo_FA -sub $compare_FA -abs dti2c_comp_abs

fslmaths $compare_FA -sub $detect_FA -abs comp_corr_abs


dim1=`fslsize $detect_dir/dti2cEC_wo_FA|grep "\bdim1\b"|awk '{print $2}'`
dim2=`fslsize $detect_dir/dti2cEC_wo_FA|grep "\bdim2\b"|awk '{print $2}'`
dim3=`fslsize $detect_dir/dti2cEC_wo_FA|grep "\bdim3\b"|awk '{print $2}'`

fslmaths $detect_dir/dti2cEC_wo_FA -mul 0 -add 1 img_1 -odt int

fslmaths $detect_dir/dti2cEC_wo_FA -thr .2 -bin -mul $data_dir/FA_tissue_mask

temp_mask

for ((i=0;i<$dim3;i++));do

#   for i in 9;do

        fslmaths temp_mask -roi 0 $dim1 0 $dim2 $i 1 0 1 temp_mask_slice

        dti2c_corr_max[$i]=`fslstats dti2c_corr_abs -k temp_mask_slice -r|awk '{print $2}'`

        dti2c_comp_max[$i]=`fslstats dti2c_comp_abs -k temp_mask_slice -r|awk '{print

$2}'`

        comp_corr_max[$i]=`fslstats comp_corr_abs -k temp_mask_slice -r|awk '{print $2}'`

```

```
    samples[$i]=`fslstats temp_mask_slice -V|awk '{print $1}'`  
  
done  
  
echo "$tree dti2c_corr_max dti2c_comp_max comp_corr_max  
samples">max_FA_diffs.txt  
  
echo dti2c_corr_max ${dti2c_corr_max[@]}>>max_FA_diffs.txt  
  
echo dti2c_comp_max ${dti2c_comp_max[@]}>>max_FA_diffs.txt  
  
echo comp_corr_max ${comp_corr_max[@]}>>max_FA_diffs.txt  
  
echo samples ${samples[@]}>>max_FA_diffs.txt  
  
done
```

APPENDIX I

Scripts for Generating Small-FOV Masks

The script called “hr_aliased_tissue_mask.sh” utilizes an image with an FOV that covers the head to generate a mask of the aliased signal in a small-FOV image. The brain mask of the larger FOV image is used to make a brain mask for the small-FOV image.

```
# Build translation matrix to overlay whole brain b0 on brainstem
# Build translation matrices to "alias" whole brain b0 on brainstem
# Threshold "alias" images to make masks of "low signal" regions
# Build mask that includes brainstem signal but excludes "alias" signal
# Register whole brain b0 to brainstem b0 excluding aliased areas in cost
# Build translation matrices to concatenate with registration matrix for "aliasing"
# Threshold "alias" images to make masks of "low signal" regions
# Build brainstem mask of areas with low aliased signal
# Registers standard T1 brain to b0 brain of brainstem DWI
# Registers standard T1 brain mask to brainstem DWI
# Adds mask to brainstem DWI brain mask

standard_T1_2mm_brain=/usr/local/fsl/data/standard/MNI152_T1_2mm_brain
standard_T1_2mm_brain_mask=/usr/local/fsl/data/standard/MNI152_T1_2mm_brain_m
ask

while read tree;do

    tree_dir=/home/keith/GWS/Results/hr_brain_mask/$tree

    cd $tree_dir
```

```
dti2cEC=dti2cEC
```

```
dtihr=dtihrEC
```

```
lr_to_hr_mat=lr_to_hr.mat
```

```
lr_x_offset=`fslhd $dti2cEC |grep sto_xyz:1|awk '{print $5}'|sed s/-/_/`
```

```
lr_y_offset=`fslhd $dti2cEC |grep sto_xyz:2|awk '{print $5}'|sed s/-/_/`
```

```
lr_z_offset=`fslhd $dti2cEC |grep sto_xyz:3|awk '{print $5}'|sed s/-/_/`
```

```
hr_x_offset=`fslhd $dtihr |grep sto_xyz:1|awk '{print $5}'|sed s/-/_/`
```

```
hr_y_offset=`fslhd $dtihr |grep sto_xyz:2|awk '{print $5}'|sed s/-/_/`
```

```
hr_z_offset=`fslhd $dtihr |grep sto_xyz:3|awk '{print $5}'|sed s/-/_/`
```

```
hr_x_dim=`fslhd $dtihr |grep "\bdim1\b"|awk '{print $2}'|sed s/-/_/`
```

```
hr_y_dim=`fslhd $dtihr |grep "\bdim2\b"|awk '{print $2}'|sed s/-/_/`
```

```
hr_x_pixdim=`fslhd $dtihr |grep "\bpixdim1\b"|awk '{print $2}'|sed s/-/_/`
```

```
hr_y_pixdim=`fslhd $dtihr |grep "\bpixdim2\b"|awk '{print $2}'|sed s/-/_/`
```

```
hr_x_fov=`dc -e "8 k $hr_x_dim $hr_x_pixdim * p"`
```

```
hr_y_fov=`dc -e "8 k $hr_y_dim $hr_y_pixdim * p"`
```

```
mat_x_offset=`dc -e "8 k $lr_x_offset $hr_x_offset - _1 * p"`
```

```
mat_plus_x_offset=`dc -e "8 k $lr_x_offset $hr_x_offset - _1 * $hr_x_fov + p"`
```

```
mat_minus_x_offset=`dc -e "8 k $lr_x_offset $hr_x_offset - _1 * $hr_x_fov - p"`
```



```
mat_y_offset=`dc -e "8 k $lr_y_offset $hr_y_offset - p"`
```

```
mat_plus_y_offset=`dc -e "8 k $lr_y_offset $hr_y_offset - $hr_y_fov + p"`
```

```
mat_minus_y_offset=`dc -e "8 k $lr_y_offset $hr_y_offset - $hr_y_fov - p"`
```

```
mat_z_offset=`dc -e "8 k $lr_z_offset $hr_z_offset - p"`
```

```
echo 1 0 0 $mat_x_offset>lr_to_hr.mat
```

```
echo 0 1 0 $mat_y_offset>>lr_to_hr.mat
```

```
echo 0 0 1 $mat_z_offset>>lr_to_hr.mat
```

```
echo 0 0 0 1 >>lr_to_hr.mat
```

```
echo 1 0 0 $mat_plus_x_offset>lr_to_hr_plus_x.mat
```

```
echo 0 1 0 $mat_y_offset>>lr_to_hr_plus_x.mat
```

```
echo 0 0 1 $mat_z_offset>>lr_to_hr_plus_x.mat
```

```
echo 0 0 0 1 >>lr_to_hr_plus_x.mat
```

```
echo 1 0 0 $mat_minus_x_offset>lr_to_hr_minus_x.mat
```

```
echo 0 1 0 $mat_y_offset>>lr_to_hr_minus_x.mat
```

```
echo 0 0 1 $mat_z_offset>>lr_to_hr_minus_x.mat
```

```
echo 0 0 0 1 >>lr_to_hr_minus_x.mat
```

```
echo 1 0 0 $mat_x_offset>lr_to_hr_plus_y.mat
```

```
echo 0 1 0 $mat_plus_y_offset>>lr_to_hr_plus_y.mat
```

```
echo 0 0 1 $mat_z_offset>>lr_to_hr_plus_y.mat
```

```
echo 0 0 0 1 >>lr_to_hr_plus_y.mat
```

```
echo 1 0 0 $mat_x_offset>lr_to_hr_minus_y.mat
```

```
echo 0 1 0 $mat_minus_y_offset>>lr_to_hr_minus_y.mat
```

```
echo 0 0 1 $mat_z_offset>>lr_to_hr_minus_y.mat
```

```
echo 0 0 0 1 >>lr_to_hr_minus_y.mat
```

```
fslroi $dti2cEC ${dti2cEC}_t0 0 1;
```

```
flirt -in ${dti2cEC}_t0 -ref $dtihr -applyxfm -init lr_to_hr_plus_x.mat -out  
${dtihr}_aliased_2x2x2_1
```

```
flirt -in ${dti2cEC}_t0 -ref $dtihr -applyxfm -init lr_to_hr_minus_x.mat -out  
${dtihr}_aliased_2x2x2_2
```

```
flirt -in ${dti2cEC}_t0 -ref $dtihr -applyxfm -init lr_to_hr_plus_y.mat -out  
${dtihr}_aliased_2x2x2_3
```

```
flirt -in ${dti2cEC}_t0 -ref $dtihr -applyxfm -init lr_to_hr_minus_y.mat -out  
${dtihr}_aliased_2x2x2_4
```

```

flirt -in ${dti2cEC}_brain_mask -ref $dtihr -applyxfm -init lr_to_hr.mat -out
${dtihr}_brain_mask

fslmaths ${dtihr}_aliased_2x2x2_1 -add 1 -uthr 51 -bin ${dtihr}_aliased_2x2x2_1
fslmaths ${dtihr}_aliased_2x2x2_2 -add 1 -uthr 51 -bin ${dtihr}_aliased_2x2x2_2
fslmaths ${dtihr}_aliased_2x2x2_3 -add 1 -uthr 51 -bin ${dtihr}_aliased_2x2x2_3
fslmaths ${dtihr}_aliased_2x2x2_4 -add 1 -uthr 51 -bin ${dtihr}_aliased_2x2x2_4
fslmaths ${dtihr}_brain_mask -bin -mul ${dtihr}_aliased_2x2x2_1 -mul
${dtihr}_aliased_2x2x2_2 -mul ${dtihr}_aliased_2x2x2_3 -mul
${dtihr}_aliased_2x2x2_4 ${dtihr}_flirt_mask

imrm ${dtihr}_aliased_2x2x2_1
imrm ${dtihr}_aliased_2x2x2_2
imrm ${dtihr}_aliased_2x2x2_3
imrm ${dtihr}_aliased_2x2x2_4

flirt -in ${dti2cEC}_t0 -ref ${dtihr} -refweight ${dtihr}_flirt_mask -init lr_to_hr.mat -
omat ${dtihr}_aliased_2x2x2_flirt.mat

echo 1 0 0 $hr_x_fov >plus_fovx.mat
echo 0 1 0 0 >>plus_fovx.mat
echo 0 0 1 0 >>plus_fovx.mat
echo 0 0 0 1 >>plus_fovx.mat

```

```
echo 1 0 0 -$hr_x_fov >minus_fovx.mat
```

```
echo 0 1 0 0 >>minus_fovx.mat
```

```
echo 0 0 1 0 >>minus_fovx.mat
```

```
echo 0 0 0 1 >>minus_fovx.mat
```

```
echo 1 0 0 0 >plus_fovy.mat
```

```
echo 0 1 0 $hr_y_fov >>plus_fovy.mat
```

```
echo 0 0 1 0 >>plus_fovy.mat
```

```
echo 0 0 0 1 >>plus_fovy.mat
```

```
echo 1 0 0 0 >minus_fovy.mat
```

```
echo 0 1 0 -$hr_y_fov >>minus_fovy.mat
```

```
echo 0 0 1 0 >>minus_fovy.mat
```

```
echo 0 0 0 1 >>minus_fovy.mat
```

```
convert_xfm -omat lr_to_hr_plus_x.mat -concat plus_fovx.mat
```

```
${dtihr}_aliased_2x2x2_flirt.mat
```

```
convert_xfm -omat lr_to_hr_minus_x.mat -concat minus_fovx.mat
```

```
${dtihr}_aliased_2x2x2_flirt.mat
```

```
convert_xfm -omat lr_to_hr_plus_y.mat -concat plus_fovy.mat
```

```
${dtihr}_aliased_2x2x2_flirt.mat
```

```

convert_xfm -omat lr_to_hr_minus_y.mat -concat minus_fovy.mat

${dtihr}_aliased_2x2x2_flirt.mat

flirt -in ${dti2cEC}_brain_mask -ref $dtihr -applyxfm -init
${dtihr}_aliased_2x2x2_flirt.mat -out ${dtihr}_brain_mask

flirt -in ${dti2cEC}_t0 -ref $dtihr -applyxfm -init lr_to_hr_plus_x.mat -out
${dtihr}_aliased_2x2x2_1

flirt -in ${dti2cEC}_t0 -ref $dtihr -applyxfm -init lr_to_hr_minus_x.mat -out
${dtihr}_aliased_2x2x2_2

flirt -in ${dti2cEC}_t0 -ref $dtihr -applyxfm -init lr_to_hr_plus_y.mat -out
${dtihr}_aliased_2x2x2_3

flirt -in ${dti2cEC}_t0 -ref $dtihr -applyxfm -init lr_to_hr_minus_y.mat -out
${dtihr}_aliased_2x2x2_4

fslmaths ${dtihr}_aliased_2x2x2_1 -add 1 -uthr 51 -bin ${dtihr}_aliased_2x2x2_1
fslmaths ${dtihr}_aliased_2x2x2_2 -add 1 -uthr 51 -bin ${dtihr}_aliased_2x2x2_2
fslmaths ${dtihr}_aliased_2x2x2_3 -add 1 -uthr 51 -bin ${dtihr}_aliased_2x2x2_3
fslmaths ${dtihr}_aliased_2x2x2_4 -add 1 -uthr 51 -bin ${dtihr}_aliased_2x2x2_4

```

```
fslmaths ${dtihr}_aliased_2x2x2_1 -mul ${dtihr}_aliased_2x2x2_2 -mul
${dtihr}_aliased_2x2x2_3 -mul ${dtihr}_aliased_2x2x2_4 ${dtihr}_aliasing_mask

fslmaths ${dtihr}_brain_mask -bin -mul ${dtihr}_aliased_2x2x2_1 -mul
${dtihr}_aliased_2x2x2_2 -mul ${dtihr}_aliased_2x2x2_3 -mul
${dtihr}_aliased_2x2x2_4 ${dtihr}_aliased_tissue_mask
```

```
imrm ${dtihr}_aliased_2x2x2_1
imrm ${dtihr}_aliased_2x2x2_2
imrm ${dtihr}_aliased_2x2x2_3
imrm ${dtihr}_aliased_2x2x2_4
```

```
flirt -in ${dti2cEC}_t0 -ref ${dtihr} -refweight ${dtihr}_aliased_tissue_mask -init
${dtihr}_aliased_2x2x2_flirt.mat -out ${dtihr}_aliased_2x2x2_flirt -omat
${dtihr}_aliased_2x2x2_flirt.mat
```

```
flirt -in ${dti2cEC}_brain_mask -ref $dtihr -applyxfm -init
${dtihr}_aliased_2x2x2_flirt.mat -out ${dtihr}_brain_mask
```

```
fslmaths ${dtihr}_brain_mask -bin ${dtihr}_brain_mask
```

```
flirt -in $standard_T1_2mm_brain -ref ${dtihr} -refweight
${dtihr}_aliased_tissue_mask -omat ${dtihr}_from_MNI.mat
```

```
flirt -in $standard_T1_2mm_brain_mask -ref ${dtihr} -applyxfm -init  
${dtihr}_from_MNI.mat -out ${dtihr}_MNI_brain_mask  
fslmaths ${dtihr}_MNI_brain_mask -add ${dtihr}_brain_mask -bin  
${dtihr}_combined_brain_mask  
  
done
```

APPENDIX J
Maximum FA Changes for Whole Head GWIS DTI Scans

The maximum change in FA caused by removing signal void artifacts was collected for each slice of each whole head DTI scan in the GWIS. The maximum change in FA for the slice with the largest change is reported in the table below. The average of the maximum FA changes for all the affected slices in a subject is also reported in the table below.

Subject ID (National Sample = GWN; Seabees = GWS)	Number of Slices Affected by Signal Void Artifacts	Maximum of Maximum FA Changes	Average of Maximum FA Changes
GWN04	3	0.010	0.010
GWN05	4	0.070	0.021
GWN06	4	0.024	0.013
GWN08	14	0.016	0.008
GWN10	5	0.015	0.010
GWN12	35	0.015	0.009
GWN13	5	0.012	0.009
GWN15	6	0.019	0.012
GWN16	6	0.032	0.019
GWN19	6	0.009	0.007
GWN21	11	0.015	0.007
GWN22	3	0.008	0.007
GWN25	3	0.006	0.005
GWN26	11	0.020	0.011
GWN28	9	0.007	0.006
GWN29	62	0.113	0.008
GWN30	16	0.012	0.007
GWN31	10	0.009	0.007
GWN33	4	0.010	0.008
GWN34	15	0.039	0.018
GWN37	4	0.010	0.008
GWN38	9	0.008	0.006
GWN39	5	0.006	0.005
GWN40	3	0.007	0.006
GWN43	21	0.014	0.008

GWN45	43	0.044	0.013
GWN49	62	0.253	0.020
GWN50	11	0.012	0.009
GWN51	38	0.021	0.012
GWN52	8	0.041	0.012
GWN57	21	0.081	0.014
GWN58	7	0.013	0.009
GWN59	3	0.009	0.008
GWN60	7	0.011	0.006
GWN62	20	0.017	0.009
GWN63	2	0.008	0.008
GWN64	8	0.017	0.009
GWN65	33	0.046	0.012
GWN66	4	0.024	0.013
GWN70	16	0.019	0.010
GWN71	16	0.019	0.013
GWN72	2	0.006	0.006
GWN73	11	0.057	0.024
GWN76	24	0.011	0.007
GWN77	11	0.018	0.010
GWN81	2	0.004	0.004
GWN82	8	0.027	0.012
GWN84	4	0.011	0.008
GWN87	30	0.014	0.008
GWN91	21	0.011	0.008
GWN92	4	0.007	0.005
GWN93	4	0.008	0.007
GWN94	59	0.071	0.021
GWN96	5	0.006	0.005
GWN97	2	0.006	0.005
GWS04	9	0.015	0.007
GWS06	62	0.219	0.034
GWS07	45	0.048	0.018
GWS08	34	0.029	0.012
GWS09	46	0.019	0.011
GWS10	43	0.157	0.026
GWS13	62	0.381	0.015
GWS14	61	0.554	0.026
GWS15	62	0.176	0.030
GWS16	41	0.034	0.012
GWS17	34	0.015	0.009
GWS18	60	0.259	0.047
GWS19	62	0.168	0.003

GWS20	42	0.018	0.010
GWS21	62	0.125	0.003
GWS22	29	0.024	0.009
GWS24	62	0.032	0.007
GWS25	11	0.018	0.011
GWS26	62	0.484	0.076
GWS27	62	0.555	0.018
GWS29	62	0.429	0.036
GWS30	62	0.013	0.001
GWS31	61	0.157	0.014
GWS32	60	0.225	0.014
GWS33	62	0.582	0.045
GWS34	61	0.022	0.005
GWS35	61	0.130	0.018
GWS37	61	0.059	0.001
GWS38	61	0.158	0.011
GWS39	7	0.045	0.016
GWS40	61	0.221	0.023
GWS41	61	0.119	0.003
GWS42	62	0.263	0.036
GWS44	12	0.016	0.009
GWS45	19	0.015	0.010
GWS46	62	0.186	0.005
GWS47	62	0.152	0.020
GWS48	10	0.024	0.013
GWS49	62	0.055	0.005
GWS53	7	0.014	0.010
GWS54	9	0.031	0.023
GWS55	21	0.033	0.013
GWS57	55	0.064	0.017

The maximum change in FA caused by removing data from alternate volumes to those flagged for signal void artifacts was collected for each slice of each whole head DTI scan in the GWIS. The maximum change in FA for the slice with the largest change is reported in the table below. The average of the maximum FA changes for all the affected slices in a subject is also reported in the table.

Subject ID (National Sample = GWN; Seabees = GWS)	Number of Slices Affected by Signal Void Artifacts	Maximum of Maximum FA Changes	Average of Maximum FA Changes
GWN04	3	0.008	0.007
GWN05	4	0.019	0.011
GWN06	4	0.007	0.005
GWN08	14	0.009	0.006
GWN10	5	0.010	0.008
GWN12	35	0.012	0.008
GWN13	5	0.009	0.007
GWN15	6	0.026	0.014
GWN16	6	0.010	0.007
GWN19	6	0.006	0.006
GWN21	11	0.006	0.005
GWN22	3	0.008	0.008
GWN25	3	0.005	0.005
GWN26	11	0.016	0.009
GWN28	9	0.006	0.005
GWN29	62	0.070	0.004
GWN30	16	0.010	0.007
GWN31	10	0.008	0.006
GWN33	4	0.007	0.006
GWN34	15	0.040	0.015
GWN37	4	0.007	0.006
GWN38	9	0.005	0.004
GWN39	5	0.007	0.006
GWN40	3	0.007	0.007
GWN43	21	0.011	0.006
GWN45	43	0.010	0.006
GWN49	62	0.090	0.005
GWN50	11	0.009	0.007

GWN51	38	0.010	0.006
GWN52	8	0.011	0.008
GWN57	21	0.011	0.006
GWN58	7	0.007	0.006
GWN59	3	0.006	0.005
GWN60	7	0.008	0.005
GWN62	20	0.012	0.007
GWN63	2	0.008	0.008
GWN64	8	0.014	0.009
GWN65	33	0.012	0.006
GWN66	4	0.009	0.007
GWN70	16	0.014	0.009
GWN71	16	0.017	0.009
GWN72	2	0.007	0.007
GWN73	11	0.041	0.020
GWN76	24	0.008	0.006
GWN77	11	0.013	0.010
GWN81	2	0.004	0.004
GWN82	8	0.013	0.007
GWN84	4	0.009	0.007
GWN87	30	0.015	0.006
GWN91	21	0.007	0.005
GWN92	4	0.006	0.005
GWN93	4	0.005	0.005
GWN94	59	0.020	0.011
GWN96	5	0.005	0.004
GWN97	2	0.007	0.007
GWS04	9	0.006	0.004
GWS06	62	0.068	0.011
GWS07	45	0.024	0.011
GWS08	34	0.023	0.009
GWS09	46	0.016	0.008
GWS10	43	0.066	0.014
GWS13	62	0.005	0.001
GWS14	61	0.016	0.002
GWS15	62	0.156	0.021
GWS16	41	0.015	0.007
GWS17	34	0.010	0.007
GWS18	60	0.248	0.023
GWS19	62	0.007	0.001
GWS20	42	0.013	0.007
GWS21	62	0.011	0.002
GWS22	29	0.010	0.006

GWS24	62	0.019	0.005
GWS25	11	0.018	0.011
GWS26	62	0.011	0.002
GWS27	62	0.015	0.003
GWS29	62	0.169	0.019
GWS30	62	0.008	0.001
GWS31	61	0.094	0.006
GWS32	60	0.205	0.010
GWS33	62	0.042	0.005
GWS34	61	0.008	0.003
GWS35	61	0.030	0.006
GWS37	61	0.009	0.002
GWS38	61	0.088	0.003
GWS39	7	0.011	0.008
GWS40	61	0.104	0.015
GWS41	61	0.012	0.001
GWS42	62	0.006	0.001
GWS44	12	0.009	0.006
GWS45	19	0.008	0.006
GWS46	62	0.011	0.002
GWS47	62	0.021	0.002
GWS48	10	0.015	0.009
GWS49	62	0.011	0.002
GWS53	7	0.012	0.008
GWS54	9	0.008	0.006
GWS55	21	0.013	0.008
GWS57	55	0.016	0.007

The maximum change in FA caused by removing signal void artifacts was compared to the maximum change in FA caused by removing data from alternate volumes for each slice of each whole head FOV DTI scan in the GWIS. The maximum and minimum of the differences in FA change between removing the artifacts and removing alternate volumes is reported in the table below. The average and the standard deviation of the differences in FA change between removing the artifacts and removing alternate volumes is also reported in the table. The p value of a one tailed paired t test is also given. (For those cases where the average of the differences in FA change between removing the artifacts and removing alternate volumes is negative, the one tailed t test is reported as NA.)

The column labels are:

A = Subject ID (National Sample = GWN; Seabees = GWS)

B = Number of Slices Affected by Signal Void Artifacts

C = Maximum of differences in FA change (Removing Artifacts – Removing Alternates)

D = Minimum of differences in FA change (Removing Artifacts – Removing Alternates)

E = Average of differences in FA change (Removing Artifacts – Removing Alternates)

F = Standard Deviation of differences in FA change (Removing Artifacts – Removing Alternates)

G = P value of a one tailed paired t test (Removing Artifacts – Removing Alternates)

A	B	C	D	E	F	G
GWN04	3	0.003	0.002	0.002	0.001	0.005
GWN05	4	0.051	-0.003	0.010	0.027	0.240
GWN06	4	0.020	-0.002	0.008	0.011	0.112

GWN08	14	0.008	0.000	0.002	0.002	0.001
GWN10	5	0.008	-0.001	0.002	0.004	0.124
GWN12	35	0.006	-0.003	0.002	0.002	0.000
GWN13	5	0.003	0.001	0.001	0.001	0.006
GWN15	6	0.000	-0.007	-0.002	0.003	NA
GWN16	6	0.026	-0.003	0.012	0.011	0.017
GWN19	6	0.003	0.001	0.002	0.001	0.001
GWN21	11	0.010	0.000	0.003	0.003	0.011
GWN22	3	0.000	-0.002	-0.001	0.001	NA
GWN25	3	0.001	-0.001	0.000	0.001	0.348
GWN26	11	0.008	-0.003	0.002	0.003	0.016
GWN28	9	0.002	0.000	0.001	0.001	0.003
GWN29	62	0.113	-0.006	0.004	0.018	0.026
GWN30	16	0.003	-0.003	0.000	0.001	0.245
GWN31	10	0.003	0.000	0.001	0.001	0.003
GWN33	4	0.004	0.000	0.002	0.002	0.082
GWN34	15	0.012	-0.009	0.002	0.006	0.078
GWN37	4	0.004	0.000	0.002	0.001	0.024
GWN38	9	0.004	0.000	0.002	0.001	0.003
GWN39	5	0.000	-0.002	-0.001	0.001	NA
GWN40	3	0.001	-0.001	0.000	0.002	NA
GWN43	21	0.005	-0.001	0.002	0.001	0.000
GWN45	43	0.037	-0.001	0.007	0.008	0.000
GWN49	62	0.251	-0.003	0.015	0.044	0.005
GWN50	11	0.005	0.000	0.002	0.002	0.001
GWN51	38	0.015	0.000	0.005	0.004	0.000
GWN52	8	0.030	-0.002	0.004	0.011	0.139
GWN57	21	0.073	0.000	0.008	0.017	0.030
GWN58	7	0.006	0.001	0.003	0.002	0.001
GWN59	3	0.005	0.002	0.003	0.002	0.027
GWN60	7	0.005	-0.001	0.001	0.002	0.200
GWN62	20	0.007	-0.001	0.003	0.002	0.000
GWN63	2	0.001	0.000	0.001	0.001	0.148
GWN64	8	0.003	-0.002	0.000	0.002	0.247
GWN65	33	0.034	-0.001	0.006	0.009	0.000
GWN66	4	0.017	-0.003	0.006	0.009	0.134
GWN70	16	0.006	-0.002	0.001	0.002	0.009
GWN71	16	0.010	-0.001	0.004	0.003	0.000
GWN72	2	-0.001	-0.002	-0.001	0.000	NA
GWN73	11	0.015	-0.007	0.003	0.006	0.045
GWN76	24	0.007	-0.002	0.001	0.002	0.009
GWN77	11	0.008	-0.004	0.000	0.004	0.453
GWN81	2	0.001	-0.001	0.000	0.001	0.465

GWN82	8	0.014	0.001	0.005	0.004	0.006
GWN84	4	0.005	-0.003	0.001	0.004	0.325
GWN87	30	0.006	-0.002	0.002	0.002	0.000
GWN91	21	0.005	0.000	0.002	0.001	0.000
GWN92	4	0.001	0.000	0.001	0.001	0.088
GWN93	4	0.003	0.001	0.002	0.001	0.008
GWN94	59	0.050	-0.002	0.011	0.010	0.000
GWN96	5	0.002	0.000	0.001	0.001	0.020
GWN97	2	-0.001	-0.001	-0.001	0.000	NA
GWS04	9	0.010	-0.001	0.003	0.005	0.038
GWS06	62	0.218	-0.009	0.023	0.053	0.001
GWS07	45	0.033	-0.004	0.007	0.008	0.000
GWS08	34	0.021	-0.004	0.004	0.006	0.000
GWS09	46	0.011	0.000	0.003	0.002	0.000
GWS10	43	0.138	-0.019	0.013	0.029	0.003
GWS13	62	0.380	-0.002	0.014	0.065	0.046
GWS14	61	0.553	-0.002	0.024	0.089	0.020
GWS15	62	0.175	-0.002	0.010	0.033	0.013
GWS16	41	0.028	-0.002	0.005	0.006	0.000
GWS17	34	0.006	-0.002	0.002	0.002	0.000
GWS18	60	0.259	-0.001	0.024	0.065	0.003
GWS19	62	0.168	0.000	0.002	0.021	0.190
GWS20	42	0.010	-0.003	0.003	0.003	0.000
GWS21	62	0.124	-0.001	0.001	0.016	0.241
GWS22	29	0.017	-0.001	0.003	0.004	0.000
GWS24	62	0.016	-0.001	0.002	0.004	0.000
GWS25	11	0.006	-0.004	0.000	0.003	0.313
GWS26	62	0.483	-0.002	0.075	0.105	0.000
GWS27	62	0.554	-0.002	0.015	0.082	0.082
GWS29	62	0.428	-0.002	0.017	0.081	0.052
GWS30	62	0.005	-0.001	0.000	0.001	NA
GWS31	61	0.156	-0.001	0.008	0.026	0.009
GWS32	60	0.223	-0.002	0.004	0.030	0.146
GWS33	62	0.581	-0.004	0.040	0.095	0.001
GWS34	61	0.017	-0.001	0.001	0.003	0.001
GWS35	61	0.129	-0.003	0.012	0.029	0.001
GWS37	61	0.057	-0.003	-0.001	0.008	NA
GWS38	61	0.157	-0.005	0.007	0.033	0.047
GWS39	7	0.035	0.001	0.008	0.012	0.059
GWS40	61	0.221	-0.002	0.008	0.034	0.029
GWS41	61	0.119	-0.001	0.002	0.015	0.177
GWS42	62	0.262	-0.001	0.035	0.068	0.000
GWS44	12	0.007	-0.001	0.002	0.003	0.005

GWS45	19	0.007	0.001	0.004	0.002	0.000
GWS46	62	0.186	-0.004	0.003	0.024	0.162
GWS47	62	0.152	0.000	0.017	0.045	0.002
GWS48	10	0.015	-0.001	0.004	0.006	0.023
GWS49	62	0.054	-0.002	0.003	0.011	0.023
GWS53	7	0.005	0.000	0.002	0.002	0.017
GWS54	9	0.027	0.000	0.017	0.009	0.000
GWS55	21	0.026	-0.003	0.005	0.007	0.001
GWS57	55	0.052	0.001	0.010	0.010	0.000

APPENDIX K
Maximum FA Changes for Small-FOV GWIS DTI Scans

The maximum change in FA caused by removing signal void artifacts was collected for each slice of each small-FOV DTI scan in the GWIS. The maximum change in FA for the slice with the largest change is reported in the table below. The average of the maximum FA changes for all the affected slices in a subject is also reported in the table.

Subject ID (National Sample = GWN; Seabees = GWS)	Number of Slices Affected by Signal Void Artifacts	Maximum of Maximum FA Changes	Average of Maximum FA Changes
GWN04	21	0.004	0.001
GWN06	21	0.009	0.004
GWN08	22	0.010	0.005
GWN10	22	0.008	0.003
GWN11	23	0.006	0.001
GWN12	22	0.020	0.015
GWN13	23	0.010	0.002
GWN14	22	0.010	0.006
GWN15	23	0.008	0.002
GWN16	20	0.009	0.003
GWN17	22	0.005	0.001
GWN18	21	0.007	0.003
GWN19	22	0.014	0.008
GWN20	22	0.012	0.007
GWN21	23	0.007	0.002
GWN23	21	0.006	0.003
GWN24	22	0.008	0.002
GWN25	23	0.009	0.004
GWN26	22	0.017	0.006
GWN28	23	0.012	0.005
GWN29	22	0.011	0.002
GWN30	20	0.006	0.002
GWN31	23	0.007	0.003
GWN32	23	0.021	0.009
GWN33	22	0.008	0.002

GWN34	22	0.016	0.002
GWN36	22	0.009	0.002
GWN37	18	0.014	0.008
GWN38	23	0.007	0.001
GWN39	20	0.009	0.002
GWN42	21	0.007	0.001
GWN43	23	0.008	0.002
GWN44	23	0.005	0.001
GWN46	22	0.006	0.002
GWN47	23	0.007	0.004
GWN49	22	0.004	0.001
GWN50	22	0.013	0.003
GWN51	21	0.009	0.004
GWN52	23	0.006	0.001
GWN53	22	0.007	0.004
GWN56	21	0.006	0.001
GWN57	22	0.016	0.004
GWN58	23	0.011	0.003
GWN60	23	0.008	0.002
GWN62	22	0.012	0.007
GWN63	23	0.006	0.001
GWN64	23	0.006	0.002
GWN65	21	0.019	0.011
GWN67	23	0.007	0.004
GWN68	23	0.005	0.001
GWN69	21	0.005	0.001
GWN71	23	0.007	0.003
GWN72	21	0.017	0.011
GWN73	23	0.015	0.003
GWN75	23	0.009	0.002
GWN76	23	0.014	0.004
GWN77	23	0.007	0.003
GWN79	22	0.008	0.005
GWN80	23	0.003	0.001
GWN81	23	0.005	0.002
GWN82	23	0.007	0.003
GWN84	23	0.007	0.002
GWN85	21	0.006	0.001
GWN87	22	0.007	0.001
GWN89	23	0.017	0.012
GWN90	23	0.007	0.001
GWN91	23	0.008	0.002
GWN93	22	0.013	0.004

GWN96	23	0.006	0.002
GWN97	23	0.005	0.002
GWS04	22	0.008	0.003
GWS06	23	0.013	0.005
GWS07	24	0.626	0.398
GWS08	23	0.032	0.009
GWS09	22	0.009	0.004
GWS11	23	0.551	0.442
GWS12	22	0.394	0.341
GWS13	21	0.006	0.002
GWS14	20	0.007	0.001
GWS15	20	0.018	0.011
GWS16	19	0.017	0.011
GWS17	21	0.006	0.002
GWS18	20	0.017	0.008
GWS19	21	0.007	0.003
GWS20	21	0.013	0.009
GWS21	22	0.013	0.004
GWS22	18	0.016	0.004
GWS23	22	0.013	0.002
GWS24	19	0.018	0.009
GWS25	22	0.006	0.003
GWS26	20	0.030	0.008
GWS27	20	0.011	0.005
GWS28	22	0.013	0.005
GWS29	16	0.007	0.001
GWS31	19	0.013	0.009
GWS33	19	0.009	0.002
GWS34	20	0.024	0.017
GWS35	20	0.030	0.005
GWS36	23	0.005	0.002
GWS37	22	0.005	0.001
GWS38	17	0.010	0.004
GWS39	21	0.011	0.007
GWS40	19	0.012	0.004
GWS42	20	0.006	0.001
GWS43	22	0.012	0.004
GWS44	20	0.015	0.013
GWS45	19	0.015	0.009
GWS46	19	0.001	0.001
GWS47	23	0.016	0.004
GWS48	23	0.007	0.002
GWS49	21	0.008	0.003

GWS50	22	0.012	0.001
GWS52	20	0.007	0.003
GWS53	22	0.402	0.267
GWS54	22	0.012	0.008
GWS55	19	0.006	0.003
GWS56	23	0.005	0.001
GWS57	20	0.021	0.016
GWS60	19	0.008	0.004

The maximum change in FA caused by removing data from alternate volumes to those flagged for signal void artifacts was collected for each slice of each small-FOV DTI scan in the GWIS. The maximum change in FA for the slice with the largest change is reported in the table below. The average of the maximum FA changes for all the affected slices in a subject is also reported in the table.

Subject ID (National Sample = GWN; Seabees = GWS)	Number of Slices Affected by Signal Void Artifacts	Maximum of Maximum FA Changes	Average of Maximum FA Changes
GWN04	21	0.004	0.001
GWN06	21	0.008	0.004
GWN08	22	0.007	0.005
GWN10	22	0.007	0.002
GWN11	23	0.004	0.000
GWN12	22	0.016	0.011
GWN13	23	0.009	0.001
GWN14	22	0.009	0.005
GWN15	23	0.006	0.001
GWN16	20	0.009	0.003
GWN17	22	0.005	0.000
GWN18	21	0.007	0.003
GWN19	22	0.012	0.006
GWN20	22	0.011	0.006
GWN21	23	0.004	0.001
GWN23	21	0.006	0.002
GWN24	22	0.007	0.002
GWN25	23	0.008	0.003
GWN26	22	0.010	0.003
GWN28	23	0.009	0.004
GWN29	22	0.010	0.002
GWN30	20	0.005	0.001
GWN31	23	0.006	0.002
GWN32	23	0.010	0.007
GWN33	22	0.008	0.001
GWN34	22	0.009	0.001
GWN36	22	0.006	0.001
GWN37	18	0.011	0.008
GWN38	23	0.005	0.001

GWN39	20	0.005	0.001
GWN42	21	0.006	0.001
GWN43	23	0.007	0.002
GWN44	23	0.004	0.001
GWN46	22	0.363	0.018
GWN47	23	0.006	0.004
GWN49	22	0.003	0.000
GWN50	22	0.008	0.002
GWN51	21	0.007	0.003
GWN52	23	0.007	0.001
GWN53	22	0.007	0.004
GWN56	21	0.006	0.001
GWN57	22	0.014	0.002
GWN58	23	0.010	0.002
GWN60	23	0.008	0.001
GWN62	22	0.010	0.007
GWN63	23	0.006	0.001
GWN64	23	0.007	0.001
GWN65	21	0.013	0.008
GWN67	23	0.007	0.003
GWN68	23	0.004	0.000
GWN69	21	0.005	0.000
GWN71	23	0.006	0.002
GWN72	21	0.012	0.007
GWN73	23	0.027	0.003
GWN75	23	0.009	0.001
GWN76	23	0.011	0.003
GWN77	23	0.009	0.003
GWN79	22	0.007	0.004
GWN80	23	0.003	0.000
GWN81	23	0.004	0.001
GWN82	23	0.008	0.003
GWN84	23	0.328	0.016
GWN85	21	0.005	0.001
GWN87	22	0.007	0.001
GWN89	23	0.013	0.010
GWN90	23	0.005	0.000
GWN91	23	0.007	0.002
GWN93	22	0.010	0.004
GWN96	23	0.006	0.002
GWN97	23	0.005	0.001
GWS04	22	0.007	0.002
GWS06	23	0.012	0.004

GWS07	24	0.626	0.398
GWS08	23	0.024	0.008
GWS09	22	0.007	0.003
GWS11	23	0.551	0.442
GWS12	22	0.394	0.341
GWS13	21	0.005	0.001
GWS14	20	0.006	0.001
GWS15	20	0.015	0.009
GWS16	19	0.016	0.009
GWS17	21	0.005	0.001
GWS18	20	0.014	0.007
GWS19	21	0.007	0.001
GWS20	21	0.010	0.008
GWS21	22	0.018	0.004
GWS22	18	0.010	0.003
GWS23	22	0.010	0.002
GWS24	19	0.015	0.008
GWS25	22	0.006	0.002
GWS26	20	0.018	0.007
GWS27	20	0.010	0.005
GWS28	22	0.013	0.005
GWS29	16	0.005	0.001
GWS31	19	0.011	0.008
GWS33	19	0.009	0.002
GWS34	20	0.017	0.014
GWS35	20	0.013	0.004
GWS36	23	0.005	0.001
GWS37	22	0.005	0.001
GWS38	17	0.009	0.004
GWS39	21	0.011	0.006
GWS40	19	0.011	0.004
GWS42	20	0.007	0.001
GWS43	22	0.009	0.003
GWS44	20	0.011	0.008
GWS45	19	0.014	0.007
GWS46	19	0.000	0.000
GWS47	23	0.014	0.003
GWS48	23	0.006	0.001
GWS49	21	0.006	0.002
GWS50	22	0.011	0.001
GWS52	20	0.006	0.002
GWS53	22	0.402	0.267
GWS54	22	0.009	0.006

GWS55	19	0.357	0.021
GWS56	23	0.007	0.001
GWS57	20	0.014	0.011
GWS60	19	0.006	0.003

The maximum change in FA caused by removing signal void artifacts was compared to the maximum change in FA caused by removing data from alternate volumes for each slice of each small-FOV DTI scan in the GWIS. The maximum and minimum of the differences in FA change between removing the artifacts and removing alternate volumes is reported in the table below. The average and the standard deviation of the differences in FA change between removing the artifacts and removing alternate volumes is also reported in the table. The p value of a one tailed paired t test is also given. (For those cases where the average of the differences in FA change between removing the artifacts and removing alternate volumes is negative, the one tailed t test is reported as NA.)

The column labels are:

A = Subject ID (National Sample = GWN; Seabees = GWS)

B = Number of Slices Affected by Signal Void Artifacts

C = Maximum of differences in FA change (Removing Artifacts – Removing Alternates)

D = Minimum of differences in FA change (Removing Artifacts – Removing Alternates)

E = Average of differences in FA change (Removing Artifacts – Removing Alternates)

F = Standard Deviation of differences in FA change (Removing Artifacts – Removing Alternates)

G = P value of a one tailed paired t test (Removing Artifacts – Removing Alternates)

A	B	C	D	E	F	G
GWN04	21	0.001	0.000	0.000	0.000	0.000
GWN06	21	0.002	-0.001	0.000	0.001	0.001
GWN08	22	0.003	-0.001	0.001	0.001	0.001
GWN10	22	0.002	-0.001	0.000	0.001	0.000
GWN11	23	0.002	0.000	0.000	0.000	0.000
GWN12	22	0.009	0.001	0.004	0.002	0.000

GWN13	23	0.001	0.000	0.001	0.000	0.000
GWN14	22	0.004	0.000	0.001	0.001	0.000
GWN15	23	0.003	0.000	0.001	0.001	0.000
GWN16	20	0.001	-0.002	0.000	0.001	0.046
GWN17	22	0.001	0.000	0.001	0.000	0.000
GWN18	21	0.001	-0.002	0.000	0.001	0.168
GWN19	22	0.005	0.000	0.001	0.001	0.000
GWN20	22	0.003	-0.001	0.001	0.001	0.001
GWN21	23	0.004	-0.001	0.001	0.001	0.000
GWN23	21	0.002	0.000	0.001	0.000	0.000
GWN24	22	0.001	-0.001	0.000	0.000	0.000
GWN25	23	0.002	-0.001	0.001	0.001	0.000
GWN26	22	0.011	0.000	0.002	0.003	0.000
GWN28	23	0.004	-0.001	0.001	0.001	0.000
GWN29	22	0.001	-0.001	0.000	0.001	0.017
GWN30	20	0.001	-0.001	0.000	0.000	0.000
GWN31	23	0.002	-0.001	0.001	0.001	0.000
GWN32	23	0.012	0.000	0.002	0.003	0.002
GWN33	22	0.002	-0.001	0.000	0.001	0.007
GWN34	22	0.006	0.000	0.001	0.001	0.002
GWN36	22	0.004	0.000	0.001	0.001	0.001
GWN37	18	0.004	0.000	0.001	0.001	0.001
GWN38	23	0.002	0.000	0.001	0.000	0.000
GWN39	20	0.003	0.000	0.001	0.001	0.000
GWN42	21	0.001	0.000	0.000	0.000	0.000
GWN43	23	0.001	-0.001	0.001	0.000	0.000
GWN44	23	0.001	0.000	0.001	0.000	0.000
GWN46	22	0.001	-0.363	-0.016	0.077	NA
GWN47	23	0.002	-0.001	0.000	0.001	0.029
GWN49	22	0.002	0.000	0.001	0.000	0.000
GWN50	22	0.005	0.000	0.001	0.001	0.001
GWN51	21	0.002	-0.001	0.001	0.001	0.000
GWN52	23	0.000	-0.001	0.000	0.000	0.038
GWN53	22	0.001	-0.001	0.000	0.001	0.026
GWN56	21	0.001	-0.001	0.000	0.000	0.000
GWN57	22	0.006	0.000	0.002	0.001	0.000
GWN58	23	0.001	0.000	0.001	0.000	0.000
GWN60	23	0.001	0.000	0.001	0.000	0.000
GWN62	22	0.002	-0.001	0.000	0.001	0.058
GWN63	23	0.001	0.000	0.001	0.000	0.000
GWN64	23	0.001	-0.001	0.001	0.000	0.000
GWN65	21	0.009	0.000	0.003	0.003	0.000
GWN67	23	0.002	0.000	0.001	0.001	0.000

GWN68	23	0.001	0.000	0.001	0.000	0.000
GWN69	21	0.001	0.000	0.001	0.000	0.000
GWN71	23	0.003	0.000	0.001	0.001	0.000
GWN72	21	0.009	0.002	0.004	0.002	0.000
GWN73	23	0.002	-0.012	0.000	0.003	NA
GWN75	23	0.001	-0.001	0.001	0.000	0.000
GWN76	23	0.003	0.000	0.001	0.001	0.000
GWN77	23	0.001	-0.002	0.000	0.001	0.217
GWN79	22	0.003	0.000	0.001	0.001	0.000
GWN80	23	0.001	0.000	0.001	0.000	0.000
GWN81	23	0.001	0.000	0.001	0.000	0.000
GWN82	23	0.001	-0.002	0.000	0.001	0.023
GWN84	23	0.001	-0.327	-0.014	0.068	NA
GWN85	21	0.001	0.000	0.001	0.000	0.000
GWN87	22	0.001	0.000	0.000	0.000	0.000
GWN89	23	0.006	0.001	0.002	0.001	0.000
GWN90	23	0.002	0.000	0.001	0.000	0.000
GWN91	23	0.001	0.000	0.001	0.000	0.000
GWN93	22	0.003	-0.001	0.000	0.001	0.054
GWN96	23	0.001	0.000	0.001	0.001	0.000
GWN97	23	0.001	-0.001	0.000	0.000	0.000
GWS04	22	0.005	-0.001	0.001	0.001	0.000
GWS06	23	0.002	-0.001	0.000	0.001	0.006
GWS07	24	0.000	-0.001	0.000	0.000	NA
GWS08	23	0.008	-0.002	0.001	0.002	0.009
GWS09	22	0.004	0.000	0.001	0.001	0.000
GWS11	23	0.000	-0.001	0.000	0.000	NA
GWS12	22	0.000	0.000	0.000	0.000	0.008
GWS13	21	0.001	-0.001	0.001	0.001	0.000
GWS14	20	0.002	-0.001	0.001	0.000	0.000
GWS15	20	0.004	-0.001	0.001	0.001	0.000
GWS16	19	0.006	-0.003	0.001	0.002	0.005
GWS17	21	0.001	0.000	0.001	0.000	0.000
GWS18	20	0.004	-0.003	0.001	0.001	0.001
GWS19	21	0.003	0.000	0.002	0.001	0.000
GWS20	21	0.002	-0.001	0.001	0.001	0.015
GWS21	22	0.001	-0.005	0.000	0.001	0.109
GWS22	18	0.006	0.000	0.001	0.001	0.011
GWS23	22	0.004	0.000	0.001	0.001	0.001
GWS24	19	0.005	-0.001	0.001	0.002	0.001
GWS25	22	0.002	0.000	0.001	0.001	0.000
GWS26	20	0.011	-0.001	0.001	0.003	0.011
GWS27	20	0.003	-0.001	0.001	0.001	0.006

GWS28	22	0.001	-0.002	0.000	0.001	0.008
GWS29	16	0.002	-0.001	0.000	0.001	0.004
GWS31	19	0.003	0.000	0.001	0.001	0.000
GWS33	19	0.001	-0.001	0.000	0.000	0.000
GWS34	20	0.009	0.000	0.003	0.003	0.000
GWS35	20	0.017	-0.002	0.001	0.004	0.080
GWS36	23	0.001	0.000	0.001	0.000	0.000
GWS37	22	0.001	-0.001	0.001	0.000	0.000
GWS38	17	0.002	-0.002	0.000	0.001	0.408
GWS39	21	0.002	-0.001	0.001	0.001	0.000
GWS40	19	0.003	-0.001	0.000	0.001	0.010
GWS42	20	0.001	-0.002	0.000	0.001	0.005
GWS43	22	0.005	-0.001	0.001	0.001	0.001
GWS44	20	0.008	0.001	0.005	0.002	0.000
GWS45	19	0.003	-0.001	0.001	0.001	0.000
GWS46	19	0.001	0.000	0.001	0.000	0.000
GWS47	23	0.007	-0.001	0.001	0.002	0.008
GWS48	23	0.002	0.000	0.001	0.000	0.000
GWS49	21	0.002	0.000	0.001	0.001	0.000
GWS50	22	0.002	0.000	0.000	0.000	0.000
GWS52	20	0.002	0.000	0.001	0.000	0.000
GWS53	22	0.001	-0.001	0.000	0.000	0.302
GWS54	22	0.005	0.000	0.002	0.001	0.000
GWS55	19	0.001	-0.356	-0.018	0.082	NA
GWS56	23	0.001	-0.002	0.000	0.001	0.048
GWS57	20	0.010	0.002	0.005	0.002	0.000
GWS60	19	0.003	0.000	0.001	0.001	0.000

BIBLIOGRAPHY

- Abe, O., H. Yamasue, et al. (2006). "Voxel-based diffusion tensor analysis reveals aberrant anterior cingulum integrity in posttraumatic stress disorder due to terrorism." Psychiatry Res **146**(3): 231-242.
- Ahn, C. B. and Z. H. Cho (1991). "Analysis of the eddy-current induced artifacts and the temporal compensation in nuclear magnetic resonance imaging." IEEE Trans Med Imaging **10**(1): 47-52.
- Alexander, A. L., J. S. Tsuruda, et al. (1997). "Elimination of eddy current artifacts in diffusion-weighted echo-planar images: the use of bipolar gradients." Magn Reson Med **38**(6): 1016-1021.
- Alexander, D. C. and G. J. Barker (2005). "Optimal imaging parameters for fiber-orientation estimation in diffusion MRI." Neuroimage **27**(2): 357-367.
- Assaf, Y., R. Z. Freidlin, et al. (2004). "New modeling and experimental framework to characterize hindered and restricted water diffusion in brain white matter." Magn Reson Med **52**(5): 965-978.
- Basser, P. J., J. Mattiello, et al. (1994). "Estimation of the effective self-diffusion tensor from the NMR spin echo." J Magn Reson B **103**(3): 247-254.
- Beaulieu, C. (2002). "The basis of anisotropic water diffusion in the nervous system - a technical review." NMR Biomed **15**(7-8): 435-455.
- Behrens, T. E., H. J. Berg, et al. (2007). "Probabilistic diffusion tractography with multiple fibre orientations: What can we gain?" Neuroimage **34**(1): 144-155.
- Behrens, T. E., M. W. Woolrich, et al. (2003). "Characterization and propagation of

- uncertainty in diffusion-weighted MR imaging." Magn Reson Med **50**(5): 1077-1088.
- Benarroch, E. E. (2009). "The locus ceruleus norepinephrine system: functional organization and potential clinical significance." Neurology **73**(20): 1699-1704.
- Bhagat, Y. A. and C. Beaulieu (2004). "Diffusion anisotropy in subcortical white matter and cortical gray matter: changes with aging and the role of CSF-suppression." J Magn Reson Imaging **20**(2): 216-227.
- Birn, R. M., M. A. Smith, et al. (2008). "The respiration response function: the temporal dynamics of fMRI signal fluctuations related to changes in respiration." Neuroimage **40**(2): 644-654.
- Brown, R. (1828). "A brief account of microscopical observations made in the months of June, July and August, 1827, on the particles contained in the pollen of plants; and on the general existence of active molecules in organic and inorganic bodies." Philosophical Magazine **4**: 161-173.
- Calamante, F., J. D. Tournier, et al. (2011). "Track density imaging (TDI): validation of super resolution property." Neuroimage **56**(3): 1259-1266.
- Carr, H. Y. and E. M. Purcell (1954). "Effects of Diffusion on Free Precession in Nuclear Magnetic Resonance Experiments." Physical Review **94**(3): 630-638.
- Chang, L. C., D. K. Jones, et al. (2005). "RESTORE: robust estimation of tensors by outlier rejection." Magn Reson Med **53**(5): 1088-1095.
- Chou, K. H., Y. Cheng, et al. (2011). "Sex-linked white matter microstructure of the social and analytic brain." Neuroimage **54**(1): 725-733.
- Cook, P. A., Y. Bai, et al. (2006). Camino: Open-Source Diffusion-MRI Reconstruction

- and Processing. 14th Scientific Meeting of the International Society for Magnetic Resonance in Medicine. Seattle, WA: 2759.
- Dietrich, O., S. Heiland, et al. (2001). "Noise correction for the exact determination of apparent diffusion coefficients at low SNR." Magn Reson Med **45**(3): 448-453.
- Dietrich, O., J. G. Raya, et al. (2007). "Measurement of signal-to-noise ratios in MR images: influence of multichannel coils, parallel imaging, and reconstruction filters." J Magn Reson Imaging **26**(2): 375-385.
- Einstein, A., Ed. (1956). Investigations on the Theory of the Brownian Movement. Mineola, N.Y., Dover Publications, Inc.
- Elster, A. D. and J. Burdette (2001). Questions and answers in magnetic resonance imaging. St Louis, Mo., Mosby.
- Feinberg, D. A. and A. S. Mark (1987). "Human brain motion and cerebrospinal fluid circulation demonstrated with MR velocity imaging." Radiology **163**(3): 793-799.
- Gallichan, D., J. Scholz, et al. (2010). "Addressing a systematic vibration artifact in diffusion-weighted MRI." Hum Brain Mapp **31**(2): 193-202.
- Golay, X., H. Jiang, et al. (2002). "High-resolution isotropic 3D diffusion tensor imaging of the human brain." Magn Reson Med **47**(5): 837-843.
- Greitz, D., R. Wirestam, et al. (1992). "Pulsatile brain movement and associated hydrodynamics studied by magnetic resonance phase imaging. The Monroe-Kellie doctrine revisited." Neuroradiology **34**(5): 370-380.
- Gudbjartsson, H. and S. Patz (1995). "The Rician distribution of noisy MRI data." Magn Reson Med **34**(6): 910-914.

- Gurses, B., N. Tasdelen, et al. (2011). "Diagnostic utility of DTI in prostate cancer." Eur J Radiol **79**(2): 172-176.
- Habib, J., D. P. Auer, et al. (2010). "A quantitative analysis of the benefits of cardiac gating in practical diffusion tensor imaging of the brain." Magn Reson Med **63**(4): 1098-1103.
- Haley, R. W., T. L. Kurt, et al. (1997). "Is there a Gulf War Syndrome? Searching for syndromes by factor analysis of symptoms." JAMA **277**(3): 215-222.
- Haley, R. W., W. W. Marshall, et al. (2000). "Brain abnormalities in Gulf War syndrome: evaluation with 1H MR spectroscopy." Radiology **215**(3): 807-817.
- Haselgrove, J. C. and J. R. Moore (1996). "Correction for distortion of echo-planar images used to calculate the apparent diffusion coefficient." Magn Reson Med **36**(6): 960-964.
- Henkelman, R. M. (1985). "Measurement of signal intensities in the presence of noise in MR images." Med Phys **12**(2): 232-233.
- Hiltunen, J., R. Hari, et al. (2006). "Quantification of mechanical vibration during diffusion tensor imaging at 3 T." Neuroimage **32**(1): 93-103.
- Hoogendijk, W. J., C. W. Pool, et al. (1995). "Image analyser-assisted morphometry of the locus coeruleus in Alzheimer's disease, Parkinson's disease and amyotrophic lateral sclerosis." Brain **118** (Pt 1): 131-143.
- Huster, R. J., R. Westerhausen, et al. (2009). "Hemispheric and gender related differences in the midcingulum bundle: a DTI study." Hum Brain Mapp **30**(2): 383-391.
- Iannacchione, V. G., J. A. Dever, et al. (2011). "Validation of a Research Case Definition of Gulf War Illness in the 1991 US Military Population." Neuroepidemiology

37(2): 129-140.

- Jenkinson, M. and S. Smith (2001). "A global optimisation method for robust affine registration of brain images." Med Image Anal **5(2): 143-156.**
- Jeong, E. K., S. E. Kim, et al. (2005). "High-resolution DTI with 2D interleaved multislice reduced FOV single-shot diffusion-weighted EPI (2D ss-rFOV-DWEPI)." Magn Reson Med **54(6): 1575-1579.**
- Jiang, H., X. Golay, et al. (2002). "Origin and minimization of residual motion-related artifacts in navigator-corrected segmented diffusion-weighted EPI of the human brain." Magn Reson Med **47(4): 818-822.**
- Jones, D. K. (2004). "The effect of gradient sampling schemes on measures derived from diffusion tensor MRI: a Monte Carlo study." Magn Reson Med **51(4): 807-815.**
- Jones, D. K. (2009). Gaussian Modeling of the Diffusion Signal. Diffusion MRI. J.-B. Heidi and E. J. B. Timothy. San Diego, Academic Press: 37-54.
- Jones, D. K. and P. J. Basser (2004). ""Squashing peanuts and smashing pumpkins": how noise distorts diffusion-weighted MR data." Magn Reson Med **52(5): 979-993.**
- Jones, D. K. and M. Cercignani (2010). "Twenty-five pitfalls in the analysis of diffusion MRI data." NMR Biomed **23(7): 803-820.**
- Jones, D. K., M. A. Horsfield, et al. (1999). "Optimal strategies for measuring diffusion in anisotropic systems by magnetic resonance imaging." Magn Reson Med **42(3): 515-525.**
- Karampinos, D. C., A. T. Van, et al. (2008). "High resolution reduced-FOV diffusion tensor imaging of the human pons with multi-shot variable density spiral at 3T." Conf Proc IEEE Eng Med Biol Soc **2008: 5761-5764.**

- Kieseppa, T., M. Eerola, et al. (2010). "Major depressive disorder and white matter abnormalities: a diffusion tensor imaging study with tract-based spatial statistics." J Affect Disord **120**(1-3): 240-244.
- Kim, C. K., S. M. Jang, et al. (2011). "Diffusion tensor imaging of normal prostate at 3T: effect of number of diffusion-encoding directions on quantitation and image quality." Br J Radiol.
- Kim, S. J., D. U. Jeong, et al. (2006). "Asymmetrically altered integrity of cingulum bundle in posttraumatic stress disorder." Neuropsychobiology **54**(2): 120-125.
- Kruger, G. and G. H. Glover (2001). "Physiological noise in oxygenation-sensitive magnetic resonance imaging." Magn Reson Med **46**(4): 631-637.
- Lebel, C., M. Gee, et al. (2012). "Diffusion tensor imaging of white matter tract evolution over the lifespan." Neuroimage **60**(1): 340-352.
- LeBihan, D. and P. J. Basser (1995). Molecular Diffusion and Nuclear Magnetic Resonance. Diffusion and Perfusion Magnetic Resonance Imaging: Applications to Functional MRI. D. LeBihan. New York, Raven Press.
- Li, L., N. Ma, et al. (2007). "Prefrontal white matter abnormalities in young adult with major depressive disorder: a diffusion tensor imaging study." Brain Res **1168**: 124-128.
- Liang, Z.-P. and P. C. Lauterbur (2000). Principles of Magnetic Resonance Imaging: A Signal Processing Perspective. New York, IEEE Press.
- Liu, F., L. Vidarsson, et al. (2010). "Sex differences in the human corpus callosum microstructure: a combined T2 myelin-water and diffusion tensor magnetic resonance imaging study." Brain Res **1343**: 37-45.

- Mangin, J. F., C. Poupon, et al. (2002). "Distortion correction and robust tensor estimation for MR diffusion imaging." Med Image Anal **6**(3): 191-198.
- Markwardt, C. B. "MPFIT: IDL curve fitting and function optimization." Retrieved 10/19/2011, from <http://www.physics.wisc.edu/~craigm/idl/fitting.html>.
- McColl, R., S. Li, et al. (2009). "Diffuse White Matter Differences Between Gulf War Syndrome II and Control Subjects Revealed by Diffusion Tensor MRI." NeuroImage **47**(S1): S105.
- McGibney, G. and M. R. Smith (1993). "An unbiased signal-to-noise ratio measure for magnetic resonance images." Med Phys **20**(4): 1077-1078.
- Menzler, K., M. Belke, et al. (2011). "Men and women are different: diffusion tensor imaging reveals sexual dimorphism in the microstructure of the thalamus, corpus callosum and cingulum." Neuroimage **54**(4): 2557-2562.
- Mori, S., B. J. Crain, et al. (1999). "Three-dimensional tracking of axonal projections in the brain by magnetic resonance imaging." Ann Neurol **45**(2): 265-269.
- Morris, D., R. Nossin-Manor, et al. (2011). "Preterm neonatal diffusion processing using detection and replacement of outliers prior to resampling." Magn Reson Med.
- Nagae-Poetscher, L. M., H. Jiang, et al. (2004). "High-resolution diffusion tensor imaging of the brain stem at 3 T." AJNR Am J Neuroradiol **25**(8): 1325-1330.
- Nam, H. and H. J. Park (2011). "Distortion correction of high b-valued and high angular resolution diffusion images using iterative simulated images." Neuroimage **57**(3): 968-978.
- Nichols, T. E. and A. P. Holmes (2002). "Nonparametric permutation tests for functional neuroimaging: a primer with examples." Hum Brain Mapp **15**(1): 1-25.

- Nunes, R. G., P. Jezzard, et al. (2005). "Investigations on the efficiency of cardiac-gated methods for the acquisition of diffusion-weighted images." J Magn Reson **177**(1): 102-110.
- Pierpaoli, C. (2011). Artifacts in Diffusion MRI. Diffusion MRI: theory, method, and applications. D. K. Jones. New York, Oxford University Press.
- Pipe, J. (2009). Pulse Sequences for Diffusion-weighted MRI. Diffusion MRI. J.-B. Heide and E. J. B. Timothy. San Diego, Academic Press: 11-35.
- Poncelet, B. P., V. J. Wedeen, et al. (1992). "Brain parenchyma motion: measurement with cine echo-planar MR imaging." Radiology **185**(3): 645-651.
- Raj, D., A. W. Anderson, et al. (2001). "Respiratory effects in human functional magnetic resonance imaging due to bulk susceptibility changes." Phys Med Biol **46**(12): 3331-3340.
- Raj, D., D. P. Paley, et al. (2000). "A model for susceptibility artefacts from respiration in functional echo-planar magnetic resonance imaging." Phys Med Biol **45**(12): 3809-3820.
- Reese, T. G., O. Heid, et al. (2003). "Reduction of eddy-current-induced distortion in diffusion MRI using a twice-refocused spin echo." Magn Reson Med **49**(1): 177-182.
- Sala, S., F. Agosta, et al. (2012). "Microstructural changes and atrophy in brain white matter tracts with aging." Neurobiol Aging **33**(3): 488-498 e482.
- Schuff, N., Y. Zhang, et al. (2011). "Patterns of altered cortical perfusion and diminished subcortical integrity in posttraumatic stress disorder: an MRI study." Neuroimage **54 Suppl 1**: S62-68.

- Sharman, M. A., J. Cohen-Adad, et al. (2011). "Impact of outliers on diffusion tensor and Q-ball imaging: clinical implications and correction strategies." J Magn Reson Imaging **33**(6): 1491-1502.
- Sinha, S. and U. Sinha (2004). "In vivo diffusion tensor imaging of the human prostate." Magn Reson Med **52**(3): 530-537.
- Skare, S. and J. L. Andersson (2001). "On the effects of gating in diffusion imaging of the brain using single shot EPI." Magn Reson Imaging **19**(8): 1125-1128.
- Smith, S. M. (2002). "Fast robust automated brain extraction." Hum Brain Mapp **17**(3): 143-155.
- Smith, S. M., M. Jenkinson, et al. (2006). "Tract-based spatial statistics: voxelwise analysis of multi-subject diffusion data." Neuroimage **31**(4): 1487-1505.
- Smith, S. M., M. Jenkinson, et al. (2004). "Advances in functional and structural MR image analysis and implementation as FSL." Neuroimage **23 Suppl 1**: S208-219.
- Stejskal, E. O. and J. E. Tanner (1965). "Spin Diffusion Measurements: Spin Echoes in the Presence of a Time-Dependent Field Gradient." Journal of Chemical Physics **42**(1): 288-292.
- Storey, P., F. J. Frigo, et al. (2007). "Partial k-space reconstruction in single-shot diffusion-weighted echo-planar imaging." Magn Reson Med **57**(3): 614-619.
- Tournier, J. D., S. Mori, et al. (2011). "Diffusion tensor imaging and beyond." Magn Reson Med **65**(6): 1532-1556.
- Truong, T. K., N. K. Chen, et al. (2011). "Dynamic correction of artifacts due to susceptibility effects and time-varying eddy currents in diffusion tensor imaging." Neuroimage **57**(4): 1343-1347.

- Van de Moortele, P. F., J. Pfeuffer, et al. (2002). "Respiration-induced B0 fluctuations and their spatial distribution in the human brain at 7 Tesla." Magn Reson Med **47**(5): 888-895.
- van Gelderen, P., M. H. de Vleeschouwer, et al. (1994). "Water diffusion and acute stroke." Magn Reson Med **31**(2): 154-163.
- Wedeen, V. J., R. M. Weisskoff, et al. (1994). "MRI signal void due to in-plane motion is all-or-none." Magn Reson Med **32**(1): 116-120.
- Wu, Y. C., A. S. Field, et al. (2011). "Age- and gender-related changes in the normal human brain using hybrid diffusion imaging (HYDI)." Neuroimage **54**(3): 1840-1853.
- Zhan, L., A. D. Leow, et al. (2010). "How does angular resolution affect diffusion imaging measures?" Neuroimage **49**(2): 1357-1371.
- Zhang, L., Y. Zhang, et al. (2011). "Different white matter abnormalities between the first-episode, treatment-naïve patients with posttraumatic stress disorder and generalized anxiety disorder without comorbid conditions." J Affect Disord **133**(1-2): 294-299.
- Zhou, Z., W. Liu, et al. (2011). "Automated artifact detection and removal for improved tensor estimation in motion-corrupted DTI data sets using the combination of local binary patterns and 2D partial least squares." Magn Reson Imaging **29**(2): 230-242.
- Zhu, X., X. Wang, et al. (2011). "Altered white matter integrity in first-episode, treatment-naïve young adults with major depressive disorder: a tract-based spatial statistics study." Brain Res **1369**: 223-229.